

Developing a Magnetic Reconnection Model to Interpret Blazar Variability as Measured with the FACT Telescope

Master Thesis in Physics

by

Marc Klinger, B.Sc.

submitted to

III. PHYSIKALISCHES INSTITUT A

RHEINISCH-WESTFÄLISCHE TECHNISCHE HOCHSCHULE AACHEN

Prof. Dr. Thomas Bretz

Prof. Dr. Philipp Mertsch

in

December 2019

First Referee

Prof. Dr. Thomas Bretz
Physics Institute III A
RWTH Aachen University

Second Referee

Prof. Dr. Philipp Mertsch
Institute for Theoretical Particle Physics and Cosmology
RWTH Aachen University

Contents

1. Introduction	1
1.1. Idea of This Thesis	1
1.2. Active Galaxies and Blazars	2
1.3. Detection of Gamma Rays	6
2. FACT	13
2.1. First G-APD Cherenkov Telescope	13
2.2. Data Taking	15
2.3. From Light in the Camera to an Image	17
2.4. FACT Monte Carlos	21
2.5. Trigger Efficiency from Monte Carlos	26
2.6. Cut Efficiencies and Uncertainties	27
2.7. Quality Cuts	28
2.8. Reconstruction of the Origin	30
2.9. Cut on Arrival Direction	32
2.10. Gamma-Hadron-Separation	34
2.11. Performance of Complete Analysis	36
3. PIC Simulations of Magnetic Reconnection	39
3.1. Magnetohydrodynamics	39
3.2. Flux Freezing	40
3.3. Magnetic Reconnection	42
3.4. PIC Simulations in Two and Three Dimensions	44
3.5. Evolution of a Stationary State with Plasmoids	45
3.6. Monte Carlo Approach to Replace PIC-Simulations	51
3.6.1. Numerical Implementation	52
3.6.2. Results for a Complete Layer	56
3.6.3. Long-Term Evolution	64
4. Non-Thermal Radiation Modelling	67
4.1. Normalisations	67
4.2. Number Density and Compactness	67
4.3. Effects of Special Relativity	68
4.4. Black Body	70
4.5. Radiative Processes	72
4.5.1. Synchrotron Radiation	73
4.5.2. Inverse Compton Scattering	76
4.5.3. Pair Production	81

4.6. Numerical Solving of the Equations	82
4.7. Synchrotron Radiation for a Power Law	86
4.8. Synchrotron in Steady State	88
4.9. Inverse Compton Scattering on a Black Body for a Power Law	90
4.10. Inverse Compton Scattering on a Black Body in Steady State	92
4.11. Modelling the Radiation in a Plasmoid	94
4.11.1. Doppler Factor of Plasmoid and Broad Line Region	95
4.11.2. Boosting the Results of the Radiation Modelling	96
4.11.3. Injection and Escape	97
4.11.4. After Leaving the Layer	98
4.11.5. Transformation of the Photon Escape	98
4.12. Results for Single Plasmoids	99
4.13. Light Curves of a Complete Reconnection Layer	107
5. Summary	109
5.1. Outlook	110
A. List of Abbreviations	113
References	I

1

Introduction

1.1. Idea of This Thesis

While it was common for centuries to look at the night sky and try to understand the emerging picture based only on the picture in the optical range of the electromagnetic spectrum, this has been changing over the last decades and is changing even more today. These days scientists from all over the world use observatories along the whole range of photon energies to expand the limited picture from just the visible light. Using telescopes in space in addition to their earthbound companions it is even possible to overcome the problem of the limited visibility of the earth's atmosphere and get access to the night sky in almost every wavelength. This is crucial for a complete and self-consistent picture of the astrophysical processes driving the emission of the various sources visible from earth. One of these sources are active galaxies, galaxies whose nuclei emit an extreme amount of energy distributed over the whole electromagnetic spectrum. Following the commonly accepted picture that these galaxies create a so called jet of highly relativistic material, emission up to gamma-ray energies could be observed from these sources. In addition to the pure existence of such high energetic radiation it also shows a high variability leading to the conclusion that this must emerge from a comparatively small region (also known as *blobs*). The origin of this variability is far from understood in complete detail, so that different theories have to be investigated and compared to the increasing amount of observational data.

One of these models is based on the idea of magnetic reconnection, which offers the possibility of a natural explanation of these blobs. It is based on the effect that two strong, antiparallel magnetic fields, which are assumed to be present in the jets of active galaxies, are unstable to the so called plasmoid instability. This instability creates stable magnetic islands called *plasmoids*, which grow in size, are accelerated towards the edges of the reconnection region and show efficient acceleration of single particles to extreme energies inside of the island. The capabilities of this particular type of models is investigated in this thesis by replacing the simulations of magnetic reconnection based on first principles with a Monte Carlo approach, modelling the radiative processes within these plasmoids and studying the light curve after accounting for all the relativistic effects.

One of the best suited instruments for the systematic long-term observation of the gamma-ray emission of such sources is the First G-APD Cherenkov Telescope (FACT). Its extremely stable hardware and dedicated data taking procedure are optimised to yield

an unprecedentedly large and unbiased sample of a few very-high-energy emitters. In order to understand and improve the analysis of this data two further theses together with this one have focused on different parts and introduced a strong collaboration. Marvin Beck optimised the cuts for the background suppression and achieved important progress in the spectral analysis of the fact data (Beck 2019). Fabian Theissen's work led to unprecedentedly insights into the effect of observational conditions on the FACT light curves, which is crucial for a meaningful study of the variability in particular with a focus on periodic behaviour (Theissen 2020). In this thesis, particular attention is payed to the existing Monte Carlo sample, which is inevitable to understand the efficiency of the detector. This offers on the one hand the opportunity to study the behaviour of the analysis steps optimised on data and is on the hand an essential step in the calculation of the spectrum of a source.

1.2. Active Galaxies and Blazars

It is a commonly accepted assumption that a *standard* galaxy consists of a supermassive ($\gtrsim 10^6 M_\odot$)¹ black hole surrounded by ordinary matter in the form of stars as well as dust and some form of dark matter (Kormendy and Ho 2013; Padovani 2017). Depending on their morphology, they can be grouped in categories from spiral galaxies as our Milky Way to elliptical galaxies as our famous neighbouring galaxy M87 (Sparke and Gallagher 2007). However, there is another important difference between the two galaxies, which is the rate at which the supermassive black hole (SMBH) accretes its surrounding matter. While this happens at a rather slow rate in our Milky Way, the centres of some galaxies including M87 show phenomena which are thought to originate from a much extremer accretion rate. In this phase a galaxy is called *active* galaxy and its core region with the accreting SMBH is called active galactic nucleus (AGN). This rather compact picture allows for the emergence of several features emerging, which lead to an even broader variety of observational features. This caused the definition of multiple, historically-grown subclasses of this unified picture, which are summarised for example in detail in Padovani (2017).

One of the most important features is the emergence of fluxes of relativistic material in the form of up to two highly collimated jets (blue to yellow in fig. 1.1). These jets can be resolved in radio observations, when observing the galaxies from the side. Sometimes they create also radio lobes, which can be even bigger than the galaxy itself (shown in yellow on the left side of fig. 1.1) (R. Blandford, Meier, and Readhead 2019). A prominent model to explain the formation of the jet is the Blandford-Znajek mechanism (BZ mechanism) (R. D. Blandford and Znajek 1977), a solution to the electromagnetic structures of a rotating black hole. Using this mechanism energy and angular momentum can be extracted from the rotating black hole, to accelerate stray charges from the accretion disk to radiate off photons which create electron-positron pairs (Dermer and Menon 2009, ch. 16.3). Together with the strong magnetic fields this

¹In the scope of this thesis $M_\odot = 1.988 \cdot 10^{30}$ kg is the mass of the sun.

results in a strong bulk-outflow of electron-positron pair-plasma. It belongs to the class of *magnetospheric* approaches. In contrast to this, there are also ideas based on a *hydromagnetic* jet, where only an accretion disk is needed to fuel a centrifugally driven jet by its rotational energy ([R. D. Blandford and Payne 1982](#)). Soon after these two ideas, also mixtures of the two concepts called *hybrid* or *hydromagnetospheric* arised, see for example [Foschini \(2011\)](#).

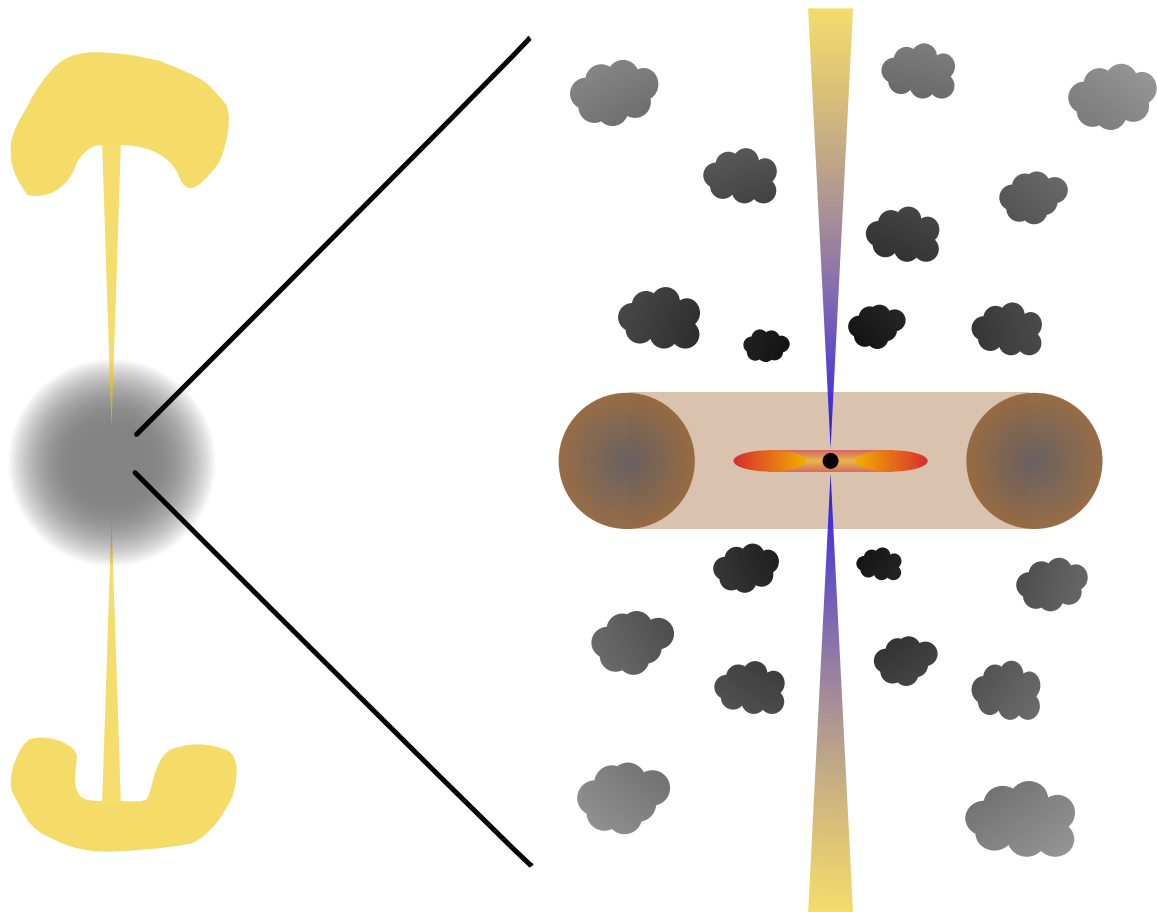


Figure 1.1.: Conceptual sketch of an active galaxy with its nucleus. **Left:** Exemplary elliptical, active galaxy in grey with a jet ending up in a huge radio lobe which can even extend the size of the galaxy itself. **Right:** Zoom into the central region with the supermassive black hole (SMBH) in the center, an accretion disk in red surrounded by a dust torus in brown. Two jets are shown starting close to the black hole in blue and evolving highly collimated, perpendicular to the accretion disk. The clouds represent from dark grey the broad line region (BLR) to light grey the narrow line region (NLR).

The existence of an additional hadronic component in the jet, also called the baryon loading, is still a factor of high uncertainty in many of the current models. Another open question is the acceleration mechanism in the jet. One widely used model is based on the fact that shocks occur in this outflow, which enables the acceleration of charged particles up to even higher energies via diffusive shock acceleration (DSA). However,

there are other processes aside of DSA, which lead to the acceleration of particles. One alternative is the acceleration of charged particles due to magnetic reconnection, which will be discussed in further detail in chapter 3. For other alternatives see [R. Blandford, Meier, and Readhead \(2019\)](#). It is also worth to note that not all AGNs possess two jets, sometimes just one or even no jet can be observed (*jetted* vs. *non-jetted* AGNs) ([Padovani 2017](#)).

For the BZ mechanism it is necessary to have an accretion disk, where the morphology varies between thick and thin disks leading to different effects on the accretion rate and the collimation of the jet ([Longair 2011, ch. 14,21.5](#)). In addition to the accretion disk (red disk in fig. 1.1) an obscuring dust torus (brown) is usually added to explain the features depending on the direct observation of the central region, which can be obscured in some cases.

The last but also very important component are the regions of cloud-like matter around the nucleus. They are divided into the broad line region (BLR) close to the black hole (approximately within $0.1 \text{ pc} \approx 3.1 \cdot 10^{17} \text{ cm}$ ([Longair 2011, ch. 20.3](#)), dark grey clouds in fig. 1.1) and the narrow line region (NLR) further outside (light grey clouds in fig. 1.1). This structure is motivated by two facts ([Longair 2011, ch. 20.3](#)): First, the BLR emission shows variability on small time scales corresponding to a small region such that the BLR is assumed to be located close to the SMBH. Second, the filling factor f of the BLR, which describes how clumpy the gas is,² can be estimated to be very small ($f \approx 10^{-4} - 10^{-6}$) from the optical depth to Thomson scattering and the resulting ultraviolet and optical emission ([Longair 2011, ch. 20.3](#)). The BLR is of course also an emitter of a thermal spectrum.

Putting together all these ingredients, the idea of the unified theory is that the several observed objects differ basically by the viewing angle of the observer, the presence of a jet and the accretion rate of the SMBH ([Urry and Padovani 1995](#)). When looking at the active galaxy perpendicular to the jet, it is typically a prominent emitter in the radio range and thus called radio galaxy. If the accretion rate is rather small and the emission is not dominated by a jet, this yields a Seyfert galaxy of type 2. If rotating the viewing angle from 90° to 45° , the core region is no longer obscured by the dust torus and it is called a Quasar or Seyfert galaxy of type 1, again depending on the dominance of non-thermal emission of a jet compared to the thermal emission of the disk. In the case of the observer looking directly into the jet corresponding to a viewing angle of 0° , the observed object is called a blazar ([Spurio 2015, ch. 9.9](#)).

The blazar class itself is only a unification of several subclasses, where the most prominent ones are flat-spectrum radio quasars (FSRQs) and BL Lacertae (BL Lac). Both show a similar broadband spectrum, but the main differences are that FSRQs are more distant, more luminous and have stronger emission lines ([Urry and Padovani 1995](#)). As the name already indicates, the FSRQs show a flat radio spectrum, where flat is usually defined as a spectral index bigger than -0.5 . The subclass of BL Lacs originates from a former misclassification of the radio emission of the first source as belonging to the variable star BL-Lacertae ([Longair 2011](#)). In the common unification scheme, it is thought

²The filling factor is defined as the fraction of the volume around the nucleus which is occupied by the clouds ([Longair 2011, ch. 20.3](#)).

that the difference between both classes arises due a much higher accretion rate for the FSRQs. This led to the empirical concept of the so called blazar sequence. It was first fitted in [Fossati et al. \(1998\)](#) to the known sources at that time and recently refitted to the third Fermi-Catalogue in [Ghisellini et al. \(2017\)](#) and [Ghisellini \(2016\)](#). Both versions are shown in fig. 1.2. The idea is basically to fit the spectral energy distribution (SED) of all blazars (about 1000) with a double hump structure based on combinations of power-laws, but binned in the luminosity measured by the Fermi satellite. This yields a basic idea of the types of spectra expected from blazars. Concerning the origin of the two humps it is commonly accepted that the first one is the result of the synchrotron radiation of a high energetic electron population. In contrast to that, it is strongly dependent on the model, where the second peak originates from. The most natural concept tries to explain the hump by inverse Compton up-scattering of the synchrotron photons by the same population of electrons (synchrotron self-Compton (SSC) model). Other ideas include the inverse Compton up-scattering of external radiation fields like the Cosmic Microwave Background or the emission by the BLR (external Compton (EC)). Including hadronic processes by increasing the baryon loading of the jet offers further possibilities to create the second hump at high energies. For a detailed review see for example [R. Blandford, Meier, and Readhead \(2019\)](#) and references therein.

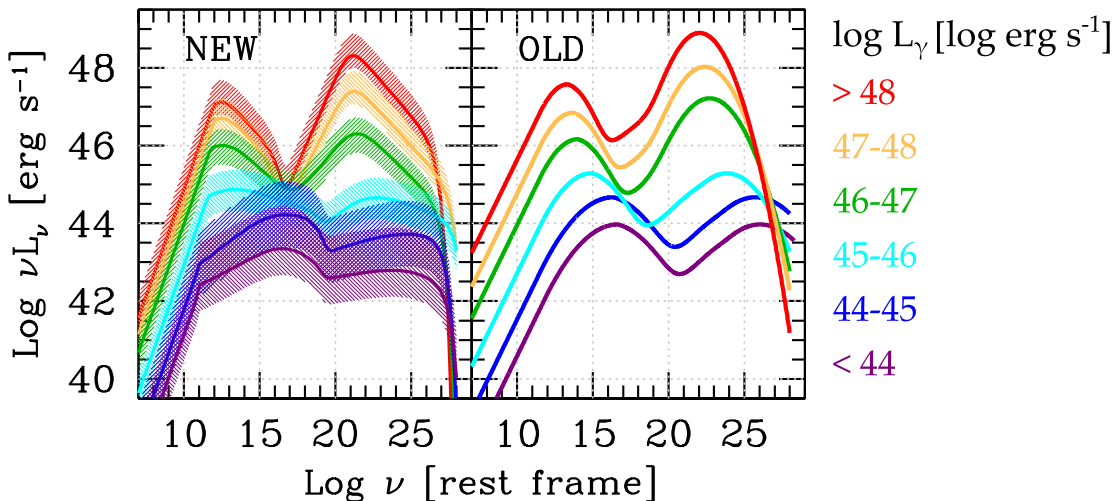


Figure 1.2.: Blazar sequence: The *new* blazar sequence normalised to the gamma-ray luminosity on the left compared to the *older* version classified according to their radio luminosity. Apart from the increase of the emission among all wavelengths also a variation in the spectral behaviour of the two humps is visible. ([Ghisellini et al. 2017](#))

When considering that the bins with higher energies (red, yellow, green) are basically dominated by the population of FSRQs and the lower ones by the BL Lacs, fig. 1.2 indicates three other features: The total luminosity is much higher and the humps are more peaked in case of the FSRQs. Furthermore, the Compton-ratio can be defined as the ratio between the heights of the synchrotron peak compared to the second one probably due to some form of Compton-scattering. It is found to be bigger in the case of the FSRQs, while it is the other way around in the case of the BL Lacs. This leads to the

interpretation that under the assumption of the second hump originating from EC on the BLR the emitting region lies deep inside the BLR for the FSRQs and outside the BLR for the BL Lacs (corresponding to the blue and yellow part of the jet in fig. 1.1).

Observations of blazars are of particular interest due to the high variability of these sources. During so called *flares* the blazars show increased fluxes up to few orders of magnitude higher, which last from minutes up to months. A famous example for variability among the different wavelengths is the BL Lac in the elliptical galaxy Markarian 421 (Mrk 421). Mrk 421 was detected by the Whipple collaboration in 1992 as the first extragalactic emitter in the TeV-range (Punch et al. 1992). With a redshift of $z = 0.03$ it is the closest blazar and has been subject to many multi-wavelength campaigns in the recent years (Spurio 2015, ch. 9.11.2), showing apart from the typical double hump structure also variability on time scales of months with a strong correlation between the x-ray and very-high-energy gamma-ray lightcurves (Ahnén et al. 2016; Sliusar et al. 2019). These multiwavelength correlations impose constraints to the modelling of the underlying physical processes. Other examples of variability going to even extremer values are the BL Lacs Markarian 501 (Mrk 501) (Albert et al. 2007), PKS 2155-304 (Aharonian et al. 2007) and BL Lacertae itself (Arlen et al. 2013) or the FSRQs 3C 279 (Ackermann et al. 2016) and 3C 454.3 (Britto et al. 2016). Modelling these sources is challenging due to variability on such small time scales corresponding to small emitting regions by arguments of causality. One of the key features of the model of magnetic reconnection is its ability to naturally explain the short flares and high variability without the need of expanding the parameter space to poorly motivated regions like ultrarelativistic ($\Gamma \gg 10$) jet Lorentz-factors (Böttcher 2019). Together with the fact that 40 % of the known TeV sources are AGN (González et al. 2019), this motivates the investigation of blazar variability based on a model of magnetic reconnection.

1.3. Detection of Gamma Rays

In the context of gamma-ray astronomy ($E_\gamma > 100$ keV), it is common to distinguish between the energy ranges high-energy (HE) (100 MeV - 100 GeV), very-high-energy (VHE) (100 GeV - 100 TeV) and the ultra-high-energy (UHE) (above 100 TeV). Depending on the energy, different detection techniques are used to account for the decreasing flux at higher energies. Because the atmosphere is opaque to gamma rays, the earth-bound, direct detection of these photons is not possible and the most natural alternative constitute observatories in space. While it is realistic to observe HE photons with satellite-based observatories like the Fermi satellite³, its exposure becomes to small for significant observations at higher energies. This would require either infeasably large detectors or extremely long measurements leading to a coarse temporal resolution and an indistinguishable background.

Thus a different detection strategy is used, which takes the earth's atmosphere as a calorimeter, similar to the detection of cosmic rays at their highest energies. In both cases a primary particle of extraterrestrial origin penetrates the atmosphere and the

³<https://glast.sites.stanford.edu/>

probability of an interaction with a molecule of the air increases due to the increasing density profile. This primary interaction usually takes place in heights of several kilometers and converts the high-energetic primary particle into secondary particles which carry still a significant amount of energy and interact with the atmosphere themselves. This yields a cascade-like distribution of the primary energy into secondary particles, which is known as an extensive air shower (EAS). In the case of an initial photon or another lepton the driving processes in the shower are bremsstrahlung and pair-production and the shower is said to be leptonic since these processes are leptonic. If however, the initial particle is a cosmic ray and already of hadronic nature, this introduces an additional hadronic component usually consisting of pions and a few kaons and other particles. As an example, two EASs by a proton and a photon of the same energy of 1 TeV are shown in fig. 1.3. Although just slightly visible from the images, hadronic showers have a bigger lateral distribution, while the leptonic shower profile is on average denser. The typical scale for a photon is a shower length of about 10 km and diameter of just 20 m. This property is often used to determine the primary particle type, which is, however, very challenging due to the high fluctuation by the stochasticity of the shower. For more details on EASs see common textbooks like [Spurio \(2015\)](#) or [De Angelis and Pimenta \(2015\)](#).

Thanks to the production of EASs, VHE gamma rays can still be detected indirectly due to the huge detector volume the atmosphere offers. In general two classes of the indirect detectors are used. First, water Cherenkov tanks can be used to detect the secondary particles of the showers and effectively become the pixels of a large array taking a video of shower profile at a certain stage. These detectors are usually build at high altitudes to probe the shower as close to its maximum as possible. Examples are the currently observing High-Altitude Water Cherenkov (HAWC) Observatory⁴ in Mexico and its progenitor MILAGRO ([Smith 2005](#)) in New Mexico. They offer a high duty cycle and a large field, but are limited at low energies and in terms of angular resolution.

The second detection method are imaging air Cherenkov telescopes (IACTs), which take advantage of the Cherenkov effect. This is basically the emission of electromagnetic radiation by a charged particle moving faster than the speed of light in its surrounding medium. As most of the secondary particles still carry enough energy to surpass this threshold, they emit light into a cone of opening angle $\alpha_c = \arccos 1/\beta/n$, where β is the velocity of the particle in units of the speed of light and n is the refractive index of the medium. For a secondary particle at a height of 8 km approximating $\beta \approx 1$ one finds a Cherenkov angle $\alpha_c \approx 1$. Because of the energy losses of the particles with proceeding shower development (also called *shower age*), α_c increases with the shower age. If now most of the shower's secondary particles produce Cherenkov light, this still adds up to a (unfilled) cone of emission. However, its form is dominated by the angle of the Cherenkov cone α_c which is larger than the typical angular spread of an electromagnetic shower (about 0.5°). The spectrum of the emission due to the Cherenkov effect is shown for photons of different energies in fig. 1.4 (solid lines). However, it is absorbed by several molecules and scattered by from aerosols in the atmosphere during its way to the ground, which changes the spectrum to the dashed lines. This is the Cherenkov

⁴<https://www.hawc-observatory.org/>

spectrum at a height of 2200 m, a typical height of IACTs. It is peaked in the near UV at around 300 nm to 350 nm with around 100 photons per m^2 reaching the ground. This is called the *light pool*, which form on the ground is to first order still ring-like with a diameter of roughly 250 m, see fig. 1.5.

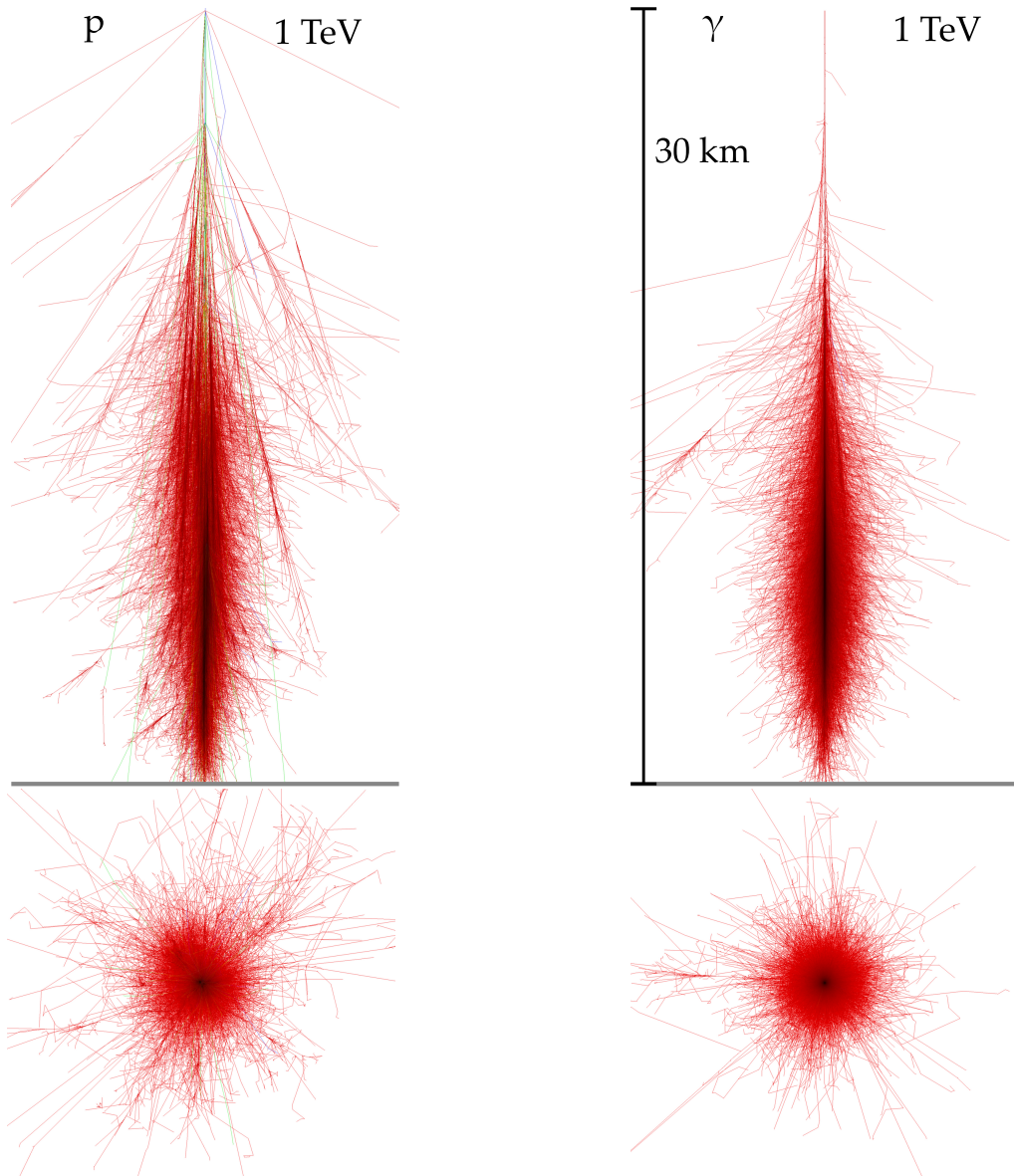


Figure 1.3.: Visualisation of two vertical EAS of a proton (p , left) and a photon (γ , right) with the same initial energy of 1 TeV. The upper plots show the projections parallel to the shower axis, while the lower ones show the perpendicular projections. The electromagnetic component of the shower consisting of electrons, positrons and photons is coloured in red, the hadronic one in blue and the tracks of muons are visualised by green lines. The first interaction happened in a height of 30 km and the simulation stops at the ground (grey line). These plots were created based on simulations of air showers with the CORSIKA software performed by [Schmidt and Knapp \(2005\)](#).

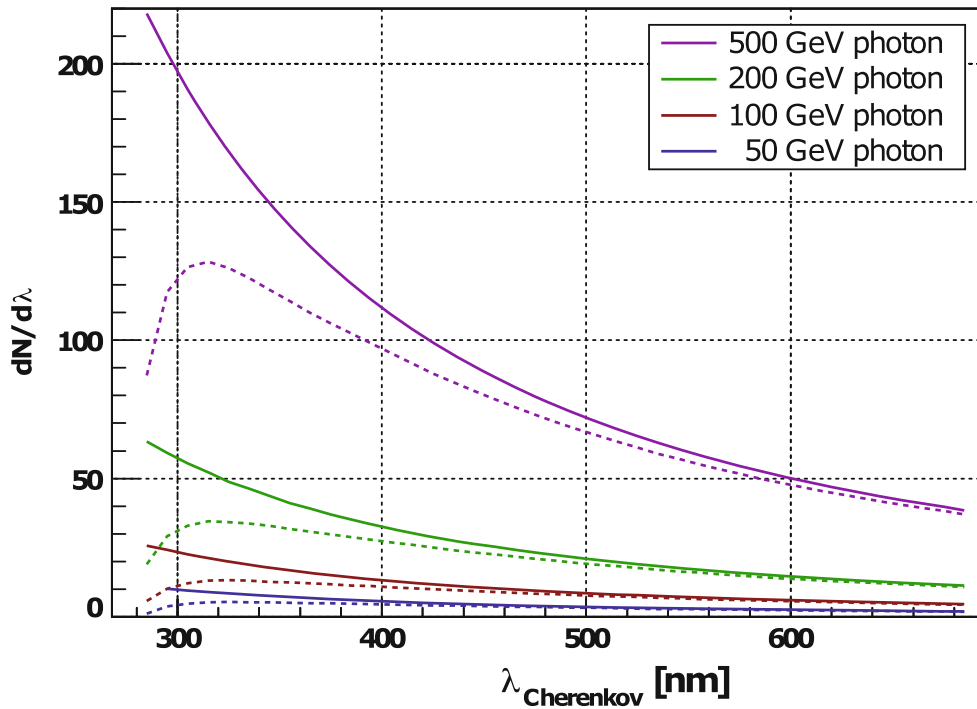


Figure 1.4.: Spectrum of Cherenkov radiation for initial photons of different initial energies. Solid lines correspond to the emission and dashed lines to the spectrum surviving at a height of 2200 m. (De Angelis and Pimenta 2015)

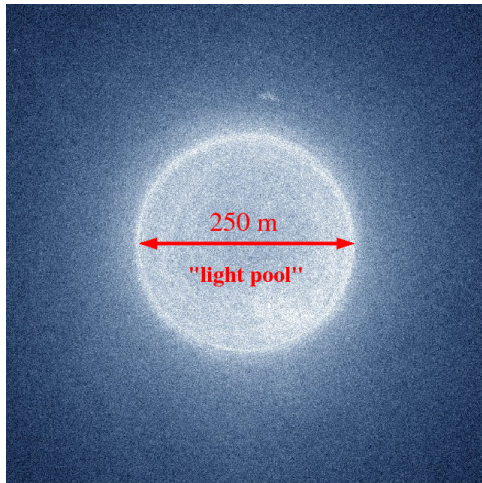


Figure 1.5.: A typical Cherenkov light distribution (Lightpool) arriving at the ground. (Völk and Bernlöhr 2009)

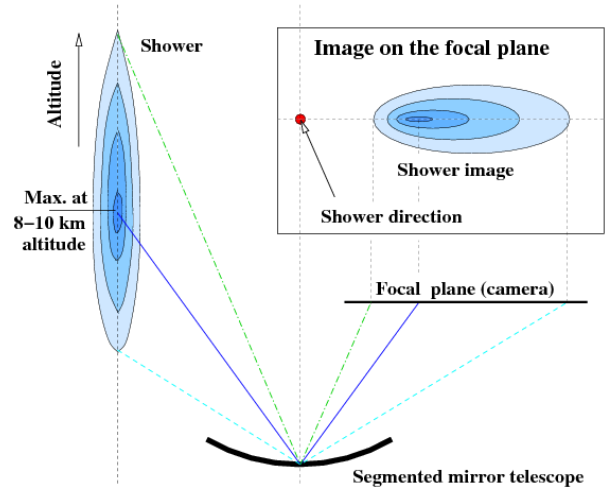


Figure 1.6.: Mapping of the light from the shower to the camera. (Völk and Bernlöhr 2009)

IACTs are then basically taking a "UV-video" of the shower, which later allows the reconstruction of the primary particle's properties. Understanding the time dependent projection of the signal produced by the shower in the camera of an IACT is rather complicated since the high variability in the shower development and geometric effects for

tilted showers (at least up to few degrees) come into play. Nevertheless, the shower image integrated over time can be approximated by an elliptical shape, compare also fig. 1.6. From the total signal in the camera the energy of the primary particle can be estimated and its original direction from the geometry of the shower image, see section 2.8. As the typical duration of an air shower is on time scales of nanoseconds, IACTs need to operate in the GHz range.

The IACTs that were built until today can be grouped in roughly 4 generations. The first generation was the Whipple telescope, constructed in 1968 first with a camera of only one pixel. It then took about 20 years to improve the camera to 37 pixels and the data analysis technique to a level, at which the Crab nebula was detected as the first VHE gamma-ray source (Weekes et al. 1989). This was followed by the next generation observatories, HEGRA at the Roque de los Muchachos Observatory on the Canary Islands and CANGAROO in Australia. HEGRA led to significant progress in the gamma-ray monitoring of blazars until it was shut down in 2002 and the third generation started observations. These consist of systems of multiple telescopes allowing for stereoscopic observations. There exist three main telescopes still in operation today: High Energy Stereoscopic System (H.E.S.S)⁵, Very Energetic Radiation Imaging Telescope Array System (VERITAS)⁶ and the Major Atmospheric Gamma-Ray Imaging Cherenkov Telescopes (MAGIC)⁷. All of these telescopes are mounted on sites with higher elevations and extremely clear observational conditions to minimise the attenuation of the Cherenkov light on its way in the atmosphere. Furthermore, the duty cycle of IACTs is limited to dark, cloudless nights without moonlight, which limits the observation time to 1000 h to 1500 h per year. This is due to the cameras of these telescopes, which consist of 500 to 2000 photo multiplier tubes (PMTs), that can not handle such high light input. In comparison to water Cherenkov arrays, the field of view of typically $5^\circ \times 5^\circ$ is much smaller, but therefore the angular resolution and the duty cycle is extremely high. Furthermore, IACTs have a better energy resolution with a lower energy threshold. A summary comparing both concepts is given in table 1.1.

In VHE gamma-ray astronomy it is very common to use the Crab nebula (usually just

	IACT	Water Cherenkov
Energy range	100 GeV - 50 TeV	400 GeV - 100 TeV
Energy resolution	15 % to 20 %	50 %
Duty cycle	15 %	> 90 %
Field of view	$5^\circ \times 5^\circ$	$4\pi/6$
Point Spread Function	0.07°	0.5°
Sensitivity (in 50 h)	1 % Crab (at 0.5 TeV)	50 % Crab (at 5 TeV)

Table 1.1.: Comparison of the two most common VHE gamma-ray detection methods, imaging air Cherenkov telescopes (IACTs) and water Cherenkov tank arrays. (De Angelis and Pimenta 2015)

⁵<https://www.mpi-hd.mpg.de/hfm/HESS/>

⁶<https://veritas.sao.arizona.edu>

⁷<https://magic.mpp.mpg.de>

"Crab") as a reference, as it is the brightest and therefore first detected source and also quite stable compared to the extragalactic sources like the blazars. The nebula together with the pulsar in its center have been identified to be the remnants of a supernova seen by Chinese astronomers in 1054 AD. Since then the shock front of the supernova explosion is expanding outwards and producing the extremely intense gamma-ray emission. Furthermore, it is located in our Milky Way at a "close" distance of about 2 kpc. For a detailed review of the observations of Crab and their physical implications see [Bühler and R. Blandford \(2014\)](#). With this in mind, it makes sense to express fluxes by different instruments in units of the Crab (CU) and it became common to express also the sensitivity as the detectability of a source with reference to the Crab in times of several hours. The sensitivity of IACTs (at slightly lower energies) is with typically 1 % Crab (at 0.5 TeV) in 50 h an order of magnitude better than for water Cherenkov tank arrays with 50 % Crab (at 5 TeV).

One prototype of a novel technique for next generation IACTs is the FACT, whose camera consists of pixels based on solid state based photo sensors. FACT is discussed in great detail in chapter 2.

The biggest project in the future for the next generation of IACTs is the Cherenkov Telescope Array (CTA)⁸, which is planned to improve the sensitivity by an order of magnitude. CTA will be deployed at two sites, one on both hemispheres, and will consist of tens of telescopes of one of three types optimised to different energy ranges.

⁸<https://www.cta-observatory.org>

2

FACT

2.1. First G-APD Cherenkov Telescope

The First G-APD Cherenkov Telescope (FACT) is an imaging air Cherenkov telescope (IACT) placed on La Palma on the Canary Islands. It is located right next to the MAGIC telescope at the Roque de los Muchachos Observatory at a height of about 2200 m. FACT is installed on a former HEGRA CT3 mount and its mirror surface sums up to an area of 9.5 m^2 , yielding a field of view of 4.5° ([Temme et al. 2017](#)). A photo is shown in fig. 2.1. As the name already indicates, it is equipped with a camera consisting of 1440 Geiger-mode avalanche photodiodes (G-APDs), which are solid state based photo sensors, instead of the commonly used PMTs. They offer a high gain ($10^5 - 10^6$) and can be used under much brighter conditions like even with a full moon. Nevertheless their photon detection efficiency is on the same level as for PMTs. Furthermore the G-APDs are compact and have a low operational voltage ([Anderhub et al. 2013](#)), which makes them perfectly suited for IACTs.



Figure 2.1.: Photo of the FACT telescope.

Motivated by this, FACT was initially intended to be a prototype for these type of light sensors in gamma ray-astronomy. After its installation in 2011, first events could be observed and the concept was proven. From this point on, the data taking has continued until today and got optimised even further, resulting in over 14 000 h of physics data¹. Today FACT collects 2500 h of physics data per year and no decrease in the efficiency of the light sensors has been observed (González et al. 2019; Temme et al. 2017). Figure 2.2 shows the total amount of possible data taking time (nights) over the last 8 yr, where the fraction in grey is dominated by the high background of twilight, the orange one denotes calibration runs to ensure the quality of the physics data in green. The red fraction shows all the other runs performed that do not contribute to the physics data taking.

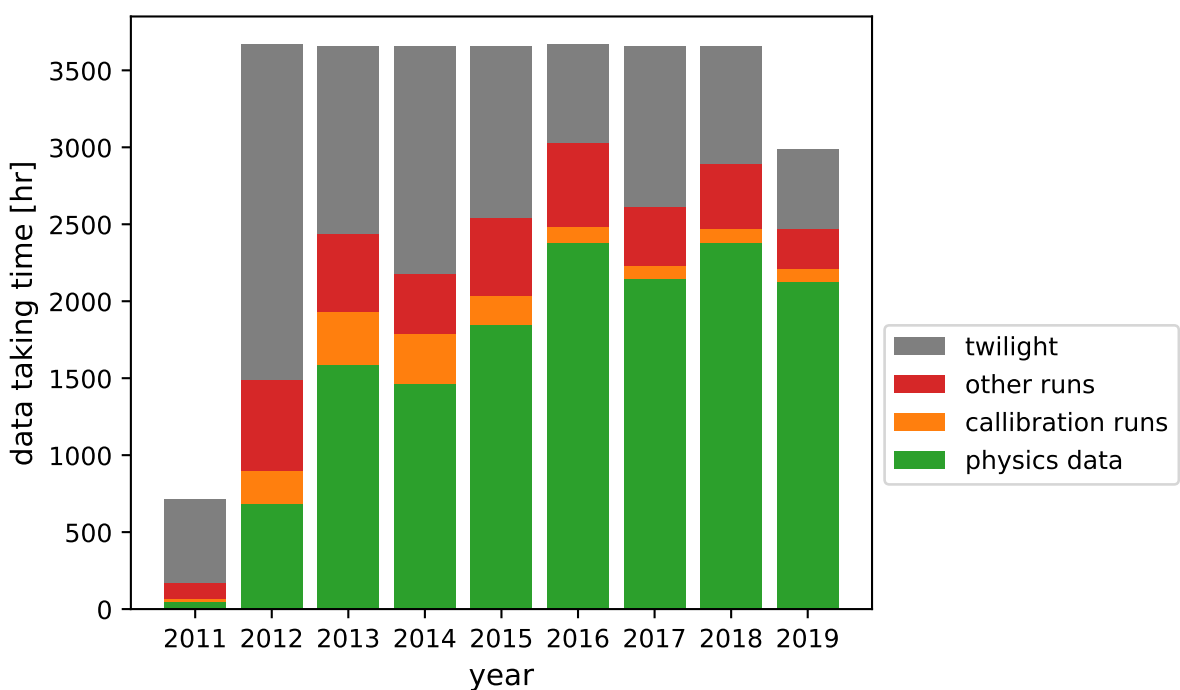


Figure 2.2.: Stacked diagram of FACT’s data taking efficiency per year: From about 3650 possible hours of night time between twilight the green fraction includes only physics data, while the orange fraction denotes all other types of runs for calibrations necessary to take physics data. The red fraction sums up all the other time where FACT was turned on but did nothing related to physics data. The size of the grey parts is affected by the weather conditions as well as technical problems. As it was installed in late 2011 and this plot includes data until November 2019, these bins are smaller than the others. The diagram shows that the amount of collected physics data has increased since the beginning and converged to a value between 2000 h and 2500 h.

In addition to the excellent performance of the G-APDs, the data taking procedure is optimised to yield maximum efficiency. This is achieved by a nearly completely robotic

¹see also https://fact-project.org/dch/obs_time.php

operation of the telescope (FACT Collaboration et al. 2018). Starting from the scheduling of the observed targets which is done automatically by an algorithm based on their visibility and overlaps with other instruments like the x-ray satellites Swift or Chandra, also the shift itself is highly automated. This means that in principle a shift consists of some basic checks for extraordinary issues, for example living beings in the telescope area, which have to be done by a human at the beginning of the night. Then after enabling the power and starting the main script, the telescope follows the schedule and monitors the data taking. In case of extreme weather conditions like high winds or in the case of any other extraordinary issue, the shifter is called on his telephone. Otherwise the telescope can perform the observation for the whole night on its own. At the end of the night the successful parking of the telescope and a quick check for any other undetected events requires the shifter, mainly for reasons of security as the unparked telescope bears for example a high risk of causing fires.

Having this extremely automated data taking procedure in combination with the excellent long-term stability of the photo-sensors, FACT is perfectly suited for the unbiased monitoring of sources. Thus its data taking is dedicated to a small subsample of the brightest gamma-ray sources visible in the sky over La Palma. The Crab Nebula is used as a calibration source, as it is quite common in gamma ray astronomy. Besides this, data taking focuses on the brightest visible blazars, which are basically Mrk 421 and Mrk 501 (both over 3000 h), as well as 1ES 1959+650 and 1ES 2344+51.4 and the Narrow-line Seyfert galaxy 1H0323+342.²

In addition to monitoring these sources, FACT also takes part in the multi-messenger network AMON (Ayala Solares et al. 2020). This means on the one hand sending triggers based on a quick-look analysis (QLA) to the partner observatories, if the observed source shows unknown behaviour like an increased flux during a flare. On the other hand FACT also automatically observes flaring sources, if another observatory triggers the partners of the network. Since AMON unites the most important astroparticle experiments like IceCube, the Pierre-Auger-Observatory, LIGO-Virgo, Fermi, Swift as well as MAGIC, H.E.S.S., VERITAS and HAWC, FACT can give an important contribution to the final goal of a self-consistent picture of blazars by maximising the observed flares and increasing the multi-messenger data-pool.

2.2. Data Taking

The data taking of FACT is structured into runs with a standard duration of 5 min. This is motivated by the fact that the measurement conditions can be approximated as constant within this time range and settings like the threshold can be kept constant. However, at the beginning and the end of the night, twilight causes the background ambient light to change much faster, such that these runs are taken only with a length of 1 min. At the beginning of each run the threshold for each pixel is set to a global value³, based on the measured current in each pixel in the last 10 s. The minimal threshold for individual patches (groups of 9 pixels) can be adjusted, if their trigger rate deviates significantly.

²See https://fact-project.org/dch/obs_time.php for latest numbers.

³There is a lower limit of at least 290 counts of the analog-to-digital converter (ADC).

Additionally, at least every 70 min a calibration run is taken to refresh the calibration of the whole trigger logic⁴.

To get a better estimate of the background, FACT takes its data in the so called *wobble* mode. This means that the telescope is not pointed directly to the source, but in a way that the source position lies a bit off the center. In fig. 2.3, all the pixels of the camera are shown and the source position is indicated by the red dot. Due to the symmetry of the hexagonal structure of the camera, there are exactly five equivalent points (grey), which do not point to the source, but in general to a position without any source. They can then be used to get a simultaneous probe of the background. The offset to the center is chosen to be 0.6° and is used for four runs (20 min), then the opposite wobble point is used. By this, the effects of any observational bias are minimised.

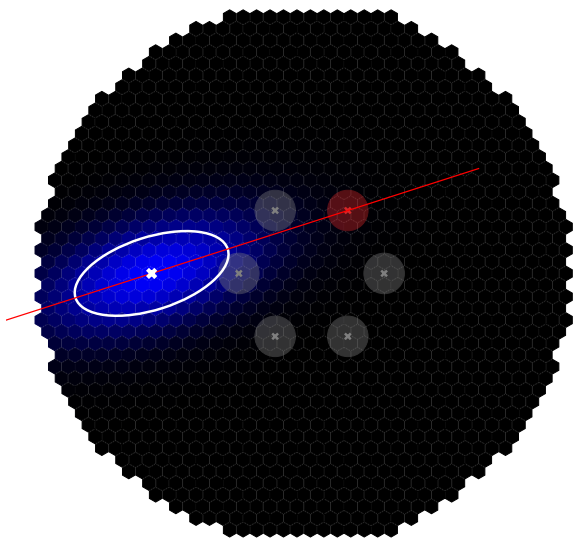


Figure 2.3.: Conceptual plot of the integral signal of each pixel from no signal (black) to a high signal (blue). The red cross marks the position of the source and together with the five grey dots of the equivalent background positions these make up the wobble points. The circles around the crosses illustrate the size of the cut on the arrival direction (section 2.9). The signal is constructed of only an idealised, elliptical image of a shower along the red shower axis pointing perfectly to the source position and without any detector noise.

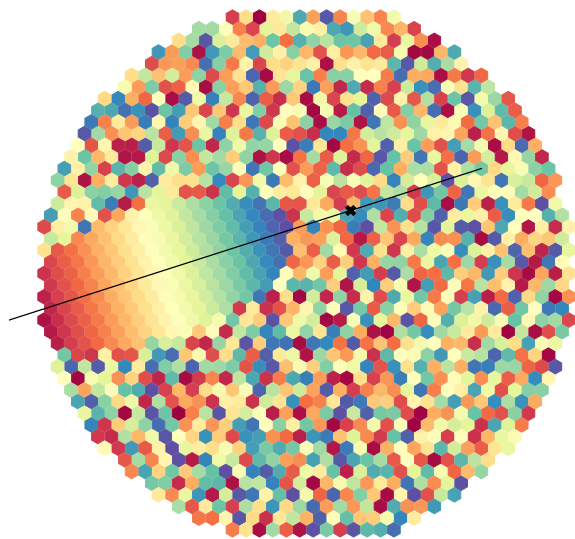


Figure 2.4.: Conceptual plot of the time information of the maximum of the signal in each pixel from early (red) to late (blue). In addition to an idealised shower along the black axis showing a clear temporal evolution there is also a background noise added to the other pixels.

⁴There are also additional conditions for the scheduling of a calibration run like large steps in the observed position when looking for example at another source

2.3. From Light in the Camera to an Image

During one data run there is continuously light arriving at the pixels of the camera. A key step is now to choose the best conditions to trigger, which is done already on the hardware level for FACT. Detailed information on the trigger logic with all the hardware specifications can be found in [Anderhub et al. \(2013\)](#). The basic concept consists of the four trigger entities shown in fig. 2.5: A single pixel yields a certain charge, peaking at the time at which the shower arrives. Nine pixels are grouped together to a so called *trigger patch*, whose integral charge is calculated and then used to define a baseline and an amplitude of the event. Then four trigger patches built up one *trigger unit* and the whole camera consists of 40 of these trigger units.

Figure 2.6 shows a schematic of the trigger logic. For each of the trigger patches of one trigger unit the signal of all pixels is first preamplified (grey) and then linearly added (orange) as mentioned before. This integral signal is then compared to a threshold (brown) and then a 1-out-of-4 selection⁵ within one trigger unit decides whether a digital trigger signal is send to the trigger master or not. On top of the linear addition the signal of each single pixel is also split up into a differential signal (dark grey) to feed a ring buffer (DRS4, green), which continuously contains the data of the last 512 ns in steps of 0.5 ns corresponding to a sampling frequency of 2 GHz. If the trigger master receives now a trigger from one of the 40 trigger units, it will trigger the readout of the ring buffer after a certain delay chosen to center the signal in the read-out range. Additionally, a time marker is added to the analogue signal of each of the pixels after a second delay, chosen to place it after the signal and with the intention to improve the synchronisation. Then the last 300 values corresponding to the last 150 ns are converted to a digital signal using an analog-to-digital converter (ADC).

Having now digitised the temporal evolution of the charge in ADC-counts in each pixel, this data is extremely compressed by the signal extraction. To achieve a high compression, the maximum value for each pixel within 12.5 ns and 112.5 ns is defined as its *signal s*. This is then converted to a photon equivalent using a calibration factor by a program called `callisto`. From the maximum it is checked backwards in time, where the signal decreases for the first time below half of the maximum value. This is called the *arrival time* t_a .

This trigger logic and signal extraction can also be mimicked by a dedicated software trigger algorithm, see [Hildebrand et al. \(2017\)](#). It determines the trigger patch with the highest amplitude and returns this amplitude, the time of the maximum value and the baseline (compare also fig. 2.5). This allows also to calculate the number of events which would have passed an arbitrary threshold and by this apply an additional virtual threshold (higher than the hardware threshold).

As a next step, the image cleaning algorithm star of the Modular Analysis and Reconstruction Software (MARS) ([Bretz and Dorner 2010](#)) generates an *image* from the preceding results by dividing the pixels into islands based on spatial and temporal information and keeping only the pixels in islands surviving certain cuts. Therefore, an iterative procedure is used, which starts with combining all pixels to an island that ful-

⁵At least one out of four.

fil the following condition based on their differences in the arrival times $t_{a,i}$ and their distances in the camera position projected to the sky \mathbf{r}_i :

$$\frac{t_{a,i} - t_{a,j}}{|\mathbf{r}_i - \mathbf{r}_j|} \leq 18.75 \text{ ns/deg} \quad (2.1)$$

If no neighbouring pixel fulfils this condition, also a single pixel can constitute an island. Then the minimal and maximal arrival time of these islands are compared to those of neighbouring islands and in case these values overlap they are merged. This is repeated as long as no further mergers are possible and all the pixels outside of the islands are dropped as noise. The concept of this procedure becomes clearer, when looking at fig. 2.4, where the arrival times of an idealised shower are shown. The elliptic approximation of the light from the shower is clearly correlated in space and time, while this is not the case for the randomly distributed pixels dominated by noise. Next, the *size* s_{isl} of an island is defined as the sum of the signals of its pixels and a cut on this value is applied ($s_{\text{isl}} > 25$). This removes small, potentially random islands. The remaining pixels are then saved as the image. Real images can be explored using the FACT Event viewer⁶.

⁶<https://www.fact-project.org/viewer/>

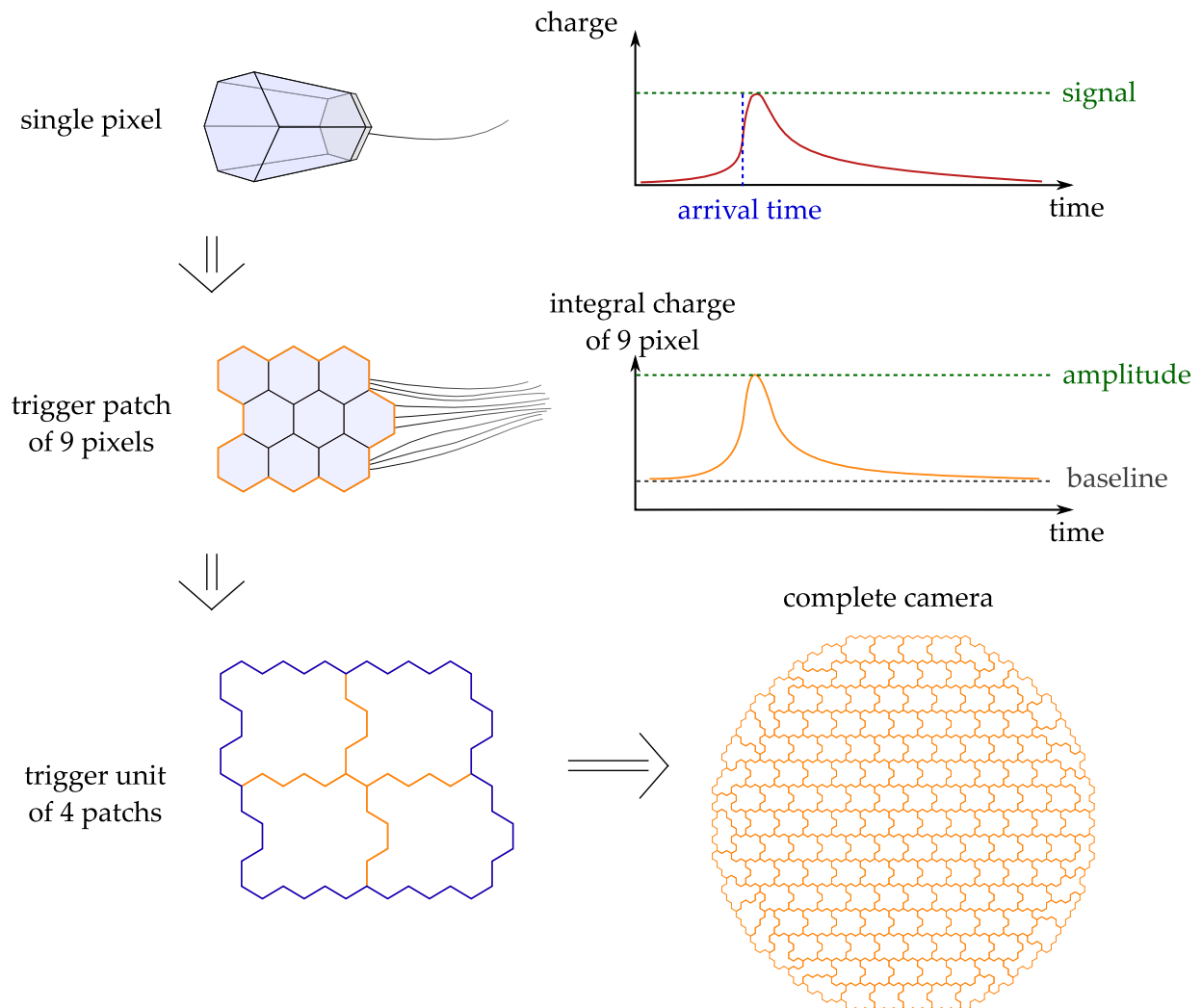


Figure 2.5.: Trigger entities of FACT: A single pixel with its typical signal, a trigger patch consisting of 9 pixels with a typical integrated signal defining the baseline and the amplitude of a patch, a trigger unit consisting of four trigger patches and the whole camera divided into its trigger patches.

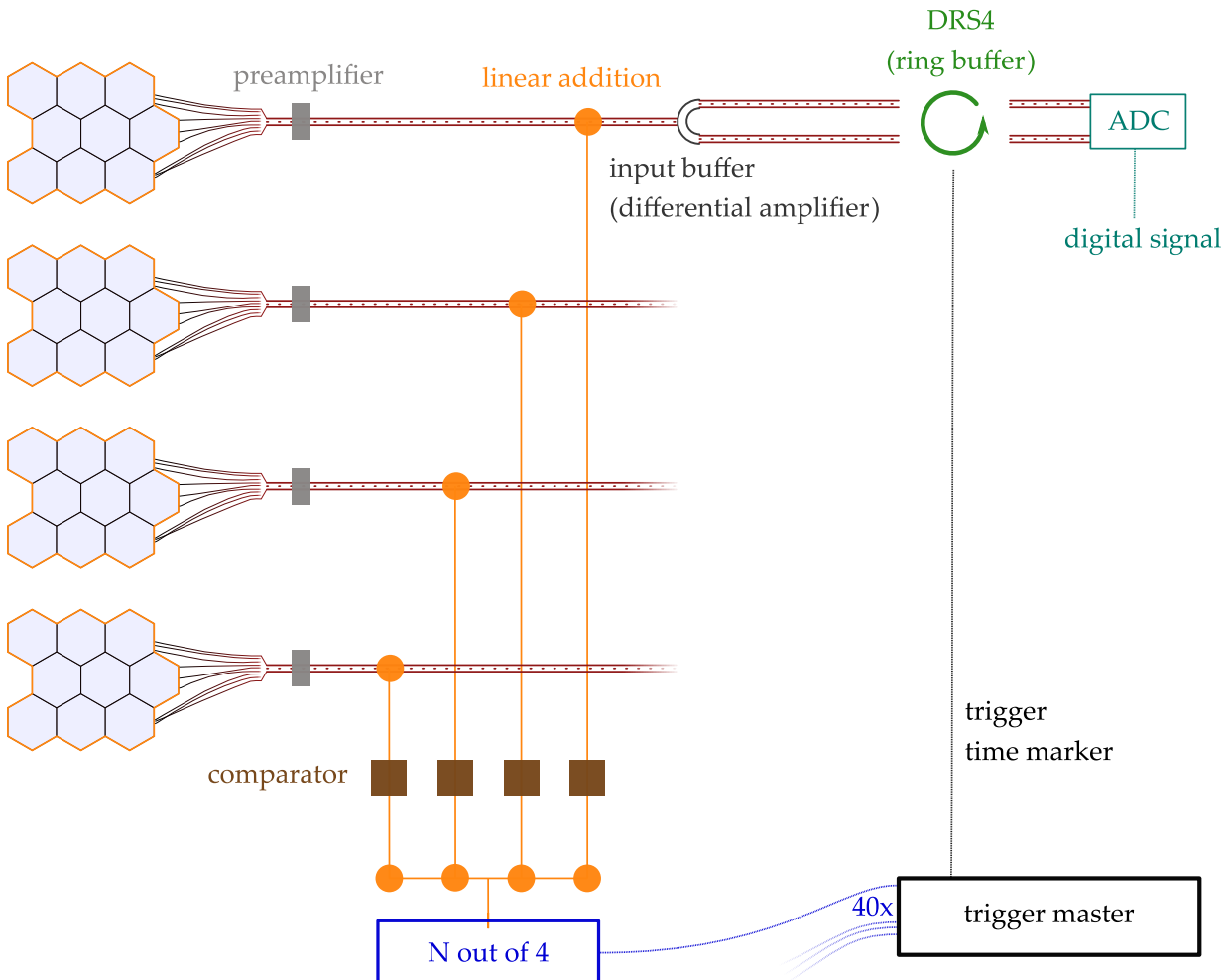


Figure 2.6.: Trigger logic of FACT: The signals of the pixels of four patches are preamplified each (grey), linearly added (orange) and compared to a threshold (brown). Based on a N-out-of-4 logic (blue) where N is usually set to 1 a digital trigger signal is sent to the trigger master (black). On top of the linear addition the signal of each pixel is split to differential signal (dark grey) to be buffered by a DRS4 ring buffer (green). It is read out and digitised by an analog-to-digital converter, once a trigger signal from the trigger master arrives. In addition to the trigger signal the trigger master also adds after a certain delay a time marker to signal of one channel of each pixel as a crosscheck of the synchronisation.

2.4. FACT Monte Carlos

Using the COsmic Ray SImulations for KAscade (CORSIKA)⁷ software, the development of an air shower can be simulated. The Modular Analysis and Reconstruction Software - Cherenkov Observatory edition (MARS-CheObs) package allows then to process these showers using a simulation program called CERES (Camera Electronics and REflector Simulation) (Bretz and Dorner 2010). As the name indicates, CERES simulates the reflection in the mirrors, the properties of the light collecting cones, the production of an electronic signal in the G-APDs and the trigger electronics. The results are processed with the same analysis software as the data and saved into output files, which have been included into a SQL-database. This results in an easy and universally accessible way of storing the data.

A Monte Carlo (MC) sample of $6 \cdot 10^7$ showers has been created in this way for a given parameter space of initial photon properties. The three most important ones are the initial photon energy E being varied between 0.5 TeV and 20 TeV, its zenith distance Zd from 0° to 60° and its impact parameter from 0 m to 540 m. The impact parameter is defined as the shortest distance between the telescope and the shower axis, see fig. 2.7. As for real data, data taking for the MC events is performed in wobble mode, such that the source position is slightly off the camera's center.

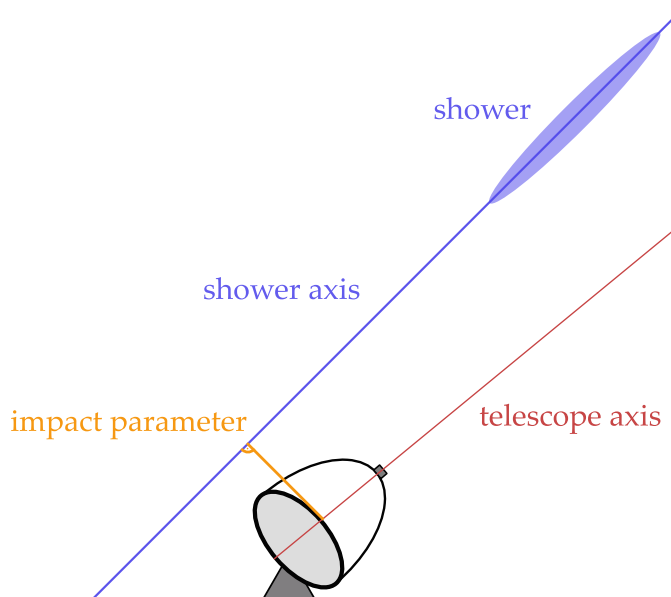


Figure 2.7.: Sketch of the telescope illustrating the definition of the impact parameter.

In analogy to the distribution expected from data, not all of the parameters for the MCs are sampled uniformly. However, the distribution of a quantity can still be changed by so called *reweighting*. For that, a weight is added to each event depending on its property. This changes the initial distribution of this property to any arbitrary distribution

⁷<https://www.ikp.kit.edu/corsika/index.php>

as long as at least a few events at each position in the parameter space are present (zero events can not be reweighted to any other number). This offers the advantage of reusing the same sample of computationally expensive MCs for different analyses. Nevertheless this has also limitations, since the statistical uncertainty at one point in the parameter space is driven by the number of originally simulated events. The uncertainty of each reweighted bin N_r is calculated from the old bin N by neglecting the uncertainty on the weight: $\sigma_{N_r} = N_r / \sqrt{N}$.

As typically for the cosmic ray spectrum, in case of the energy a power law distribution with a spectral index of $\gamma = -2.7$ has been simulated. It corresponds to a realistic distribution, but also suppresses the statistics strongly at high energies. This motivates the production of the MCs with a smaller spectral index of $\gamma = -1$. It results in an evenly sampled distribution in logarithmic energy bins with the same statistics at high energies as in the low energy range. Because FACT's reference source, the Crab nebula, has a spectral index of about -2.5 in VHE gamma rays (Nigro et al. 2019) this is chosen as a representative value. The spectra of for example the Markarian blazars tend to be a bit softer, and an additional representative value -3 is added to fig. 2.9. The spectra are assumed to follow a simple power law. For the impact distribution a linear dependence has been chosen. This corresponds to a uniform distribution in the cross sectional area along the telescope axis:

$$\frac{dN}{dA} = \frac{dN}{2\pi r dr} = \text{const} \quad \Rightarrow \quad \frac{dN}{dr} \propto r \quad (2.2)$$

The produced distribution is plotted in fig. 2.9.

In case of the origin of the particles there are in general two degrees of freedom, its Zd and the azimuthal angle. CORSIKA is able to include the effects of the geomagnetic fields and CORSIKA-simulations are therefore always done with respect to the magnetic north pole. The difference to the true north is called magnetic declination and for La Palma slightly below -7° . However, for these MCs only showers coming from one azimuth, the magnetic north at about -173° , and along a line in Zd are generated.

For the zenith distance a uniform sampling makes sense, to gain insights into the telescopes performance at all zenith distances with the same amount of statistics. However, the produced distribution shown in fig. 2.9 is affected by several effects from the production. The lower plot shows the intial distribution and the ones after each additional correction on top. Black lines denote a Possionian uncertainty. It was produced with CORSIKA in subsets of 1° with 1000 to 6000 runs consisting of 3000 events each. In fig. 2.8 the Zd -range is shown for each run identified by the ID of the file. It can be seen that the production happened in the subsets indicated by the grey bands with their corresponding name, which are further divided into a number of runs at each zenith bin. The first effect which explains the "oscillatory" behaviour of the MCs is due to the fact that CORSIKA uses a distribution which is uniform in $\cos Zd$ corresponding to a uniform distribution in solid angle for *each* 1° -bin. This explains the rising slope with decreasing amplitude in especially the first bins. In addition, CORSIKA adds another weight of $\cos Zd$ since it is designed for a flat detector. This yields a total weight of $\sin(Zd) \cos(Zd)$ normalised for each bin of 1° , which looks like an oscillation. The sec-

ond effect is that the two bins 29° - 30° and 59° - 60° have significantly less counts, which is simply due to the fact that there were less runs produced for the last Zd -bin of each sample. By counting the bins, the fractions can be determined to be 57/67 and 427/537.

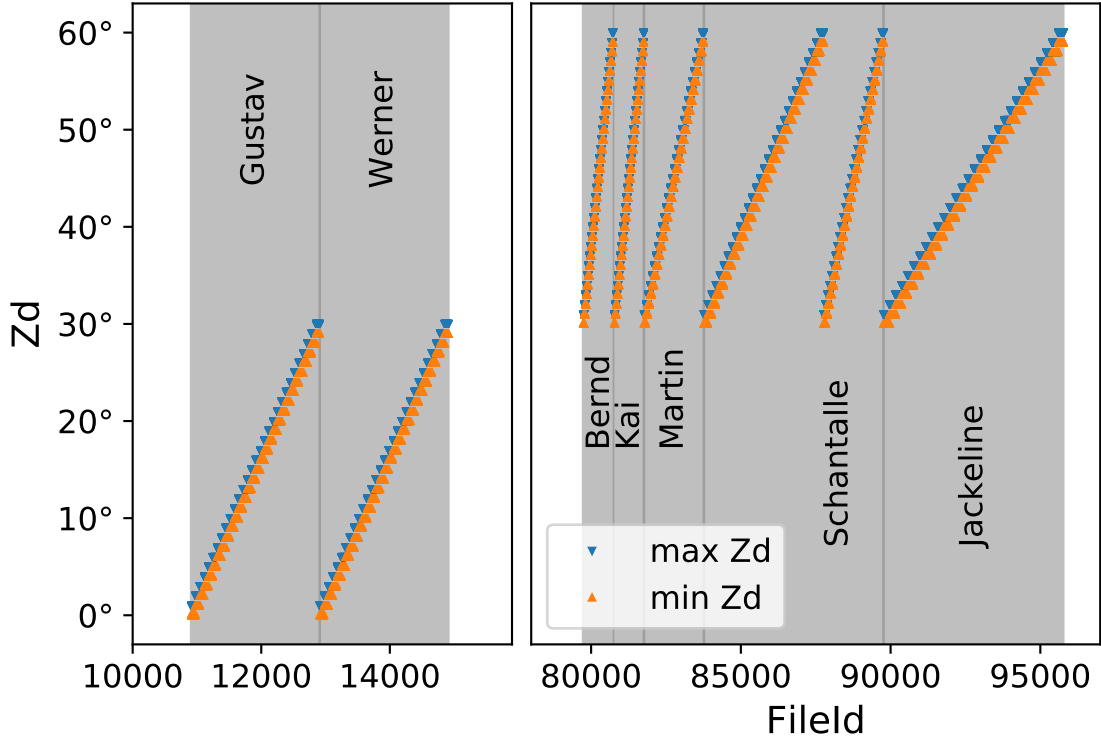


Figure 2.8.: File IDs for the different runs during production of the MCs with their Zd -range. Note that a single run consisting of 3000 showers is denoted by two triangles and each step in the plot consists of multiple triangles. The subsets in which the MCs are produced are indicated by the grey names and marked with their name.

In addition to this, another feature is visible in the distribution of Zd as well as the impact parameter. Both show a systematic decrease at low Zd and high I , belonging to one quarter of the parameter space in these two variables (compare also fig. 2.11). This part of the parameter space has been left out under the assumption that FACT nearly does not trigger any of the huge amount of showers. This seems to be validated by the result for the trigger efficiency shown in fig. 2.11. Nevertheless, these non-triggering, non-produced events have to be taken into account for a comparison to the surviving events at a later stage. The most natural form to correct for this effect would be to sample these events according to a uniform distribution within 0° and 30° or 270 m and 540 m. However, in this thesis a similar approach is chosen by reweighting the distributions of Zd and I with a correcting factor, which increases the fluctuations. Additionally the uncertainties are plotted in black.

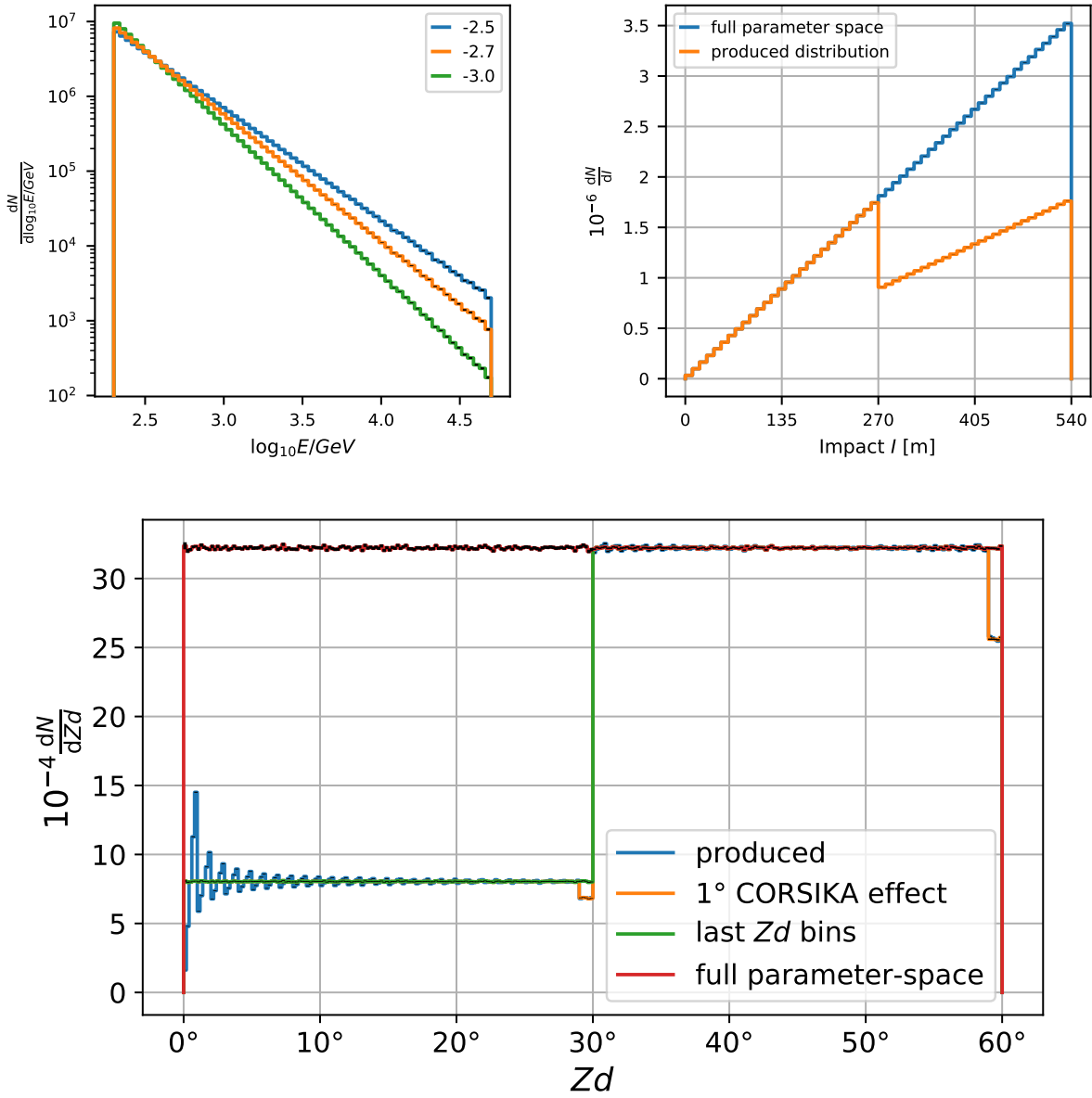


Figure 2.9.: MC distribution of the energy (upper left), impact parameter (upper right) and zenith distance (lower) of the originally simulated initial particles. For all three distributions weights are introduced to account for effects from the production.

In the next step, each shower is processed once by CERES in the wobble mode with a uniformly distributed position in a wobble ring of radius 0.6° and the standard analysis chain until the image cleaning is applied afterwards. This smears out the telescope Zd -distribution of each 1° -bin by 0.6° in both directions. Thus, a comparison between the originally produced MCs and the surviving ones at any later stage needs to be done in bins of the particle Zd . This does not affect the results strongly, but reduces the systematic uncertainties. However, the cut efficiencies afterwards are then given in terms of the telescope Zd and the effect cancels out.

The resulting distributions are reweighted to a power law with slope -2.5 in energy and shown in fig. 2.10. The plot still shows the features of the original MCs. The given 2D distributions show that most of the overlap of parameter space and the detector's sensitive range is included. However, already extrapolation by eye indicates that the number of events that trigger the detector has not decreased completely to zero at most of the boundaries of the simulated parameter space. This introduces systematic effects in the interpretation of the MCs. To fully evaluate this, the efficiency of data acquisition and the complete analysis is needed. This reduces the relevant parameter space further and has to be used to conclude, if an extension to a bigger parameter space is still necessary.

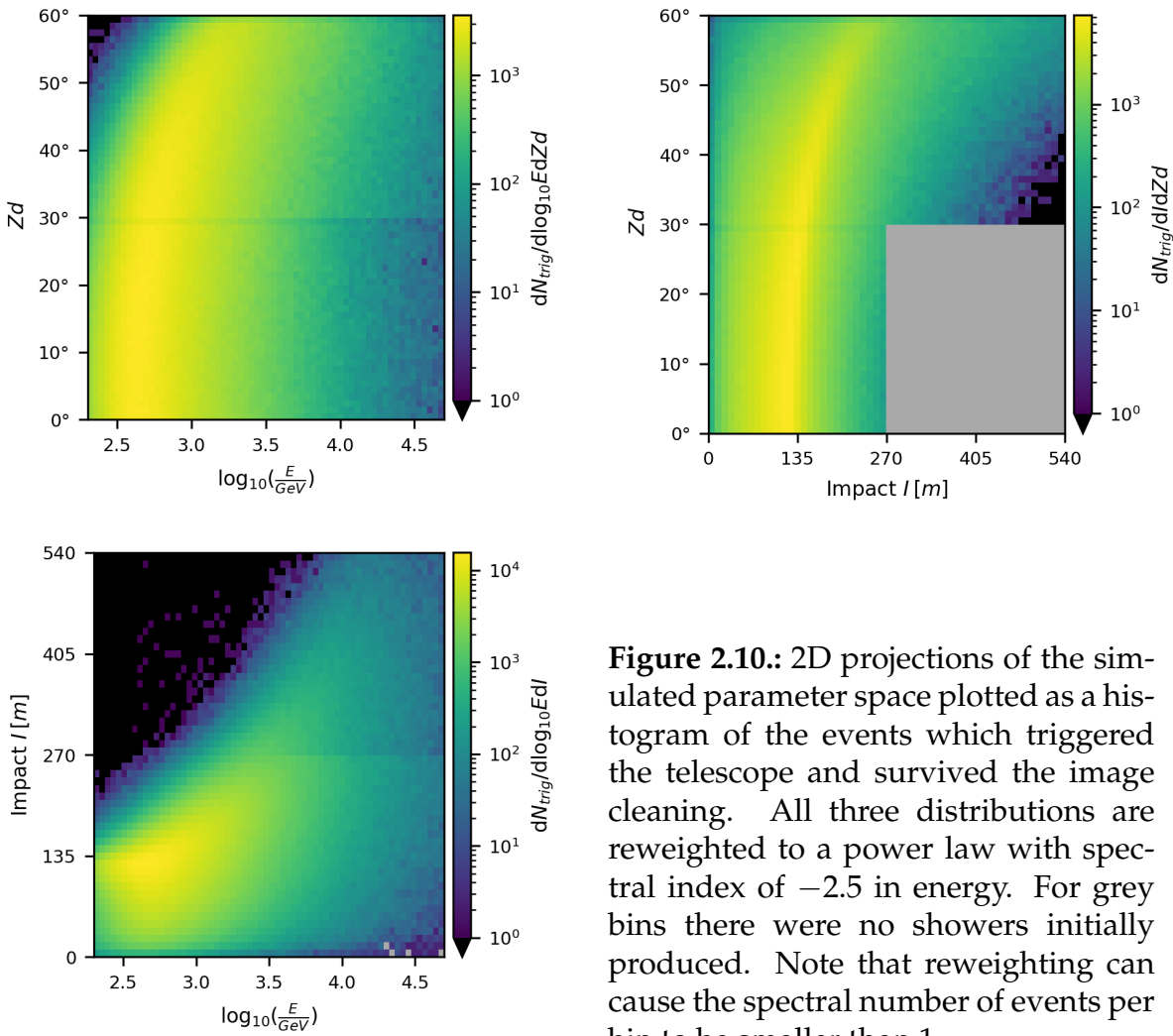


Figure 2.10.: 2D projections of the simulated parameter space plotted as a histogram of the events which triggered the telescope and survived the image cleaning. All three distributions are reweighted to a power law with spectral index of -2.5 in energy. For grey bins there were no showers initially produced. Note that reweighting can cause the spectral number of events per bin to be smaller than 1.

For a future production of new MCs, an adaptive algorithm might be more efficient to scan the parameter space systematically. This would divide the parameter space into hypercubes and extend the simulated region based on a feedback from the efficiency of the telescope in that area. This feedback could be for example the efficiency after the

data acquisition and all analysis cuts and a minimum value could yield a condition for a further expansion into adjoining regions. In all regions behind these boundaries the efficiency is approximated to be zero. This procedure would also offer an estimator of the systematic uncertainty from the threshold efficiency. Nevertheless, a dependency on the chosen energy spectrum and the parameters of the analysis remains.

2.5. Trigger Efficiency from Monte Carlos

In order to calculate a trigger efficiency for gamma rays from one source position one would naturally just produce a large amount of showers from that position and "wobble" around the source position. Assuming that the variation due to the rather small angular wobble ring is negligible, one would obtain a mean efficiency along this ring by the fraction of surviving events compared to the number of produced ones. For the given MC sample this would imply to take all showers that are produced from the position of interest, where the telescope performed the observation in the correct wobble position. But since the MCs are produced already with systematic effects that can be neglected for a 1° binning in Zd , another approach is chosen: The trigger efficiency is calculated in exactly the Zd bins, for which the number of initially produced showers is known to be always 3000 and the number of triggered ones is known as well. From these two numbers, the efficiency can be calculated for one run corresponding to only one Zd -bin. This has the advantage that the two artefacts in the Zd -distribution, the additional reweighting of each 1° -bin and the two bins with less produced showers, cancel out and do not have to be corrected for the efficiency. Note that the term triggered means in this context that an event triggered the telescope and survived the image cleaning.

The results are shown in the form of 2D-histograms of the distributions binned in energy, Zd and I in fig. 2.11. Already at first glance the structure of the non-produced showers can be seen as an artefact along the axes of Zd and I . This means, there are in fact some events in this parameter space, which would have triggered and are missing now, since the efficiency is approximated to be already exactly zero (grey region in the upper right of fig. 2.11). Nevertheless, this effect is assumed to be just a small correction to impact values above 270 m and zenith distances below 30° (indicated by the red lines).

In the upper left of fig. 2.11 the efficiency binned in energy and Zd is shown. Interpreted as a sliced energy distribution, it can be seen how the energy threshold rises with Zd . This was also seen in [Beck \(2019\)](#) and can be understood by the higher attenuation of the light of showers passing a longer distance through the atmosphere at higher Zd . The fact that the energy threshold starts to deviate significantly above about 40° is also consistent with the behaviour seen in data, compare also [Theissen \(2020\)](#).

From the plot on the lower left it can be seen that for high energies above about 10 TeV the showers start to trigger even at impact parameters of 540 m. This means that systematic effects due to the missing simulated parameter space arise for the trigger efficiency. However, it is important to notice that these few events do not survive the cuts of the complete analysis process and it is thus not necessary to simulate this region of the parameter space.

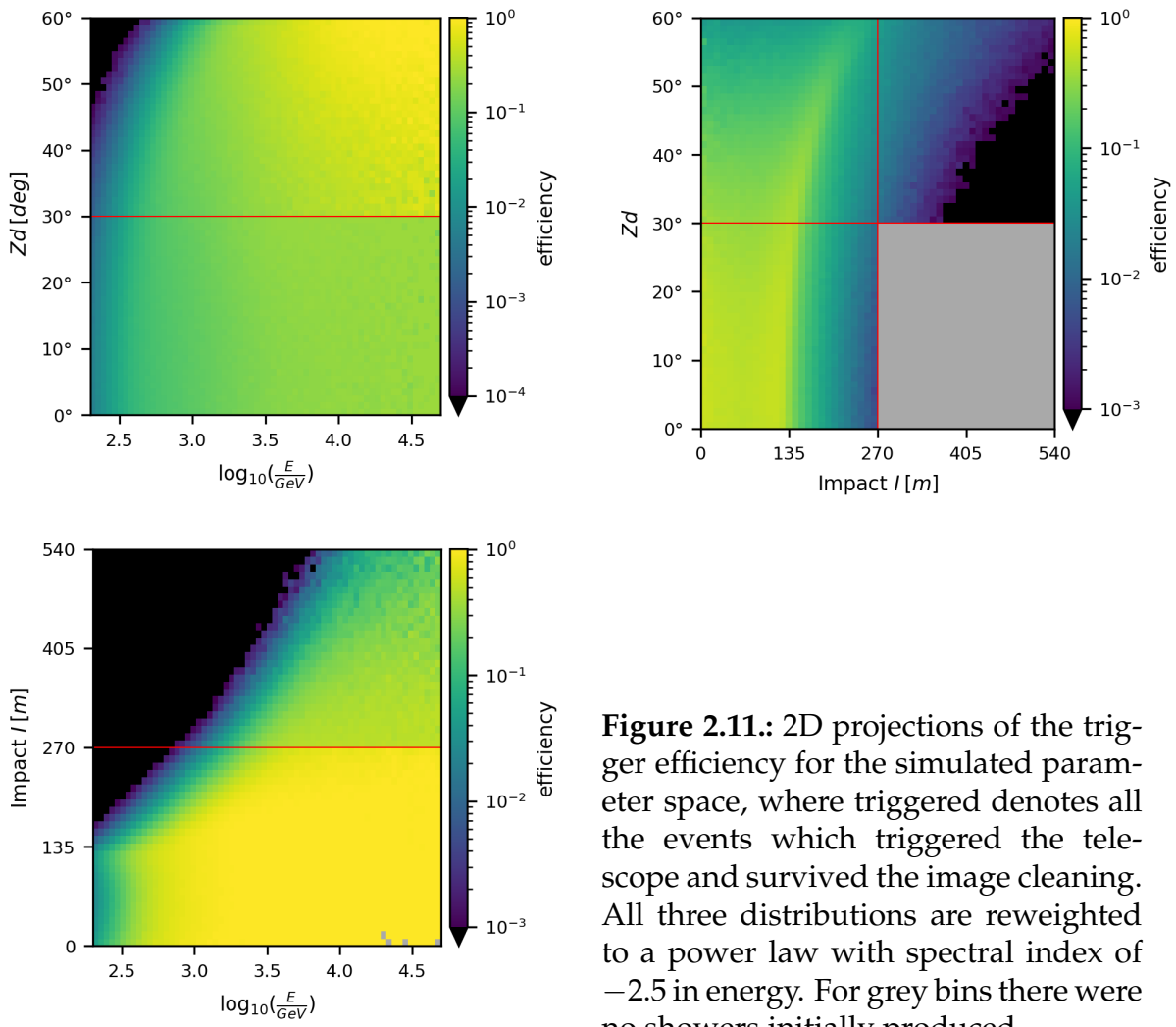


Figure 2.11.: 2D projections of the trigger efficiency for the simulated parameter space, where triggered denotes all the events which triggered the telescope and survived the image cleaning. All three distributions are reweighted to a power law with spectral index of -2.5 in energy. For grey bins there were no showers initially produced.

2.6. Cut Efficiencies and Uncertainties

It is a common thing to apply a cut on a certain variable in a distribution of some data and bin it in another variable to understand the physical impact of the cut. This results usually in two identically binned histograms, one before the cut and one after its application. The efficiency of the cut in each bin is then defined as the fraction of the number of counts in these bins. As summarised by Paterno (2004), the underlying probability distribution to estimate the uncertainty on the cut efficiency can be obtained by Bayesian statistics. Since neither the Gaussian propagation of the Poissonian errors of the two histograms ("Poisson approach") nor the approximation by the uncertainty of a binomial process with the true passing probability replaced by the estimated one ("binomial approach") behave in a sophisticated manner, a different approach is motivated. This is done by starting from a binomial distribution, which is then "inverted" via Bayes theorem to be interpreted as the probability of a true efficiency ϵ given that k events out

of N passed the cut in one bin:

$$P(\epsilon|k, N) = \frac{\Gamma(N+2)}{\Gamma(k+1)\Gamma(N-k+1)}\epsilon^k(1-\epsilon)^{N-k} \quad (2.3)$$

Here $\Gamma(n) = (n-1)!$ is Euler's gamma function, which comes in with the normalisation when choosing a uniform prior between 0 and 1. This still features a maximum at $\epsilon = k/N$ and the probability density function (PDF) can be numerically approximated by fast implementations of the incomplete beta function $B(x, a, b)$:

$$B(x, a, b) = \int_0^x t^{a-1}(1-t)^{b-1}dt \quad (2.4)$$

The uncertainties are then calculated as the values σ_{up} and σ_{low} , which include 34.13 % ($\sigma/2$) of the PDF:

$$\epsilon = \frac{k}{N} \quad a = k+1 \quad b = N-k+1 \quad (2.5)$$

$$B(\epsilon, a, b) - B(\epsilon - \sigma_{\text{low}}, a, b) \stackrel{!}{=} 0.341344745 \quad (2.6)$$

$$B(\epsilon + \sigma_{\text{up}}, a, b) - B(\epsilon, a, b) \stackrel{!}{=} 0.341344745 \quad (2.7)$$

In the special cases $\epsilon = 0$ and $\epsilon = 1$ this definition has to be adjusted to ensure $\epsilon \pm \sigma_{\text{up}/\text{low}} \in [0, 1]$. Instead of a symmetric interval, the same condition for a one-sided interval with double size 0.68268949 is chosen. This differs slightly by the approach suggested in [Paterno \(2004\)](#), but yields still an adequate parameter to estimate the width of the distribution and is computationally much easier.

2.7. Quality Cuts

To ensure quality of the data, three further cuts are applied. The first of these quality cuts is a restriction on the number of islands per shower to be less than three. This helps mainly to sort out triggered images, which do not belong to a shower, but are random coincidences surviving up to this stage. Furthermore, it suppresses hadronic showers, which have a larger spread. The second cut requires a minimum number of five pixels per shower to ensure a proper reconstruction of the image. The third cut is based on the Leakage1 parameter, which is defined as the fraction of the shower's size that lies on the outermost ring of pixels. This is a commonly used quantifier for how much of the complete image is lost, because it lies out of the camera. The cut on leakage is chosen to discard events above 10 %. The distributions of all three parameters are shown in fig. 2.12 and the cut values are indicated by a black vertical line. In fig. 2.13 the corresponding cut efficiencies binned in energy, zenith distance Zd and impact parameter are shown for the application of each cut alone. In general it can be seen that most events survive all cuts. It can be furthermore seen that the cut on the number of islands rejects especially events at low energies, which produce fainter and smaller images consisting

of less pixels. All three cuts seem to be rather independent of Zd . The most events are lost due to the Leakage1 cut, which rejects especially at high energies and impact parameters. This can be understood by the fact that these showers are typically very bright and thus large and also tilted. This makes it more probable that the shower lies only partially in the camera.

The Zd and the I histograms still indicate an artefact at the edges of the non-produced corner of the parameter space. This might be due to the fact that especially events at high zenith and high impact could trigger and survive the image cleaning but not the Leakage1 cut.

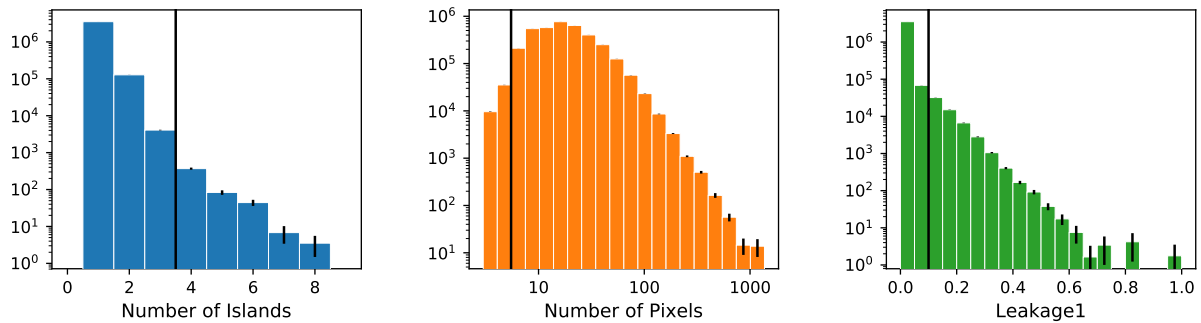


Figure 2.12.: Photon MC distribution of the number of islands (left) and pixels (center) per shower as well as the Leakage1 parameter.

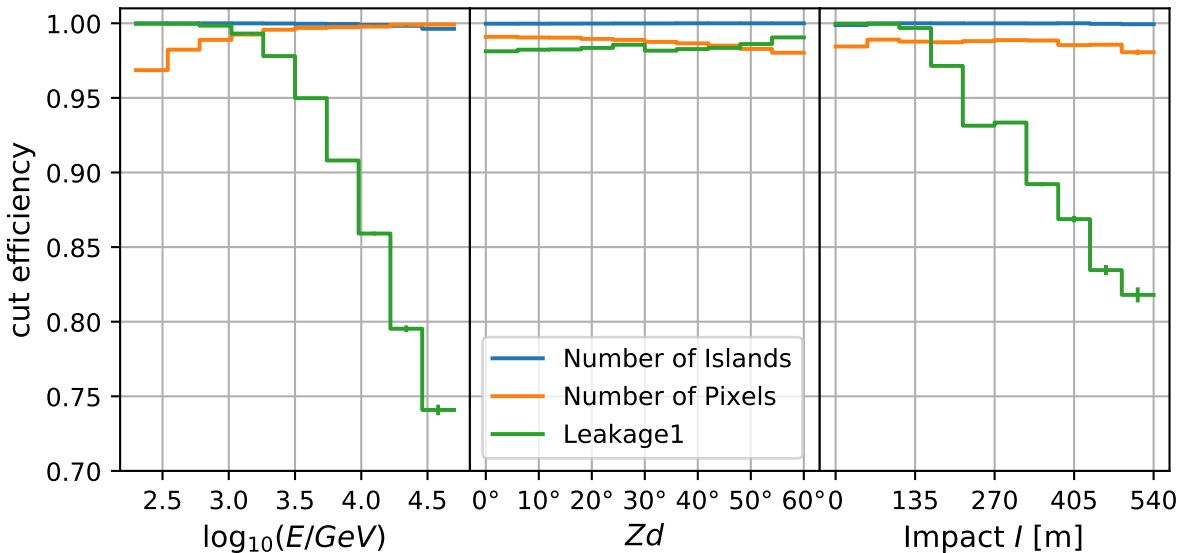


Figure 2.13.: Cut efficiency for each of the three quality cuts individually compared to the distribution of triggered and processed MC events. The left plot is binned in the true energy, the central one in the zenith distance Zd and the right one in the impact parameter of the primary photon.

2.8. Reconstruction of the Origin

To reconstruct as much information about the shower from the image as possible, a classical method introduced by [Hillas \(1985\)](#) is used. This is implemented in the module `star` of MARS-CheObs. First the total signal of the shower is defined as its size S . It can be used as a rough indicator of the energy of the primary particle. The idea is then to basically parameterise the signal distribution by its moments. Since the shower image is typically of elliptical form to first order, this results in a good parameterisation of the shower image. For this, the center of gravity (COG) of the signal distribution ($MeanX$, $MeanY$) and its covariance matrix (M_{cov}) are calculated. By solving for the eigenvectors of M_{cov} one can find the direction along which the signal distribution has the smallest and the largest spread. The variance along those two orthogonal axes define the shower's width W and length L , respectively, see also fig. 2.14. This defines the area A of the elliptical approximation and the image axis along the largest spread ("Length axis"), which is rotated by an angle δ compared to the camera's x-axis. It is then useful to extend this set of parameters also to the third momenta along the image axis. For the signal distribution this yields $M3Long$ and for the distribution of arrival times one defines the $SlopeLong$ as the slope of the arrival times when plotted against their position along the image axis. The correct sign of both variables is obtained by geometric considerations and after a conversion from mm in the camera to degrees of the corresponding observed angular distance of the sky, they are called $m3l$ and just $slope$. Both $M3Long$ and $SlopeLong$ have also an analogon defined orthogonal to the image axis which are called $M3Trans$ and $SlopeTrans$.

These parameters were then improved by [Lessard et al. \(2001\)](#), who expanded it to the so called $disp$ method. This allows the reconstruction of the direction of the primary particle, which lies on the shower axis and is shifted by a distance called $disp$ or P from the COG. [Lessard et al. \(2001\)](#) showed that P can be parameterised using W and L :

$$disp = P = \xi \left(1 - \frac{W}{L}\right) \quad (2.8)$$

The factor ξ has to be calibrated for each telescope. For FACT this was done in [Beck \(2019\)](#) by minimising the relative error on a clean subset of Crab data. It was found that a dependence on $slope$ remains: $\xi = 1.254^\circ + 0.042 \text{ deg}^2/\text{ns} \cdot slope$. The main parameters are summarised in table 2.1:

Quantity	Unit	Explanation
$Size S = \sum S_i$	p.e.	Total signal in all pixels surviving the image cleaning
$MeanX, MeanY$	mm	Mean of the signal distribution along the x/y-axis
$\delta \in [-\frac{\pi}{2}, \frac{\pi}{2})$	rad	Angle of image axis with respect to the x-axis of camera
Length L , Width W	mm	Spread of the signal distribution along and transverse to image axis
Area $A = \pi LW$	mm^2	Area of an elliptical approximation
$M3Long, M3Trans$	mm	third moment of the signal distribution along and transverse to image axis
$m3l$	mm	$M3Long$ with correct sign
$SlopeLong, SlopeTrans$	$ns \text{ mm}^{-1}$	slope of arrival time vs pixel position along and transverse to image axis
$slope$	ns/deg	$SlopeLong$ with correct sign
$dist$	mm	distance between known source position and COG of signal distribution
$\xi = 1.254^\circ + 0.042 \text{ deg}^2/\text{ns} \cdot slope$	deg	factor for determination of $disp$
$disp = P = \xi(1 - \frac{W}{L})$	deg	distance between COG and reconstructed source position along image axis

Table 2.1.: Summary of the most important parameters for the disp method

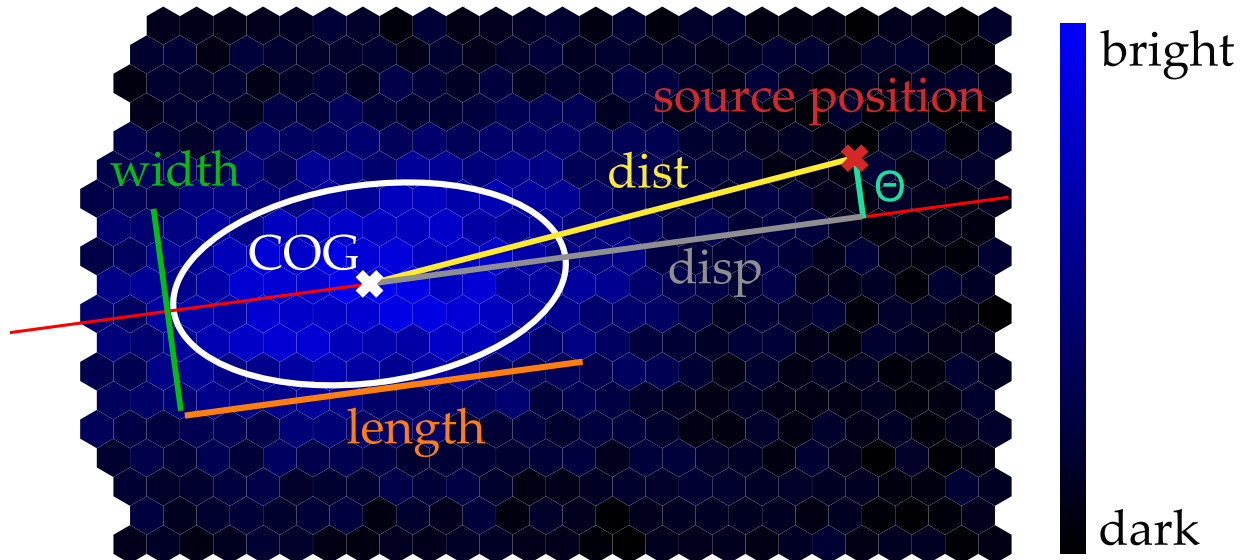


Figure 2.14.: Sketch of the Hillas parameters illustrated on a conceptual signal distribution of a shower.

2.9. Cut on Arrival Direction

After the reconstruction of the origin of the primary particle of a shower it is natural to limit the emission of a source to a certain solid angle. Since blazars as extragalactic sources and the Crab nebula can be assumed to be point-like sources with FACT's angular resolution of about 0.1° , a simple circular region around the known source position is used to cut on the arrival direction. Its radius of 0.028° is found by maximising the relative error on one winter of Crab data, see [Beck \(2019\)](#). The six circles in fig. 2.3 are drawn to scale.

This cut on the arrival direction has also the advantage to remove much more diffuse background showers which are uniformly distributed in solid angle compared to the photons from a point source following a typically Gaussian point-spread-function (PSF), which peaks around the source position. Nicely, this yields already a first step in the photon-hadron separation, which is subject of the next chapter.

The distribution of the reconstructed values of Θ^2 is shown in fig. 2.15, where the black line indicates the value above which events are excluded. Since this distribution is based only on photon events, ideally no event should be lost by the cut. However, the PSF follows a Gaussian since the reconstruction of the particles origin does not work perfectly. Especially for small images this induces a tail towards higher Θ^2 and events get lost. Nevertheless, this effect has to be seen in the context of the existence of the hadronic background, which has a flux about a factor of 1000 higher. The given cut is then optimised to yield the best significance for a Crab-like point source *with* this additional background.

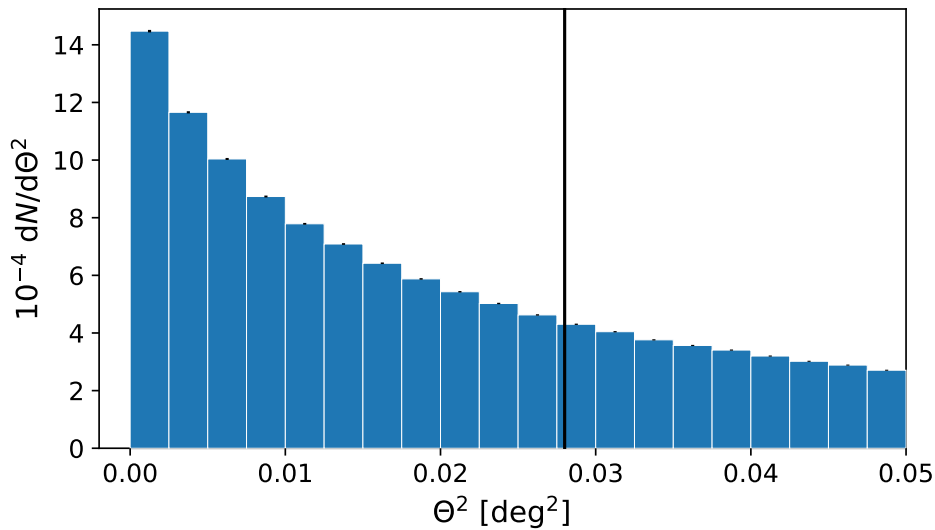


Figure 2.15.: Θ^2 distribution of the MCs consisting only of photons after applying the quality cuts described in section 2.7. The black line indicates the value above which events are excluded.

In fig. 2.16 the cut efficiencies of the Θ^2 -cut binned in energy, Zd and impact parameter are shown. It rejects in total about 70 % of the events, which is a significant amount of the data. The shape of the energy histogram fits to the expectation that low energetic events produce smaller events, whose arrival directions are harder to reconstruct and thereby the efficiency decreases. For higher energies a similar behaviour occurs, since showers become too large and their reconstruction suffers from leakage. For high Zd the efficiency decreases as well, which is due to the fainter of showers at high Zd . The extreme decrease of the cut efficiency at high values of the impact parameter can be understood by the fact these showers are more tilted and suffer from leakage similarly to high energies.

During the optimisation of the cut value a broad minimum region of 0.03° was found ([Beck 2019](#)) and one could think about increasing the cut value within this range to maximise the Θ^2 -cut efficiency for photons only.

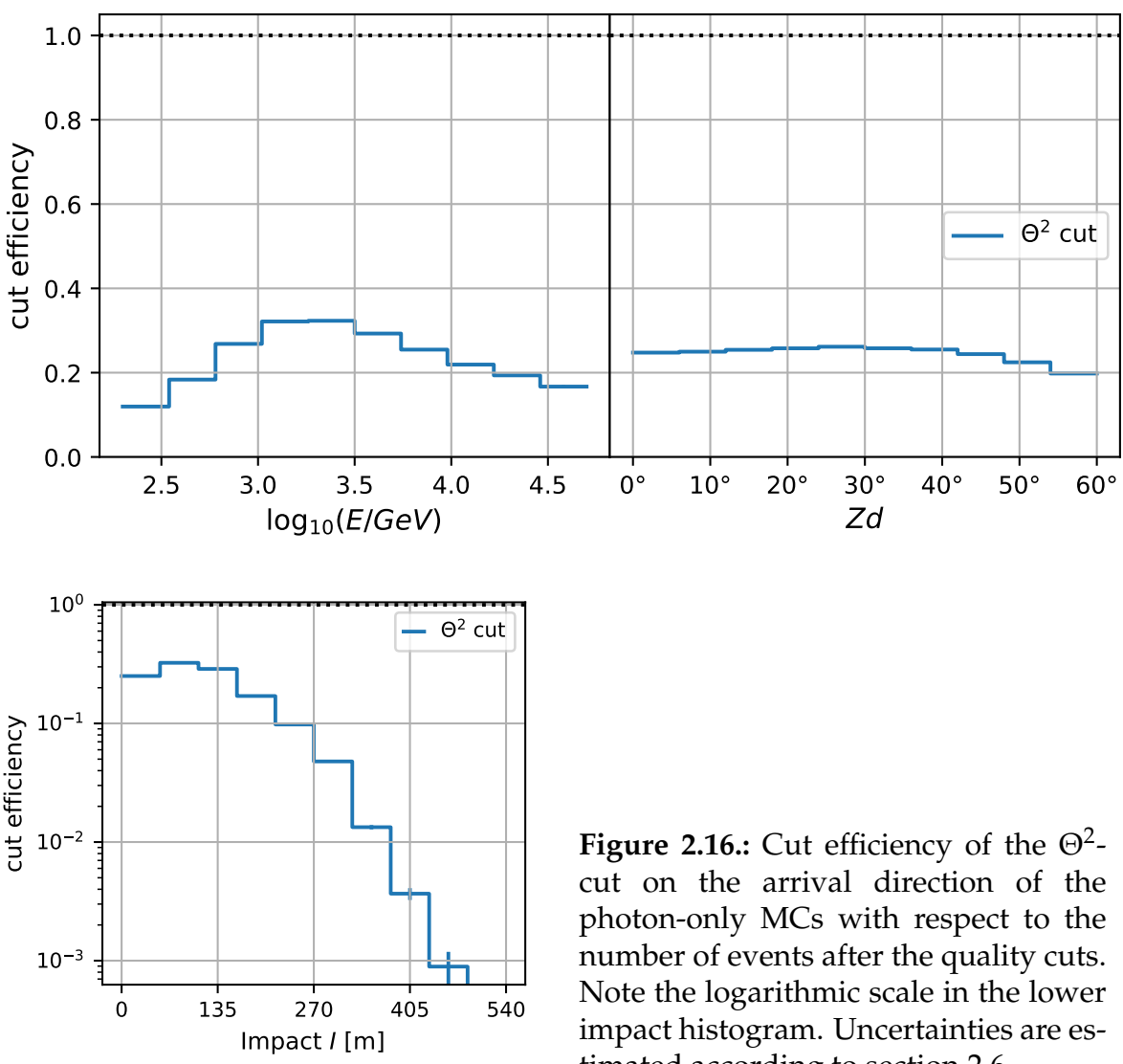


Figure 2.16.: Cut efficiency of the Θ^2 -cut on the arrival direction of the photon-only MCs with respect to the number of events after the quality cuts. Note the logarithmic scale in the lower impact histogram. Uncertainties are estimated according to section 2.6.

2.10. Gamma-Hadron-Separation

When comparing the flux of charged particles in the VHE region to the photon flux of a typical gamma-ray emitter like the Crab nebula, this background dominates the signal by about three orders of magnitude (De Angelis and Pimenta 2015). This motivates a dedicated separation mechanism to distinguish between photons and hadrons. One common method to do this is using machine learning methods like neural networks, which can be trained on dedicated MCs. However the FACT data analysis chain uses simpler approach based on the fact that photon induced electromagnetic showers are more dense and compact than hadronic ones. Defining their density as the ratio of the total Cherenkov-light intensity in the camera given by the size S over the area A of the image approximated by an ellipse, a higher density is expected for photon images. This motivates a cut in the size-area plane. A systematic investigation on the best functional shape in Beck (2019) resulted in the two cuts plotted in fig. 2.17.

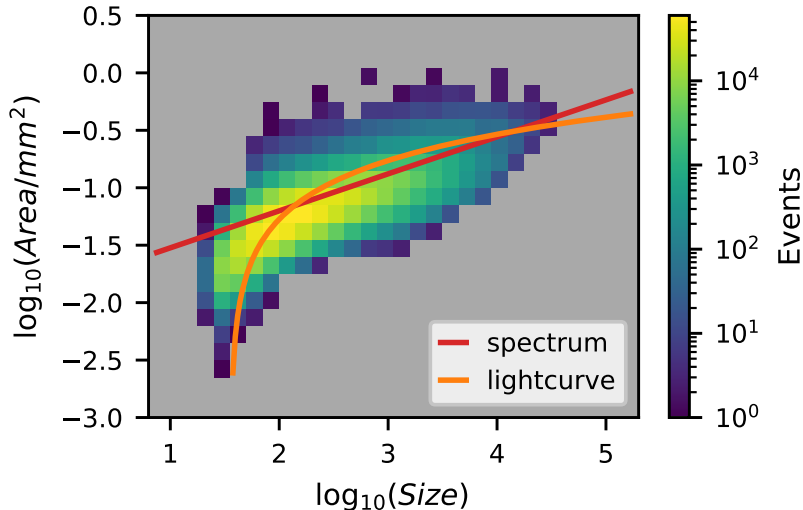


Figure 2.17.: The size-area distribution of the showers of the photon MCs after the Θ^2 -cut with the two types of Size-Area-cuts.

For both curves the relative error on Crab data is minimised, which corresponds basically to maximising its significance. However, this is done for the complete data set in case of the further goal to produce an integral light curve, while a binwise optimisation was used to obtain the the best cut in case of the calculation of a differential energy spectrum. This analysis yields a linear cut (in the log-log plot) for the spectrum, since the size can be correlated to the energy of the primary particle and for the spectrum it is important to obtain the best gamma-hadron separation in every energy bin. This effect becomes clear, when looking at the cut efficiency in binned in energy as shown in fig. 2.18, where the spectrum cut behaves rather flat compared to the light curve cut. The latter follows a logarithmic shape in the log-log-plot of size-area, which basically

cuts away everything at low energies, where the images are small and it is hard to distinguish between initial photons and hadrons. This cutting behaviour can also be seen by comparing the cuts to the underlying 2D-histogram of the MCs. However, it is important to keep two things in mind: First, some showers are missing for low Zd and high impact parameters and also for higher energies, which would probably also extend the distribution up to even higher sizes. Second, the cuts were optimised on a sample consisting of three orders of magnitude more hadronic showers, than the ones from photons shown in fig. 2.17. Both distributions overlap, which causes the cut to reject still a significant fraction of the gamma-ray induced showers.

The two plots in the center and on the right of fig. 2.18 show both the higher efficiency of the spectrum cut expected from its design. The rising behaviour with the Zd indicates that the showers which survive the Θ^2 -cut become less attenuated by the atmosphere than they shrink in area due to the geometric effect of a larger distance. For the impact parameter a rise towards larger shower distances from the telescope can be observed for the spectrum cut, which is optimised to be very efficient at high energies. Since events of large impact correspond to those with high energies, the spectrum cut is especially efficient for high impact parameters. In contrast to this, the fitted parameters of the light curve cut are dominated by the huge majority of low energetic showers with a smaller impact parameter, which leads to the cut having a low efficiency at high impacts. Note that the huge uncertainties on the efficiency arise due to the low number of events and the one-sided uncertainty for the extreme values of a efficiency of 0 and 1 (see section 2.6).

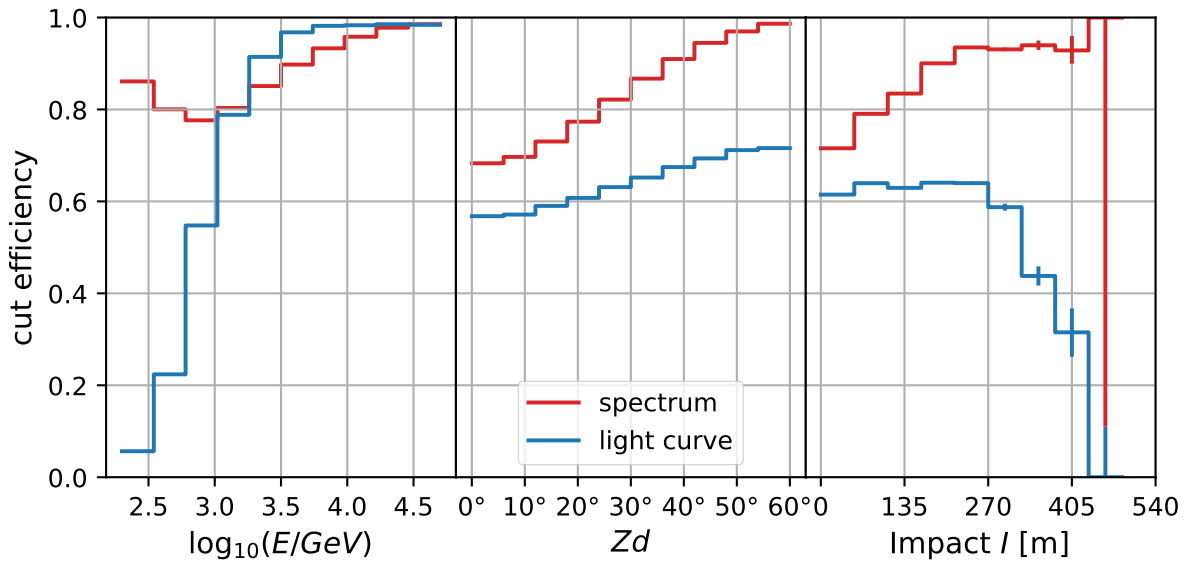


Figure 2.18.: MC efficiency of the two versions of the size-area-cut optimised for the calculation of spectra and lightcurves compared to the events surviving the Θ^2 -cut. Note that the huge uncertainties on the efficiency arise due to the low number of events and the one-sided uncertainty for the extreme values of a efficiency of 0 and 1 (see section 2.6).

2.11. Performance of Complete Analysis

The behaviour of all discussed cuts used in the analysis of FACT is summarised in form of the histograms in energy, zenith distance and the impact parameter in fig. 2.19 and fig. 2.20. Showing also the histograms offers the advantage to keep in mind the total number of events, since efficiencies alone could easily appear misleading without the underlying number density distribution.

The first two plots show especially the effect of the energy threshold of the telescope (grey area), the effect of the angular resolution (orange area) and the difference between the spectrum and light-curve cut at low energies (green area). The first two effects are also dominant in the Zd -histograms. Additionally, the histograms in fig. 2.20 show that the reconstruction and background suppression cut away all events above impact values higher than about 450 m, which justifies the chosen parameter space in the context of the current analysis.

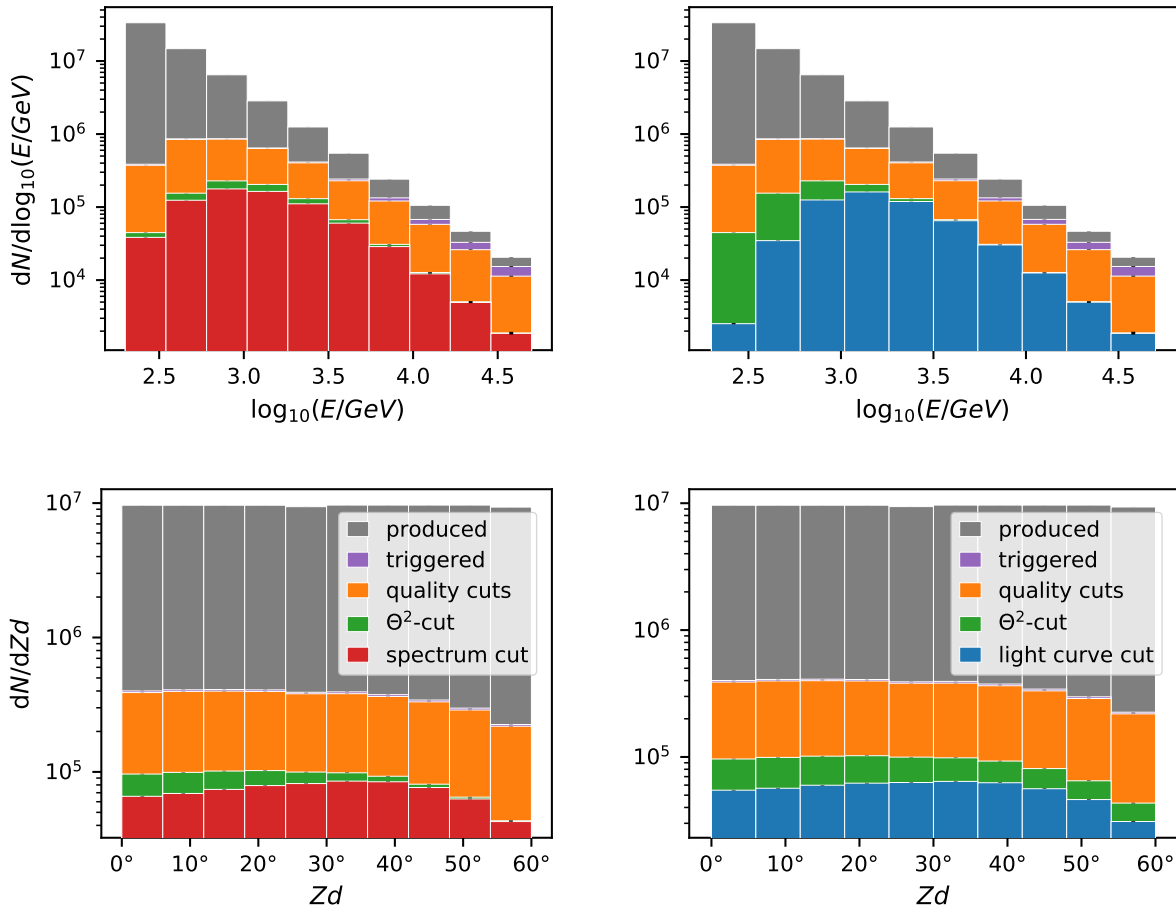


Figure 2.19.: Histograms of the gamma-ray-only MCs from the initially produced showers and after the processing from triggering to image cleaning (*triggered*), the quality cuts from section 2.7 (*quality cuts*), the cut on the arrival direction from section 2.9 (Θ^2 -*cut*) and the size-area cut for spectra (left) and light curves (right) from section 2.10.

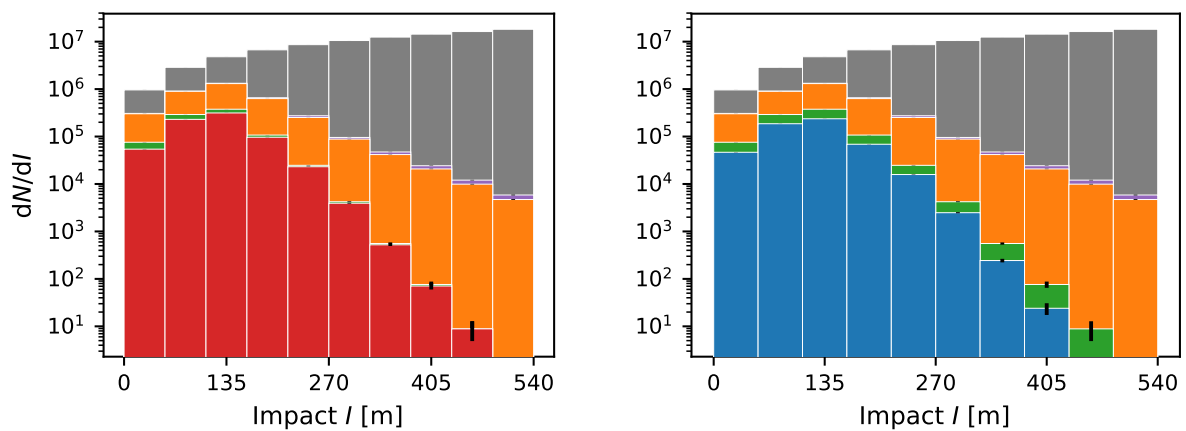


Figure 2.20.: Histograms of the gamma-ray-only MCs from the initially produced showers and after the processing from triggering to image cleaning (*triggered*), the quality cuts from section 2.7 (*quality cuts*), the cut on the arrival direction from section 2.9 (Θ^2 -*cut*) and the size-area cut for spectra (left) and light curves (right) from section 2.10. Colours are the same as in fig. 2.19.

3

PIC Simulations of Magnetic Reconnection

3.1. Magnetohydrodynamics

In many highly energetic environments the mean energy of the individual electrons and nuclei is much higher than the binding energies of the atoms and matter exists in form of a plasma. Using basic considerations from electromagnetism combined with hydrodynamic fluid theory a theory can be built to describe the phenomena of plasma. It is called magnetohydrodynamics (MHD). Assuming that the collisions are strong and thus the heat flow in the plasma is small, this yields *ideal* MHD. By further approximating Ohm's law relating the current density \mathbf{J} in a linear way and introducing the resistivity η , ideal resistive MHD emerges.

$$\eta \mathbf{J} = \mathbf{E} + \frac{1}{c} \mathbf{u} \times \mathbf{B} \quad (3.1)$$

This can be summarised in the following two sets of equations (eqs. (3.2) to (3.4) and eqs. (3.5) to (3.7)) coupled by the Lorentz force and Faraday's law ([Kulsrud 2005, ch. 3](#)):

$$\text{Continuity eq.} \quad \frac{\partial \rho}{\partial t} + \nabla \cdot (\rho \mathbf{u}) = 0 \quad (3.2)$$

$$\text{Momentum eq.} \quad \rho \left(\frac{\partial}{\partial t} + \mathbf{u} \cdot \nabla \right) \mathbf{u} = \frac{1}{c} \mathbf{J} \times \mathbf{B} - \nabla p \quad (3.3)$$

$$\text{Adiabatic Energy eq.} \quad \frac{d}{dt} \left(\frac{p}{\rho^\gamma} \right) = 0 \quad (3.4)$$

$$\text{Ampere's law} \quad \mathbf{J} = \frac{c}{4\pi} \nabla \times \mathbf{B} \quad (3.5)$$

$$\text{Faraday's law} \quad \frac{\partial}{\partial t} \mathbf{B} = \nabla \times (\mathbf{u} \times \mathbf{B}) + \frac{\eta c}{4\pi} \nabla^2 \mathbf{B} \quad (3.6)$$

$$\text{Divergence constraint} \quad \nabla \cdot \mathbf{B} = 0 \quad (3.7)$$

Equation (3.2) describes the conservation of mass, given by the change of the density ρ with time and the divergence of the flux $\rho \mathbf{u}$ with the velocity \mathbf{u} . Similarly, eq. (3.3) contains the temporal evolution of the flux or momentum of the plasma including con-

vection, Lorentz force and a gradient of the pressure p . Other force densities could also be added here. Interestingly, the Lorentz term can be divided into two terms yielding to the effects of magnetic tension and magnetic pressure (Kulsrud 2005, ch. 4.1):

$$\frac{1}{c} \mathbf{J} \times \mathbf{B} = \underbrace{\frac{(\mathbf{B} \cdot \nabla) \mathbf{B}}{4\pi}}_{\text{tension}} - \underbrace{\nabla \frac{B^2}{8\pi}}_{\text{pressure}} = \frac{B^2 \gamma}{4\pi} - \nabla \perp \frac{B^2}{8\pi} \quad (3.8)$$

where $\gamma = \mathbf{b} \cdot \mathbf{b} = -\frac{R}{B}$ with $\mathbf{B} = B\mathbf{b}$ and R is the radius of curvature. This can be interpreted as in fig. 3.1, where on the left curved magnetic field lines are shown and the magnetic tension is indicated by the arrow. In the same way, the magnetic pressure scales with the gradient of the energy density of the magnetic field, $U_B = \frac{B^2}{8\pi}$, perpendicular to its direction. From the adiabatic energy equation, eq. (3.4), it can be seen that the entropy is a constant in time. Equations (3.5) to (3.7) are basically Maxwell's equations with Ohm's law with the resistivity η . In the limit $\eta = 0$ one obtains ideal MHD.

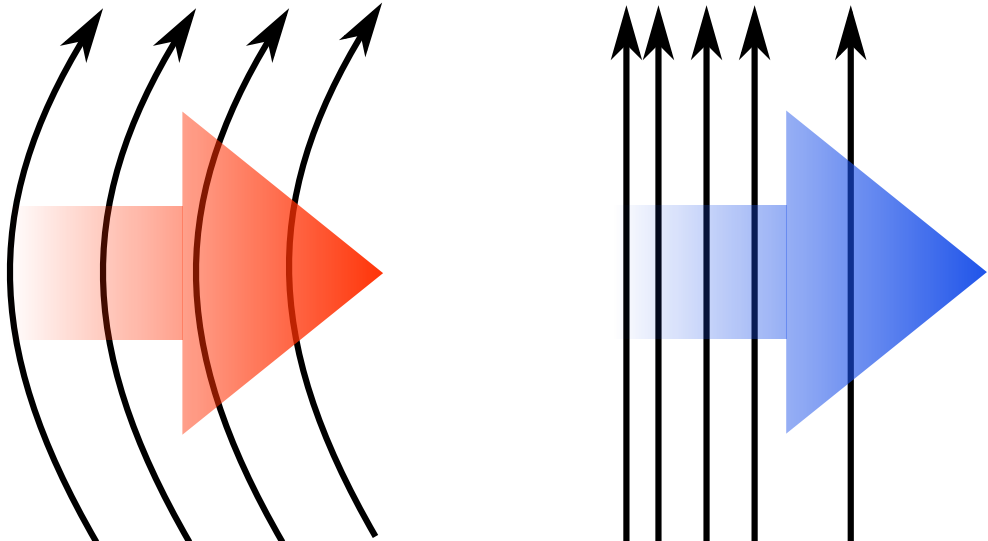


Figure 3.1.: Illustration of magnetic tension for curved field lines (left) and magnetic pressure with an orthogonal gradient in the field line density (right). In both cases the magnetic force points towards the right.

3.2. Flux Freezing

One particularly important consequence of Faraday's law (eq. (3.6)) is that in the case of no resistivity the number of magnetic field lines through a moving fluid element does not change. Thus, the field lines become embedded into the plasma which transports it. The topology is conserved. This is called flux freezing as the magnetic field *freezes* into the plasma. Mathematically this can be understood by looking at the derivative of the

magnetic flux Φ with respect to time:

$$\frac{d\Phi}{dt} = \frac{d}{dt} \int_{S(t)} \mathbf{B}(\mathbf{x}, t) d\mathbf{A} = \int_S \frac{\partial \mathbf{B}}{\partial t} d\mathbf{A} + \int_{\partial S} \mathbf{B} d\mathbf{A} \quad (3.9)$$

The first term is the change of the magnetic field itself, which can be transformed using eq. (3.6) and Stoke's theorem:

$$\int_S \frac{\partial \mathbf{B}}{\partial t} d\mathbf{A} = \int_S d\mathbf{A} \cdot \left(\nabla \times (\mathbf{u} \times \mathbf{B}) + \frac{\eta c}{4\pi} \nabla^2 \mathbf{B} \right) \quad (3.10)$$

$$= \int_S d\mathbf{A} \cdot [\nabla \times (\mathbf{u} \times \mathbf{B} - \eta c \mathbf{J})] \quad (3.11)$$

$$= \int_L d\mathbf{l} \cdot (\mathbf{u} \times \mathbf{B} - \eta c \mathbf{J}) \quad (3.12)$$

The evaluation of the second term yields exactly the striped area in fig. 3.2:

$$\int_{\partial S} \mathbf{B} \cdot d\mathbf{A} = \int_L (\mathbf{u} \times d\mathbf{l}) \cdot \mathbf{B} = - \int_L d\mathbf{l} \cdot (\mathbf{u} \times \mathbf{B}) \quad (3.13)$$

In total the change of the magnetic flux is thus given by the remaining resistive term:

$$\frac{d\Phi}{dt} = - \int_L d\mathbf{l} \cdot \eta c \mathbf{J} \quad (3.14)$$

This means that for vanishing resistivity $\eta = 0$ the flux is frozen into the plasma. For $\eta \neq 0$ the magnetic field line can slip away from the plasma's volume element in the time t a distance of:

$$l = \sqrt{\frac{\eta c t}{4\pi}} \quad (3.15)$$

As long as this distance is small compared to the length scale of interest, the flux freezing approximation works well.

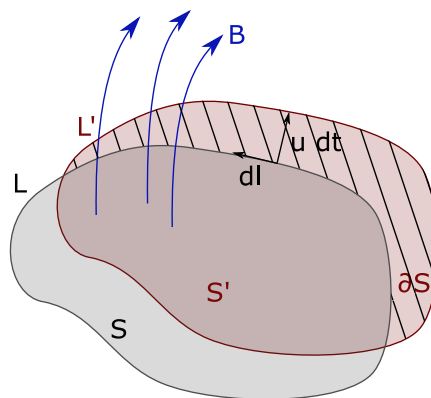


Figure 3.2.: Sketch of the calculation of the second term: It is the integral of the magnetic field over the striped area.

3.3. Magnetic Reconnection

Magnetic reconnection is a phenomenon that occurs if now the magnetic field possesses strong gradients. There the approximation of ideal MHD breaks down. A simple realisation of this is given in fig. 3.3: two antiparallel field lines approach each other. Then the magnetic field can slip away for a significant distance from the plasma's volume element and the flux is no longer frozen. In the transition zone called *current layer*, resistivity starts to play a significant role and the topology changes: the field lines reconnect.

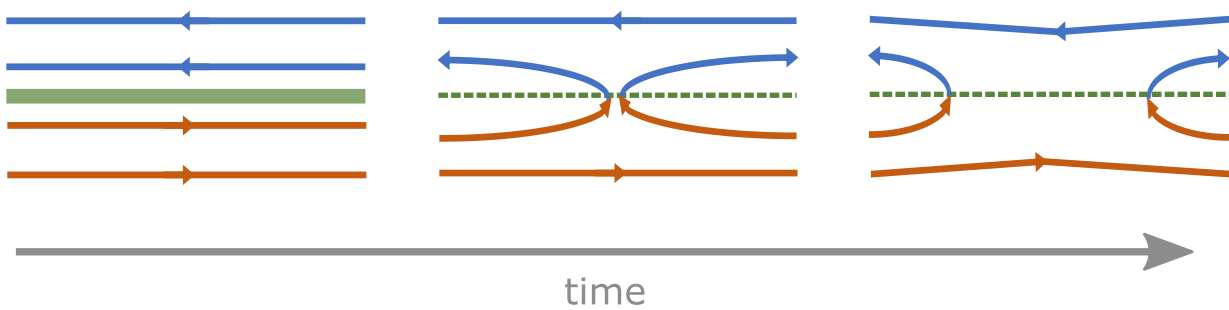


Figure 3.3.: Illustration of magnetic reconnection with temporal evolution from left to right.

One consequence of the occurrence of resistive effects in the current layer is the transformation of magnetic energy from the field to thermal energy of single particles by dissipation. This mechanism heats up the plasma and can accelerate particles to high energies.

Once the field lines have reconnected, their strong curvature produces a magnetic tension force, which pulls the reconnected field lines outwards along the current layer. In combination with the magnetic pressure gradient, plasma can be accelerated up to the Alfvén velocity $v_A = \frac{B}{\sqrt{4\pi\rho}}$ with the mass density ρ . The horizontal outflow of plasma is then compensated by a vertical inflow, compare also fig. 3.4 ([Giannios 2013](#)).

At the beginning of the reconnection theory it has been dominated by steady-state models like the ones by [Sweet \(1958\)](#) and [Parker \(1957\)](#) or [Petschek \(1964\)](#). As also visible in fig. 3.4, these allow a basic understanding of the average behaviour of the system like for example inflow and outflow speeds as well as the reconnection rate r ([Giannios 2013](#)). For the Sweet-Parker geometry it is given by $r = \frac{\delta}{L}$, where δ is given by the scale, at which resistivity becomes important (thickness of the current layer) and L is the length of the system (length of the current layer). As astrophysical plasmas are usually huge, this rate is typically very small and reconnection is not really efficient. To speed it up, Petschek added shocks to the set up, which limits the size of the reconnection region. However, this model is hard to reproduce by simulations and it is still not completely accepted ([Fitzpatrick 2014](#)). Furthermore, astrophysical plasmas, especially in blazar's jets, are expected to be highly relativistic. Then the magnetic energy in the reconnection region is much higher than the total enthalpy $w = \gamma + \frac{P}{mn c^2}$ of

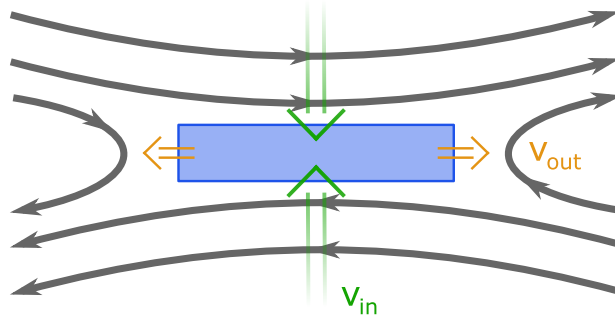


Figure 3.4.: Sketch of Sweet-Parker-reconnection: The reconnection of the grey magnetic field lines powers the horizontal plasma outflow (orange arrows). Assuming a steady state and and using the MHD equations, the vertical plasma inflow speed (green arrows) can be connected to the outflow speed from the considered blue volume.

each particle, where P is the pressure of the plasma. Nevertheless, Lyubarski showed in [Lyubarsky \(2005\)](#) that the reconnection rate for Sweet-Parker reconnection holds still in the relativistic case. It is thus still slow. Of great importance is therefore another detail: [Comisso and Asenjo \(2014\)](#) showed that aside of resistivity, also thermal kinetic effects can drive relativistic reconnection and even dominate it. Then the important scale of δ is the skin depth given by the speed of light over the plasma frequency $\omega_p = \sqrt{\frac{4\pi ne^2}{w}}$. But even if kinetic reconnection dominates, the length of astrophysical systems still tends to be bigger than δ and the reconnection stays slow.

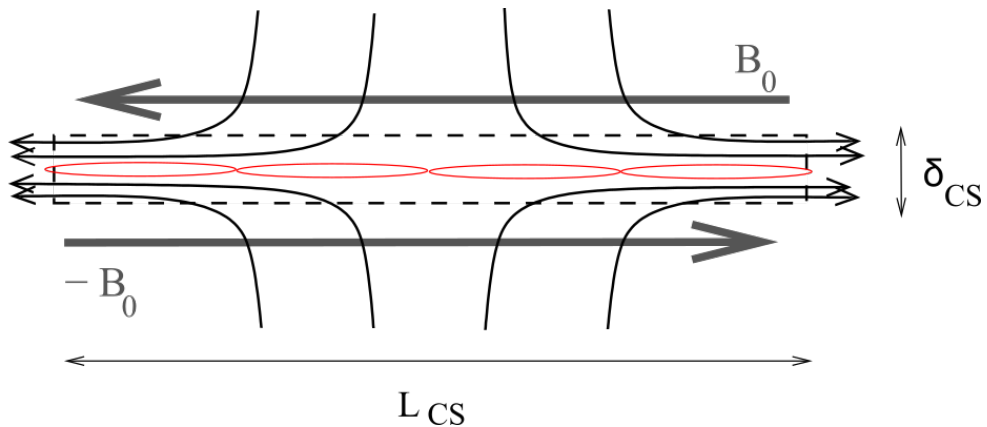


Figure 3.5.: Illustration of the formation of a chain of plasmoids due to the plasmoid instability in a constellation with two antiparallel magnetic fields and a perpendicular inflow towards the center. ([Loureiro, Schekochihin, and Cowley 2007](#))

The solution for fast reconnection is based on fragmentation. The so called plasmoid instability creates magnetic islands in the current layer, which divides it into several smaller current layers. Each of those could be seen as a new current layer, which is in-

stable to the plasmoid instability and thereby subdivided into even smaller ones. This yields a self-similar picture of plasmoids held together by magnetic tension and inter-plasmoid current layers down to a certain scale, at which the length of the layer becomes so small that stable Sweet-Parker reconnection can occur ([Uzdensky, Loureiro, and Schekochihin 2010](#)). A sketch of this is shown in fig. 3.5, where the formation of a plasmoid chain in red is illustrated.

3.4. PIC Simulations in Two and Three Dimensions

To really develop the properties of relativistic magnetic reconnection based on first principles, fully-kinetic particle-in-cell (PIC) simulations have to be performed. The concept is explained in fig. 3.6. It is based on the alternating solving of the equations of motion of so called macro-particles within a cell and the solving of Maxwell's equations on the cell's grid points. Macro-particles are in this context a collection of charged particles, which are moved using the Lorentz-force based on the current field values. The emerging currents and the new charge density is then interpolated to the grid to solve Maxwell's equations for the new field configuration. This is then interpolated to the macro-particle's positions to calculate the Lorentz-force for the next step in time. This approach is then capable of treating all effects of collisionless plasmas, even the acceleration of particles up to high energies ([Kagan et al. 2015](#)).

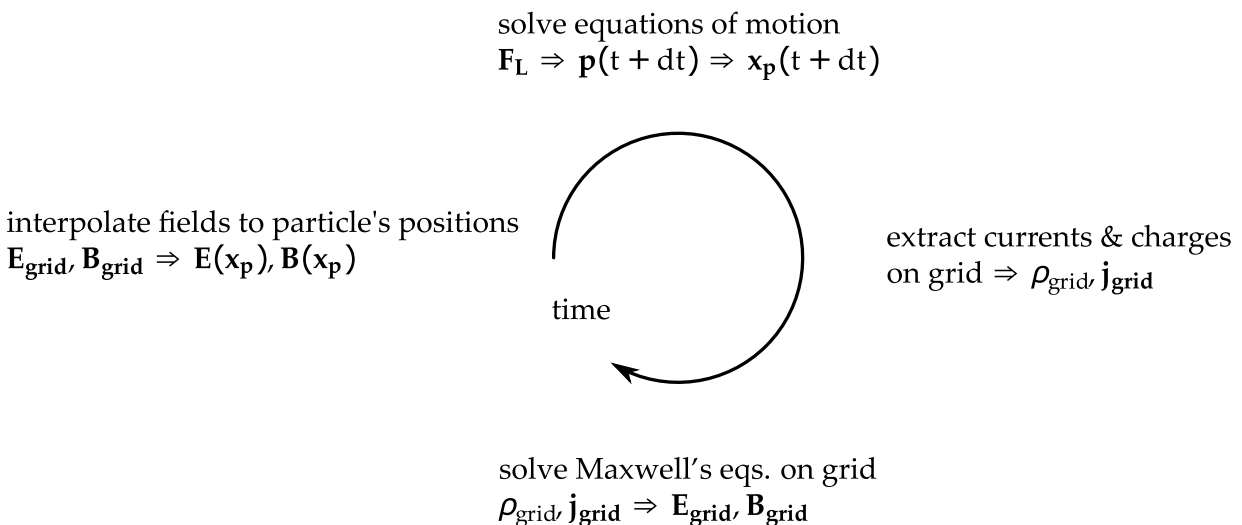


Figure 3.6.: Concept of PIC simulations: Starting on top, the new momentum and position of the macro-particles is calculated from the Lorentz-force. This result is used to extract the new currents and charges on the grid points of a cell. With this, the electric and magnetic fields can be obtained by solving Maxwell's equations on this grid. The fields can then be interpolated to the particles positions to determine the new Lorentz-force for the next step.

In order to study magnetic reconnection in real environments one would clearly expect the effects of a 3D simulation compared to just 2D or 2.5D (including a guide field perpendicular to the 2D plane) to be inevitable. However, Sironi and Spitkovsky analysed the results of PIC simulations of relativistic electron-positron plasmas, which show a very similar behaviour in 2D as well as 3D ([Sironi and Spitkovsky 2014](#)). In both cases a series of magnetic islands is visible in the x-y-plane paralleling the late-time evolution of 2D simulations. An example of such a 3D simulation is shown in fig. 3.7. Also the absence of a guide field does not affect this behaviour. This was also confirmed by more recent and systematic studies in [Werner et al. \(2017\)](#). With this in mind, the results of computationally much faster 2D simulations can be used as well.

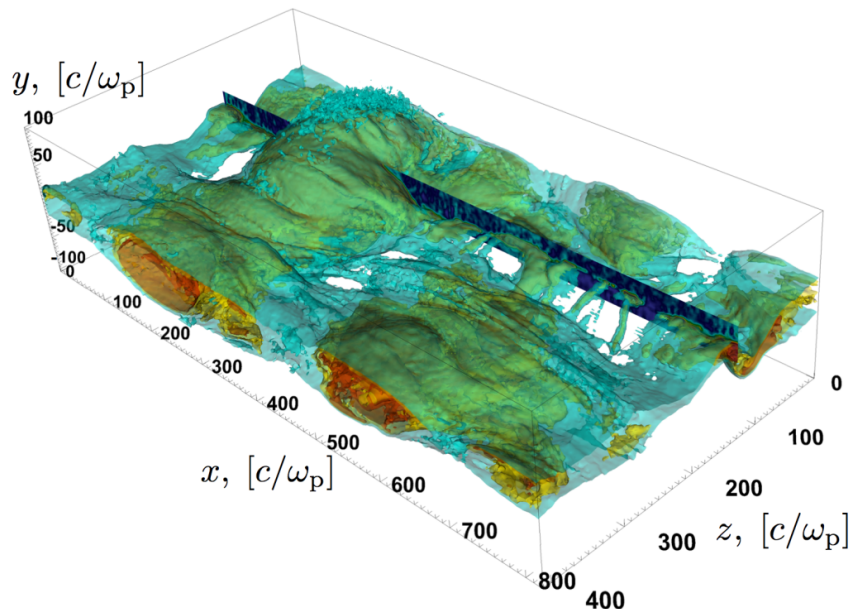


Figure 3.7.: 3D PIC simulation from [Sironi and Spitkovsky \(2014\)](#) showing a very similar structure with tubes of overdensity in red as well as transparent underdensities.

3.5. Evolution of a Stationary State with Plasmoids

In very detailed studies, [Sironi, Giannios, and Petropoulou \(2016\)](#) and [Petropoulou et al. \(2018\)](#) performed 2D PIC-simulations of relativistic magnetic reconnection in electron-positron pair-plasmas and investigated the statistical properties of the plasmoid chain and the several processes that can occur. As expected from previous studies, a steady state independent of the initial conditions evolves, which is mainly due to the open boundary conditions (i.e. whatever leaves the volume is gone instead of being reflected) and the large time scale. This steady state possesses a chain of plasmoids behaving like individual particles, whose statistical properties are then parameterised to replace the PIC simulations by a much faster but also simpler Monte Carlo approach.

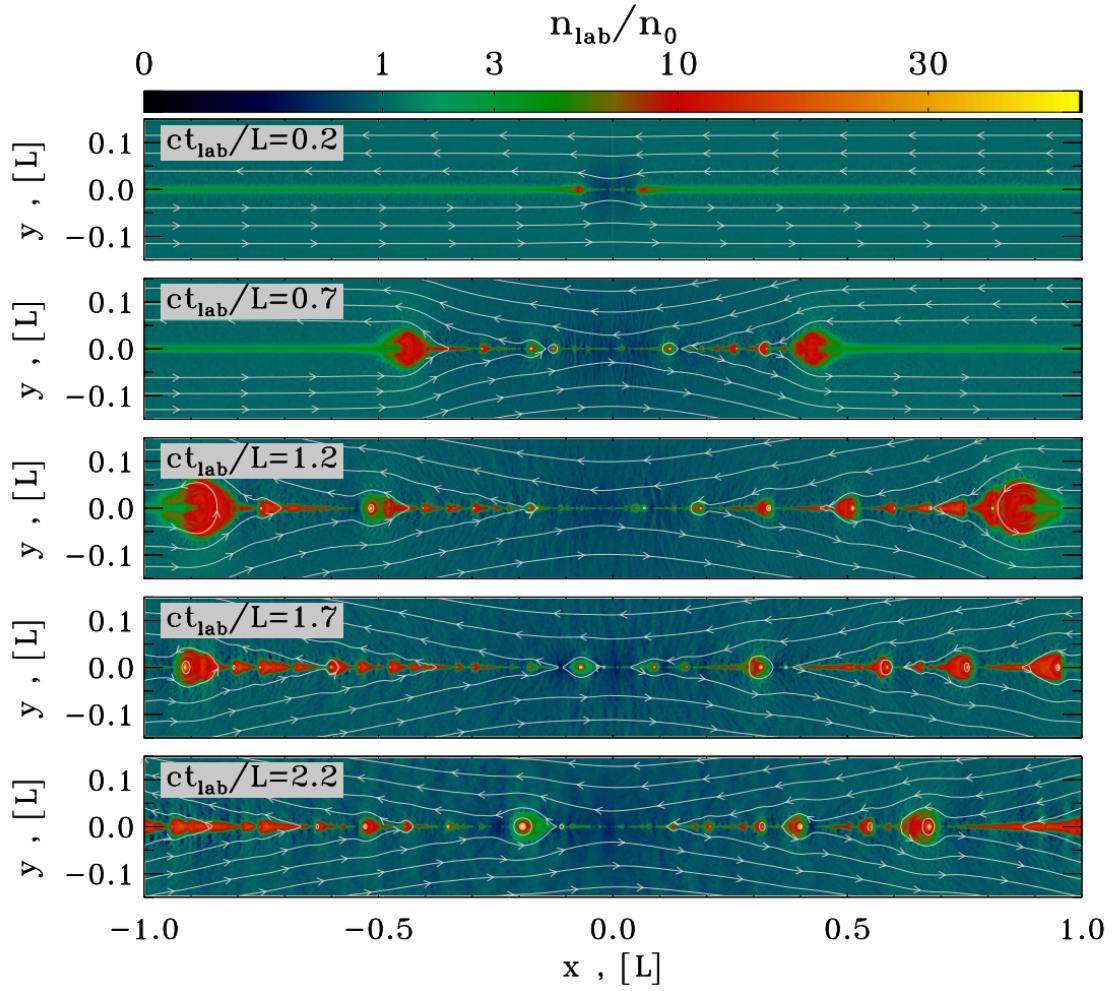


Figure 3.8.: Temporal evolution of the number density of the plasma. From PIC simulation of Sironi, Giannios, and Petropoulou (2016).

The general setup of the simulations is as follows: Everything starts from an equilibrium based on a Harris sheet with an additional hot plasma component to compensate the magnetic pressure. A Harris sheet is defined by a magnetic field of the form: $B_{\text{ini}} = B_0 \tanh(\frac{2\pi}{\Delta} y) \hat{x}$, with the width Δ which is chosen large enough to prevent spontaneous primary reconnection. To trigger the reconnection, in a central X-point the density of the additional hot plasma is lowered, such that the current layer is significantly compressed and reconnection starts, see fig. 3.8. By this, two primary fronts of magnetic reconnection evolve from the centre outwards along the y-axis, accelerated by magnetic tension. In the region between them the plasmoid instability is then fragmenting the new secondary layer into further sub-layers divided by plasmoids. To keep this process alive, fresh plasma for the inflow has to be injected. As this setup of studying secondary magnetic reconnection is designed to be independent of the initial conditions, also for the injection two injectors moving at the speed of light are used. Together with an expanding simulation box, this ensures always fresh plasma without causal contact to the

reconnection process. Then the system is evolved without any guide field for several light crossing times L/c , where L is the length of the system. As the primary fronts move at about Alfvén-speed which approaches the speed of light, they leave the layer after about one light crossing time. Because they carry the information about the initial conditions, afterwards a steady state of plasmoid-dominated reconnection is observed. The properties of the reconnecting layer then depend only on the flow conditions far from the current sheet. In this setup this is only the magnetisation σ of the layer, which is given by the ratio of magnetic to kinetic energy ([Kagan et al. 2015](#)):

$$\sigma = \frac{B^2}{4\pi(\gamma(\rho_e + \rho_p)c^2 + P)} \approx \frac{B_0^2}{4\pi m_p n_0 c^2} \quad (3.16)$$

where P is the pressure, ρ_e / ρ_p is the electron/proton rest mass density, m_p the proton mass, n the number density and the index 0 denotes the quantities far from the current layer. The approximation is based on the fact that the pressure far upstream compared to the kinetic energy of a particle and the electron compared to the proton mass density can be neglected. As relativistic reconnection is the regime of $\sigma > 1$, [Sironi, Giannios, and Petropoulou \(2016\)](#) investigated three different values of σ : 3, 10 and 50.

Description of a Plasmoid

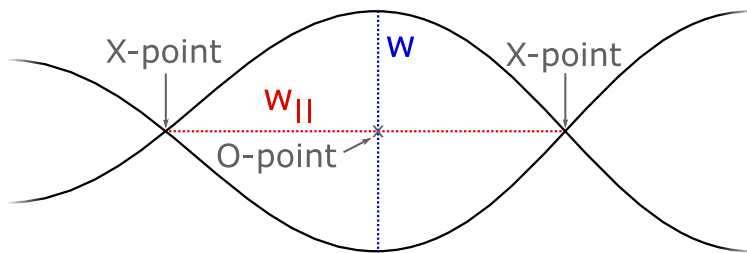


Figure 3.9.: Schematic sketch of a plasmoid

A plasmoid is defined between two X-points of the magnetic field lines (lines of constant potential). In fig. 3.9 a sketch of this is drawn. Its width w and length $w_{||}$ can be derived from this. The plasmoid's position x and velocity β are determined as the coordinates of the central O-point. In [Sironi, Giannios, and Petropoulou \(2016\)](#) (fig. 5 (a)-(c)) it was found that in their rest frame, which is moving with β , the plasmoids are quasi-spherical, i.e. the ratio of the plasmoid's width to height is 1.5, independent of the magnetisation. Thus, a plasmoids area can be approximated by an ellipse: $A = \pi w^2/4$. Furthermore, the density of a plasmoid in the rest frame and the magnetic field strength are found to be constant in time, compare fig. 5. (d)-(f) and (j)-(l) of [Sironi, Giannios, and Petropoulou \(2016\)](#).

Particle Spectrum

In [Sironi and Spitkovsky \(2014\)](#) it was found that momentum distribution of the particle from the whole reconnection layer at late times follows a power law with the slope becoming harder for higher magnetisations. Although this spectrum is likely dominated by the biggest plasmoids, it indicates that acceleration becomes more efficient for higher values of σ . It was checked that the results for 2D and 3D reconnection are very close. The PIC simulations of [Sironi, Giannios, and Petropoulou \(2016\)](#) yield similar and compatible results for the slope p : $p \sim 3$ for $\sigma = 3$, $p \sim 2$ for $\sigma = 10$ and $p \sim 1.5$ for $\sigma = 50$. This result is especially important for the injection of the particles later in section 4.11.3.

Acceleration of plasmoids

As can be seen in fig. 3.8 the magnetic field lines show up a V-type feature pointing towards the centre of the current layer. This results in an effective magnetic tension force accelerating the plasmoids to the right/left boundary of the system. This motion is shown in fig. 3.10, where the trajectories of the biggest plasmoids are plotted with a colour code showing their size. In the PIC simulations a general velocity profile of the plasmoids can be found (fig. 3.11), depending on their position x , their initial position x_0 and their radius w (σ being the magnetisation of the system):

$$\gamma\beta = \sqrt{\sigma} \tanh\left(\frac{\beta_a}{\sqrt{\sigma}} \frac{x(t) - x_0}{w(t)}\right) \quad (3.17)$$

Here β_a is a constant and can be interpreted as the rate of acceleration for small values of $(x - x_0)/w$. Figure 3.11 shows also a correlation between the size and the momentum of a plasmoid. Smaller plasmoids are in general faster (blue) than larger plasmoids (red).

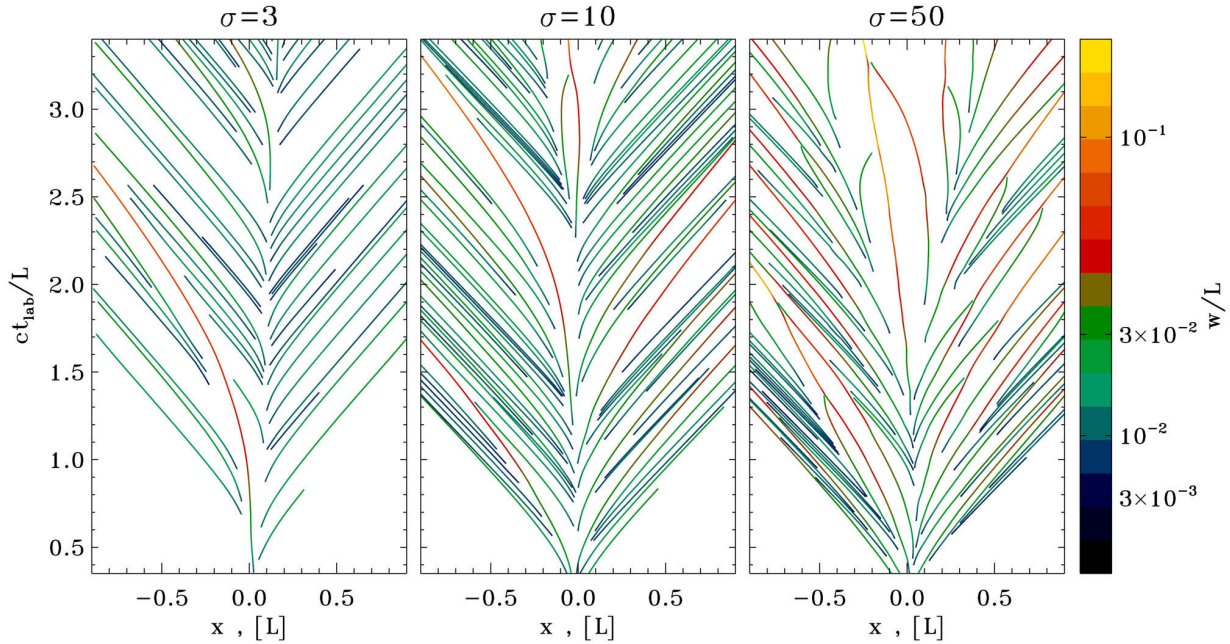


Figure 3.10.: Trajectories of the plasmoids in the PIC simulations for three different magnetisations σ . Only plasmoids with a lifetime above $0.35L/c$ are included and colours denote their momentum. (Sironi, Giannios, and Petropoulou 2016)

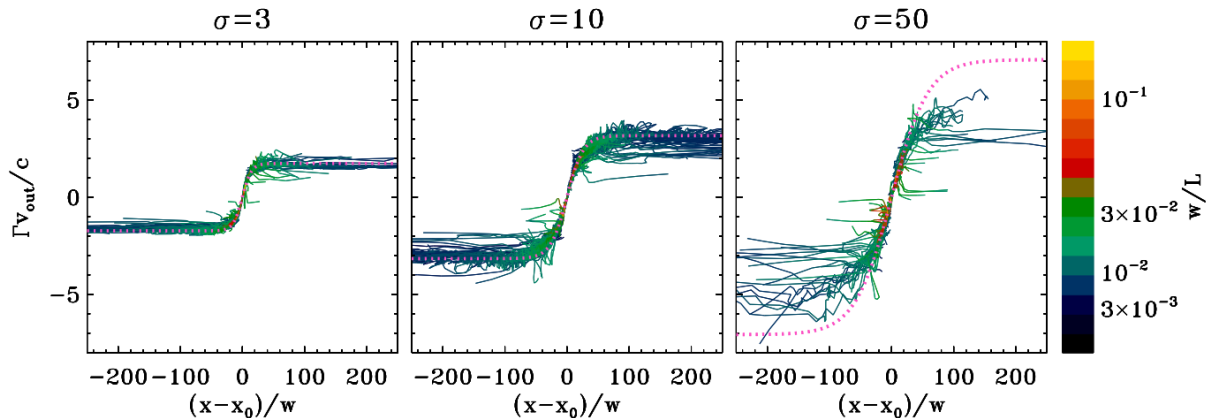


Figure 3.11.: Dependency of the plasmoid's velocity on its distance from the central reconnection point for three different magnetisations σ . A hyperbolic tangent is fit to the distribution in pink. The colour encodes the size of the plasmoids. (Sironi, Giannios, and Petropoulou 2016)

Mergers and Boundary Losses

When looking at fig. 3.10 it can also be seen that some lines suddenly end. At these points the plasmoid gets absorbed by a neighbouring bigger plasmoid. This is a frequently occurring process in the evolution of a chain. It is also visible that smaller plasmoids even get attracted in the vicinity of bigger plasmoids, until they merge. The boundary conditions used in the PIC code are open, meaning that once an plas-

moid has left the simulated scope, it is gone and does not affect the future evolution of the system.

Growth

Figures 3.8 and 3.10 indicate furthermore that plasmoids grow on their way to the edges of the system. This is due to the vertically inflowing fresh plasma and the merging of smaller and faster into slower but bigger plasmoids. [Sironi, Giannios, and Petropoulou \(2016\)](#) find that the growth rate as measured in the comoving frame of the plasmoid is constant in time:

$$\frac{dw}{cdt} = \beta_g \quad (3.18)$$

In the rest frame of the reconnection layer a Lorentz factor has to be added. This is shown in fig. 3.12 for three different magnetisations. Additionally, at a given momentum the growth stops. This can be understood by considering the correlation between speed and size: Smaller plasmoids are usually faster and can catch up with bigger and slower plasmoids. Once they arrive at a bigger plasmoid, they get simply absorbed by it. From the perspective of a slow and big plasmoid the same argument can be turned around, such that bigger plasmoids do not merge with plasmoids in front of them, but grow through the accretion of smaller plasmoids. Having a close look at fig. 3.12, dips in the growth rate of especially larger plasmoids can be observed. These originate from mergers, where the stability of the plasmoid is perturbed. Another detail from fig. 3.12 is the growth of a few plasmoids up to extremely large sizes of about a tenth of the layer's length. These plasmoids are called *monster* plasmoids and occur only rarely.

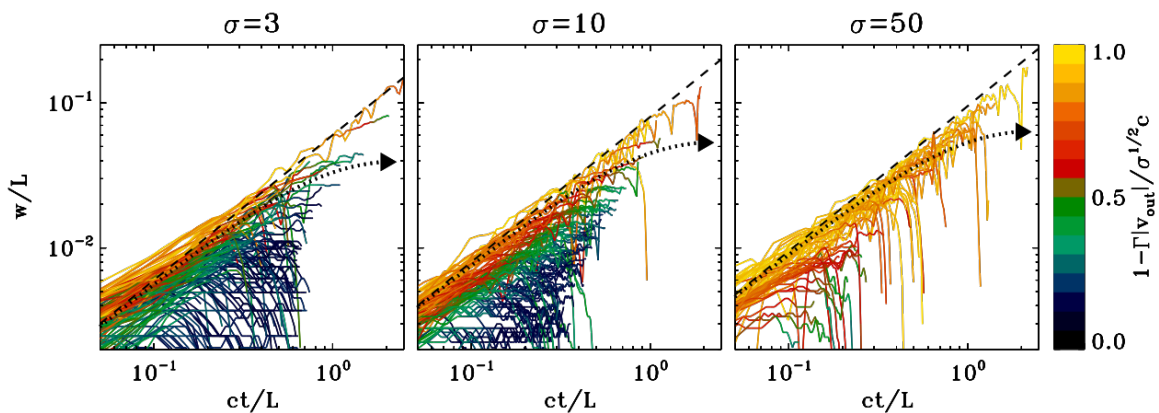


Figure 3.12.: Growth of the plasmoids in the PIC simulations for three values of the magnetisation. Colours denote the missing fraction to the maximal momentum of $\sqrt{\sigma}$. ([Sironi, Giannios, and Petropoulou 2016](#))

Birth of new Plasmoids

Due to the intrinsic property of the plasmoid instability, the fragmentation of the current layer, there are permanently new plasmoids generated. They start having a minimal size of a few skin depths and then grow. As already mentioned, the plasmoid's

momentum depends on its position and size. Assuming the same initial size for every plasmoid at birth, its initial momentum depends on the position of birth in the layer. [Petropoulou et al. \(2018\)](#) parameterised the initial momentum p_0 using an initial size of $w_{\min} = 10^{-3}L$, see also fig. 3.13:

$$\langle p_0 \rangle = 0.66\sqrt{\sigma} \tanh \frac{x_0}{l_0} \quad \text{with} \quad l_0 \approx 0.25L \frac{\sigma}{10} \quad (3.19)$$

Intuitively this would also be expected, as the bulk outflow flow increases outwards. It was furthermore found that the spread around this correlation is normally distributed with a standard deviation of about $\sigma_{p_0} = 0.3\sigma$. This also implies that in general plasmoids with positive/negative x_0 (right/left of the center) obtain a positive/negative momentum and motion happens outwards. Nevertheless, few plasmoids can also be generated with a momentum into the opposite direction. [Petropoulou et al. \(2018\)](#) investigated also the mean distance between the birth positions of two new plasmoids and found a value of $\delta x \sim 10w_{\min}$.

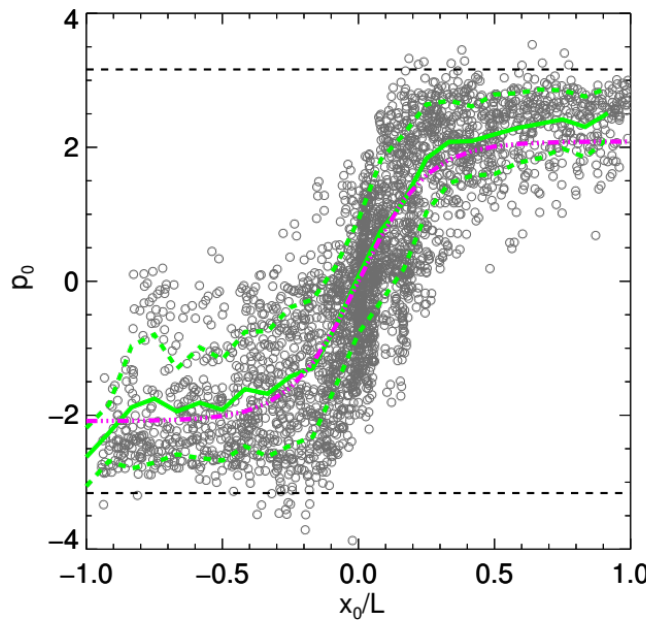


Figure 3.13.: Initial momentum of the plasmoids in the PIC simulations depending on their initial position. ([Petropoulou et al. 2018](#))

3.6. Monte Carlo Approach to Replace PIC-Simulations

Following the idea of [Petropoulou et al. \(2018\)](#), this section deals with the approach to replace the PIC simulations with a Monte Carlo code still incorporating their properties. The basic idea is to treat the plasmoids as particles and describe them by their position

and size. As explained in eq. (3.17) their momenta then follow from their positions. Together with eq. (3.18), acceleration and growth are handled on a statistical base. This approach offers three advantages: First, solving the MC equations is computationally much cheaper than the PIC-code. Secondly, this offers the possibility to study the system over much larger time scales. This is especially interesting in the context of the consequences of the plasmoids radiative evolution in the context of blazar variability in the following chapters. Finally, this approach also allows to study the roles of the individual processes like mergers, which can be easily isolated. The numerical implementation of the MC code and a discussion of the results are subject of the next two subsections.

3.6.1. Numerical Implementation

The two variables characterising a plasmoid are its position $r = x/L$ and its size $s = w/L$, both normalised to the length of the reconnection layer L . Also the time is normalised to the layer's light crossing time $\tau = ct/L$. Then, the effects of growth and acceleration described above can be summarised in the following system of coupled partial differential equations:

$$\frac{dr}{d\tau} = \beta = \frac{\hat{p}}{\sqrt{1 + \hat{p}^2}} \quad (3.20)$$

$$\frac{ds}{d\tau} = \frac{\beta_g}{\Gamma f_{\text{sup}}(\hat{p})} = \frac{\beta_g}{f_{\text{sup}}(\hat{p})\sqrt{1 + \hat{p}^2}} \quad (3.21)$$

$$(3.22)$$

where β_g is the constant growth rate. Those two equations are linked via the momentum evolution eq. (3.17):

$$\hat{p}(r(\tau), s(\tau)) = \sqrt{\sigma} \tanh\left(\frac{\beta_a}{\sqrt{\sigma}} \frac{r - r_0}{s}\right) + \hat{p}_0 \quad (3.23)$$

with r_0 and \hat{p}_0 being the initial values of r and \hat{p} and with the momentum dependent growth suppression factor:

$$f_{\text{sup}}(\hat{p}) = \frac{2}{1 - \tanh\left(\frac{\frac{|\hat{p}|}{\sqrt{\sigma}} - A}{B}\right)} \quad (3.24)$$

The dependency of f_{sup} on A , B and σ is shown in fig. 3.14. The parameter A plays the role of a threshold momentum, B determines the sharpness of the cutoff, which both also scale with the magnetisation σ . Following eq. (3.18) the growth is incorporated in the growth rate β_g . The Lorentz-factor Γ in eq. (3.21) appears because there is only a constant growth rate in the plasmoids rest frame.

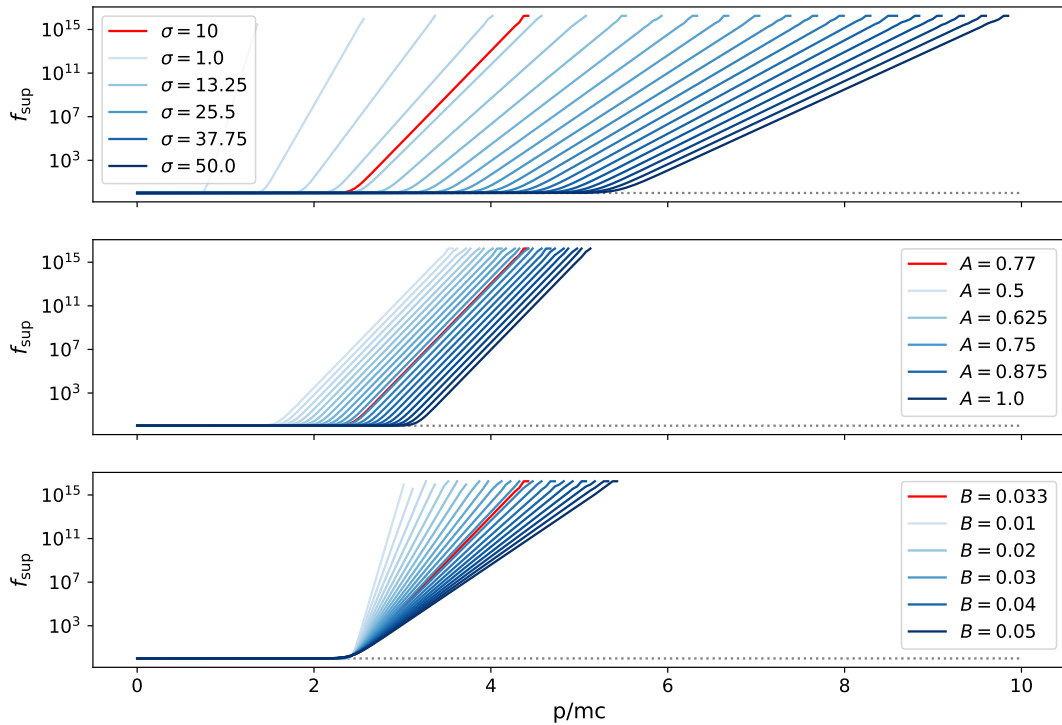


Figure 3.14.: Influence of the parameters of f_{sup} , which is used for the growth suppression.

These equations are then solved using the simple Euler method:

$$r_{i+1} = r_i + \left(\frac{dr}{dt} \right)_i dt \quad (3.25)$$

$$s_{i+1} = s_i + \left(\frac{ds}{dt} \right)_i dt \quad (3.26)$$

$$(3.27)$$

The index denotes the time step here and the derivatives are given by the eqs. (3.20) and (3.21). This could be certainly improved using a higher order solver like Runge-Kutta, but it is assumed that the time steps are chosen small enough to keep method stable and accurate enough. In practice a value of $dt = 10^{-3}$ is chosen, which corresponds to the smallest length scale of the size s_{\min} of a plasmoid at birth.

Initial Conditions

The initial condition is chosen equivalently to [Petropoulou et al. \(2018\)](#) as a simple grid of plasmoids of initial size s_{\min} . Their momenta follow the distribution described in section 3.5 and their spatial separation is given by $\delta r = 10s_{\min}$. This is clearly only the simplest method to generate plasmoids and one could imagine other scenarios of initial conditions like a generation following a steady state distribution in size and mo-

mentum or the generation of two primary plasmoids allowing birth of new plasmoids only between them analogously to the PIC simulations. For reasons of comparability to Petropoulou et al. (2018) a grid is chosen as the starting point.

Growth

Looking at a single particle with exactly $r = 0$ and $\beta = 0$, its position is expected to stay constant and $\gamma = 1$ also implies $f_{\text{sup}} = 1$. This yields a linear growth for all times: $\frac{ds}{d\tau} = \beta_g$. This is shown in fig. 3.15.

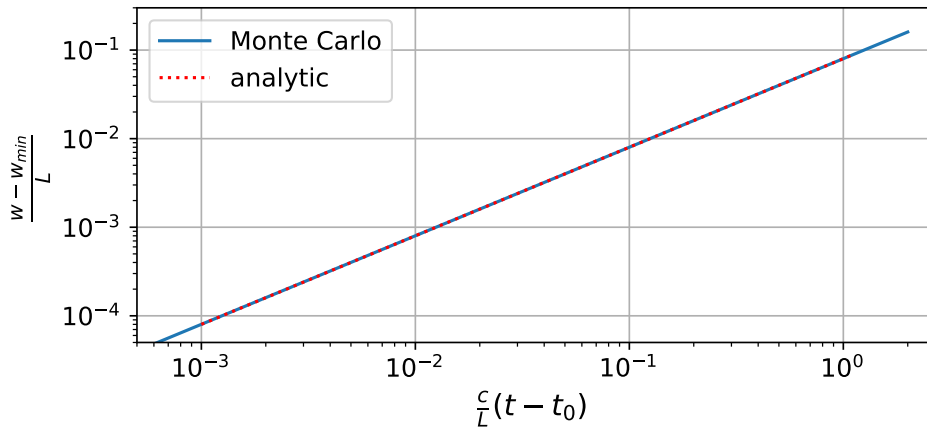


Figure 3.15.: Linear growth of a single plasmoid and the analytic expectation.

Solving Only the Equations of Growth and Motion

As a next crosscheck, eqs. (3.20) and (3.21) are solved without the generation of new plasmoids and without any mergers. This is achieved by setting the spread of the distribution of initial momenta to zero, $\sigma_{p_0} = 0$ and the plasmoid's initial momenta follow exactly eq. (3.19). This is shown for $\sigma = 10$ in the lower plot of fig. 3.16. The blue dots are the initial conditions of each particle and follow exactly the hyperbolic tangent. The green band visualises standard deviation as used in the following simulations.

The plot in the upper left of fig. 3.16 shows the simulated evolution of the particle's trajectories. As there is no spread in the initial momentum, the plasmoids move always away from the center, except for the one at $x = 0$, which stays at its position according to the previous paragraph. Thus the outer plasmoids already move close to the speed of light (slope ± 1), while for the ones originating closely from the centre still acceleration is visible. The colour shows the velocity in units of the speed of light. It is clearly visible that only the plasmoids born around $x = 0$ show significant growth. This can be understood by looking also at the plot in the upper right. It shows the growth of the plasmoids in time, where the colour denotes the speed. The plasmoids initiated far away from the centre correspond to the slower lines on the bottom. The sudden stop of growth is the intended stop of the growth due to the suppression $f_{\text{sup}}(\hat{p})$ and happens always at the same momentum slightly above $\hat{p}_{\text{sup}} = 2$. Since the outer plasmoids are

already generated with a much higher momentum and therefore reach this limit very fast, their growth stops early and their velocity converges towards the final limit of $\sqrt{\sigma}$. In contrast to that, plasmoids from the centre can grow much longer and usually do not reach \hat{p}_{sup} . This in turn also slows down their acceleration and they can grow to much higher sizes.

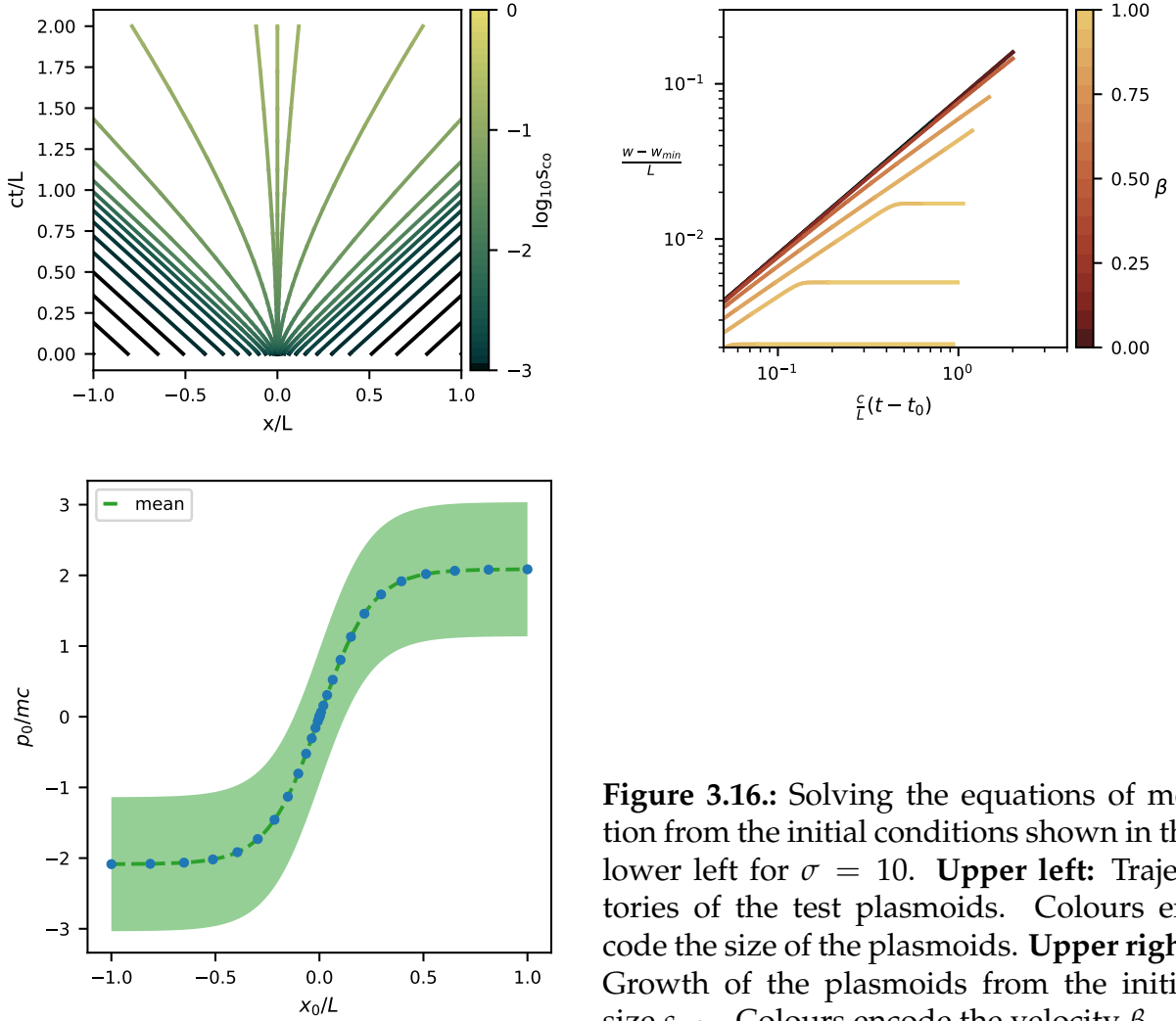


Figure 3.16.: Solving the equations of motion from the initial conditions shown in the lower left for $\sigma = 10$. **Upper left:** Trajectories of the test plasmoids. Colours encode the size of the plasmoids. **Upper right:** Growth of the plasmoids from the initial size s_{\min} . Colours encode the velocity β .

Mergers and Losses at Boundaries

In addition to the growth and motion of the particles, two other effects influence the evolution of a plasmoid. First, collisions of two plasmoids will arise at some point. Following the concept of a statistical treatment, the growth rate of the plasmoids already includes their growth through mergers on an average base. Thus, the mergers are simply handled by keeping the bigger plasmoid and dropping the smaller one. Second, plasmoids that leave the system are also dropped once they are completely outside of the system.

In both cases the decision is based on the size of the plasmoid along the direction of motion. Based on the results from PIC simulations, this is assumed to be $l_{\text{comoving}} = \frac{3}{2}w$ in the comoving frame, which transforms to $l_{\text{layer}} = l_{\text{comoving}}/\Gamma = \frac{3}{2}w/\Gamma$ in the layer's rest frame. The criterion for a merger is then that two neighbouring plasmoids overlap. The influence of different merger criteria on the size distribution has been investigated in [Petropoulou et al. \(2018\)](#) and no significant effect between the proposed methods was found. Furthermore, a plasmoid is dropped from the layer, as soon as it has left the layer with its complete size. This has a particular influence on the size distribution of the layer, since the creation of "holes" at the merger of two large plasmoids will trigger a large number of new plasmoids with the initial size.

Birth of New Plasmoids

If there is enough space between two plasmoids or the outermost plasmoid and the border, a new plasmoid is generated uniformly distributed in the free space. Its initial size is the minimum size of $s_{\min} = 10^{-3}$ and the momentum is sampled from eq. (3.19). However, no hard upper limit is set to the momentum, as proposed by [Petropoulou et al. \(2018\)](#), since these plasmoids occur rarely, are too fast to grow and will be absorbed by a larger and slower plasmoid soon. Assuming that the time step size is sufficiently small, it is checked at the end of every time step, whether there is enough free space to add plasmoids to the layer. However, only one plasmoid is added per gap, motivated by the fact that this becomes equivalent to adding multiple plasmoids in bigger gaps as long as the time step is small enough. It is furthermore worth to notice that there are two different effects causing the birth of new plasmoids. The first and most intuitive one is simply the difference in the speed of two plasmoids, which could cause a growing distance between the two. The other possibility for the creation of a gap is due to the merger of two bigger plasmoids. Since the smaller plasmoid is simply dropped from the system, this can cause big holes for big plasmoids.

3.6.2. Results for a Complete Layer

The developed code is now used to create realisations of current layers for different values of the magnetisation. The parameters for the growth suppression are taken from [Petropoulou et al. \(2018\)](#) and the results for the representative value $\sigma = 10$ are presented and compared to the latter. Then, the same is done for a higher ($\sigma = 50$) and a lower ($\sigma = 3$) value, and the consistency with the literature is investigated.

Results for $\sigma = 10$

Figure 3.17 shows the results in the form of three plots: On the top, the evolution of the layer is plotted in a diagram with position versus time, the lower left shows the distribution of the initial position and momentum for each plasmoid and the lower right shows the growth of each particle with respect to time.

In the plot of the evolution of the layer in the top and the one of the growth on the lower right, all plasmoids with a life time of less than $0.35L/c$ are not included, in analogy to fig. 3.10 and fig. 3.12. In contrast to the evolution plot from [Sironi, Giannios, and](#)

[Petropoulou \(2016\)](#), the width of a plasmoid is simply given by the size of its line and the colour denotes its velocity in terms of the speed of light. In general, a similar behaviour can be seen that plasmoids move outwards and that the biggest plasmoids emerge from the centre. It can also be observed that plasmoids with a small initial speed (dark) populate especially the central region and grow to much larger final sizes as faster ones (bright). This fits to the expectation from the growth suppression above a threshold momentum A_{sup} , which corresponds to the kink at which the lines become constant in the growth plot. The observation of plasmoids moving inwards can be understood from the fact that the initial momentum scatters around the mean value with a standard deviation of $0.3\sqrt{\sigma}$, which yields also inwards moving plasmoids, although rather rarely. The plot of the initial values shows also to regions, where the produced plasmoids accumulated. This corresponds to the region behind the biggest plasmoids, where permanently new plasmoids are born and have no chance to survive against those big ones.

In order to draw quantitative conclusions of the underlying statistical distribution, the 2 dimensional histograms in size and momentum are shown in fig. 3.18 for different time slices of the evolution. The plot on the upper left shows the initial distribution, where the plasmoids had no time for growth or acceleration. It is thus peaked around the initial size $s_{\min} = 10^{-3}$ and the asymptotic mean initial momentum for initial positions far from the centre of $|p| = 0.66\sqrt{\sigma}$. Comparison to a slightly later time slice in the plot right to it shows two effects, which can be best understood together with the plot on the lower right. It shows the temporal evolution of the plasmoids from fig. 3.16, which were produced at the same time following exactly the mean initial momentum distribution and without including the effects of mergers. This gives an intuition of the trajectory of a plasmoid in the size-momentum-histogram for the absence of mergers. The trajectories increase all in both quantities with a slope becoming larger with the initial momentum. At the threshold momentum A_{sup} the growth of those plasmoids who accelerated up to this momentum is suppressed and they follow vertical lines of acceleration only. Since many plasmoids are produced with a initial momentum around $|p| = 0.66\sqrt{\sigma}$, they do not really grow a lot and end up in the first, smallest size bin. Their acceleration is limited by construction to a value of $|p|/\sqrt{\sigma} = 1 + 0.66 + \text{initial spread}$, coming from the limit of the hyperbolic tangent in the relation between momentum and position over size, eq. (3.17), and the initial momentum distribution. The later stages (plot in the upper right for $0.1 \leq \tau \leq 0.2$ and lower left $1.9 \leq \tau \leq 2.0$) show exactly this structure: A regime in the first size bin, a regime with the plasmoids which grew significantly but show no growth (moving vertically) and one with those that show significant growth (moving also to the right). The fact that the plasmoids accumulate at the highest sizes follows from the bias introduced by the merging method of dropping always the smaller plasmoid. After about one light-crossing time the distribution does not change significantly from the one shown in the lower left.

To compare these results to the ones from [Petropoulou et al. \(2018\)](#), the projections to the size and momentum histograms are shown in fig. 3.19. To account for the statistical fluctuation, 10 realisations (light grey) are averaged. The size plot shows in general a similar, decreasing behaviour, but the flattening at small sizes and the steeper power

law at larger sizes are not reproduced, even within the fluctuations of the different realisations. In case of the momentum histogram the shape of both distributions seem similar, but the one from [Petropoulou et al. \(2018\)](#) seems scaled down by a factor of about two. The origin of this difference is still not resolved, but the distribution from the code developed within this thesis is as expected dominated by the regime of the first size bin peaking around $|p|/\sqrt{\sigma} = 1.66$ and a second population of plasmoids which have not arrived their final momentum yet. Cutting on a minimum size can basically eliminate most of the higher momenta, but is neither mentioned in [Petropoulou et al. \(2018\)](#) nor easy to justify. It is also worth to notice that the width of both first bins is chosen as the plots from [Petropoulou et al. \(2018\)](#) suggest under the assumption of a constant bin width, although this leads to bin with half of it outside of the physical range. This might introduce systematic effects to the first bin.

The origin of the difference between this code and [Petropoulou et al. \(2018\)](#) can either arise from a difference in the used and the quoted parameters (see table 3.1) or in a difference of the steps or their order. Changing the order of the processes does not resolve the difference. Apart from [Petropoulou et al. \(2018\)](#) that changing the merger criterion does not change the results, this showed no difference as well. Furthermore, removing the plasmoids already as soon as their centre lies outside of the layer's edge, lead only to a significant increase of the first size bin, since this creates large gaps in the case of big plasmoids. Also changing the way of introducing new plasmoids from once at a time to $N_{\text{new}} \approx dx/\delta x$ at a time did not resolve the difference.

parameter	$\sigma = 3$	$\sigma = 10$	$\sigma = 50$
β_a	0.1	0.12	0.13
β_g	0.06	0.08	0.1
A_{sup}	0.86	0.77	0.63
B_{sup}	0.019	0.033	0.024

Table 3.1.: Values used for the MC calculation, taken from [Petropoulou et al. \(2018\)](#).

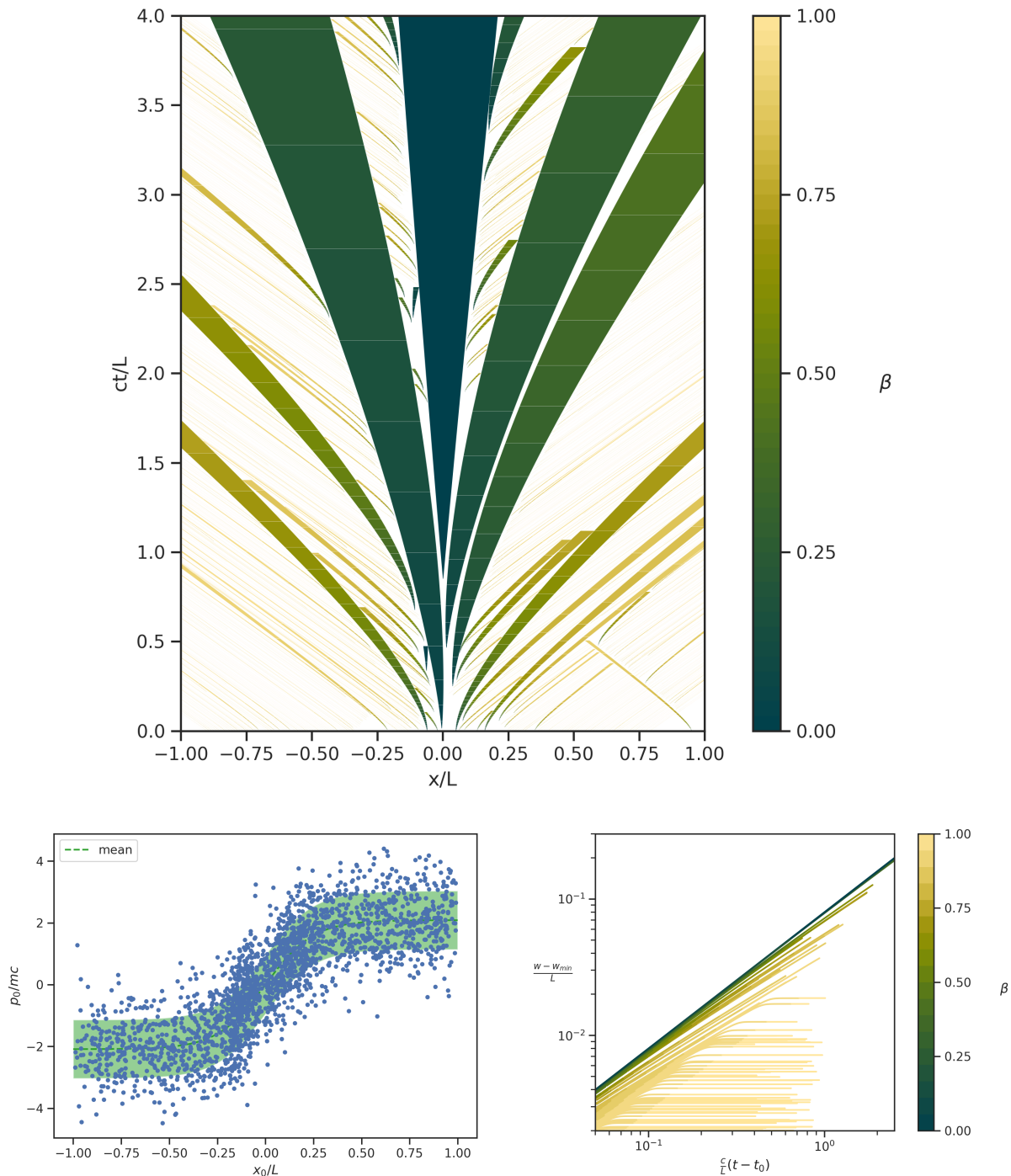


Figure 3.17.: Exemplary reconnection layer for $\sigma = 10$: **Top:** The trajectories of all plasmoids with a lifetime above $0.35L/c$ are plotted. The width of the line corresponds to the plasmoid's width and the colour to its speed in units of the speed of light. **Lower right:** Plot of the increase in size of the same plasmoids against time with the same colour encoding. **Lower left:** Initial position and momentum of all plasmoids from the layer with the mean and standard deviation of the underlying distribution.

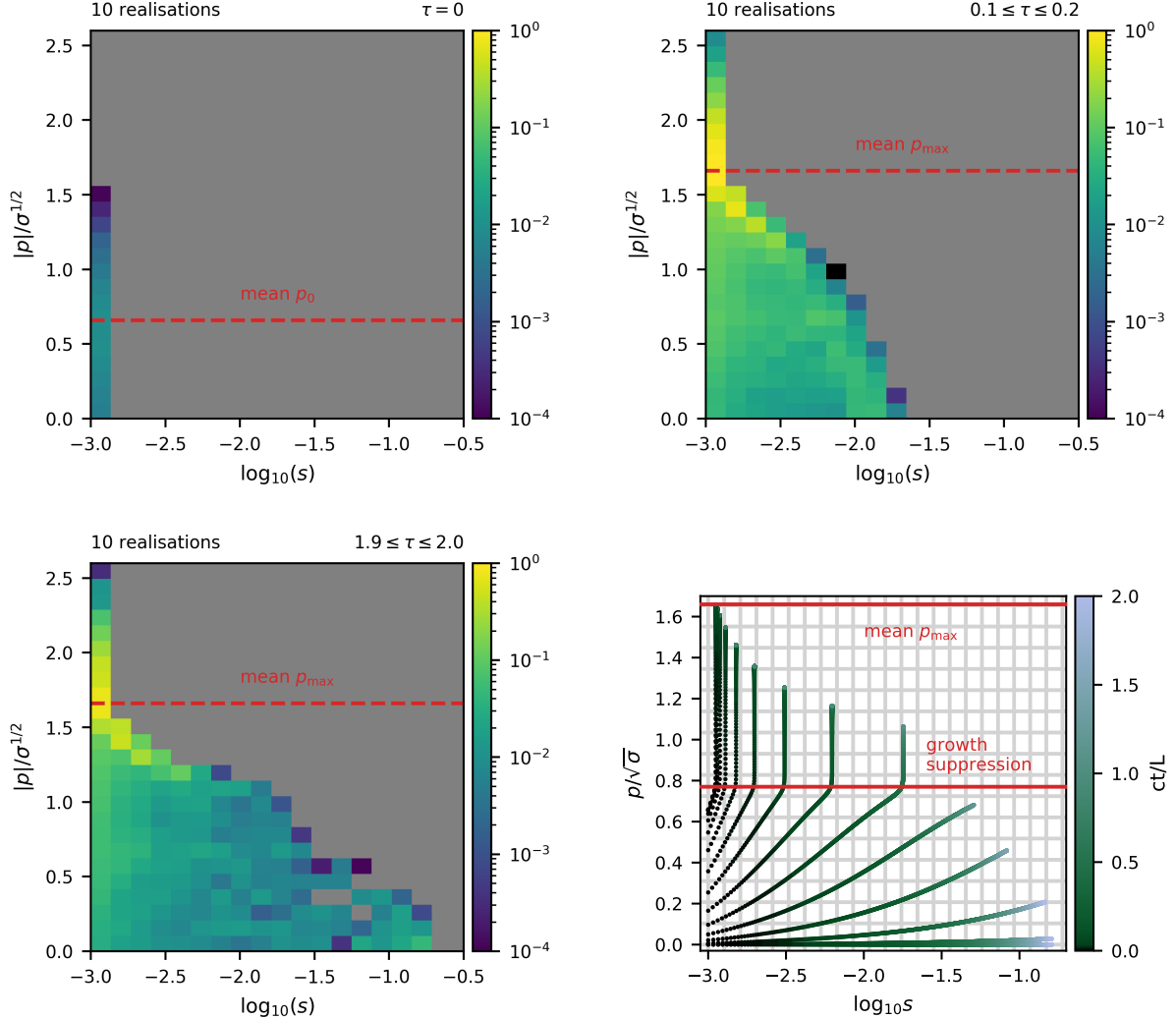


Figure 3.18.: Normalised size-momentum histograms at the initialisation ($\tau = 0$, upper left), for an early time ($0.1 \leq \tau \leq 0.2$, upper right) and for a late time ($1.9 \leq \tau \leq 2.0$, lower left). All histograms are integrated in time and space and averaged over 10 realisations. The dashed red lines correspond to the average momentum of the initial distribution at the beginning and the average maximum momentum with an additional component from the limiting case $\tanh(\beta_a/\sqrt{\sigma}(r - r_0)/s) \rightarrow 1$. The plot in the lower right visualises typical trajectories, which are taken from the test plasmoids simulated in section 3.6.1. Colours indicate the temporal evolution. The upper red line has the same meaning as in the other plots, while the lower one marks the momentum, at which the growth is suppressed.

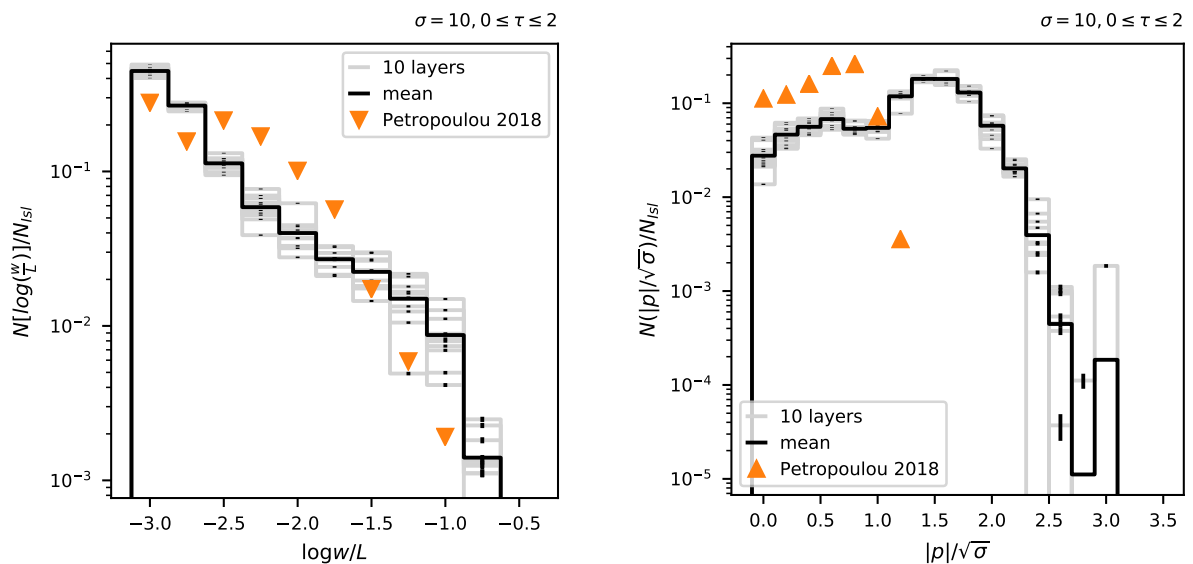


Figure 3.19.: Histograms of size (left) and momentum distribution (right) integrated in time ($0 \leq \tau \leq 2.0$) and space ($-1 \leq r \leq 1$) and normalised to the total number of plasmoids and time steps. 10 realisations are denoted in grey with errors in black and their average is shown in black. The orange triangles are taken from [Petropoulou et al. \(2018\)](#) and the binning is chosen correspondingly.

Variation of the Magnetisation

Changing the parameters to the values from table 3.1 for a significantly lower and higher magnetisation, the performance of the code can also be investigated in this region of the parameter space. With the increase of β_a and β_g and the decrease for A_{sup} and B_{sup} with the magnetisation, a faster but shorter lasting growth with stronger acceleration is expected. This creates slimmer lines in the case of $\sigma = 3$ and thicker ones for $\sigma = 50$.

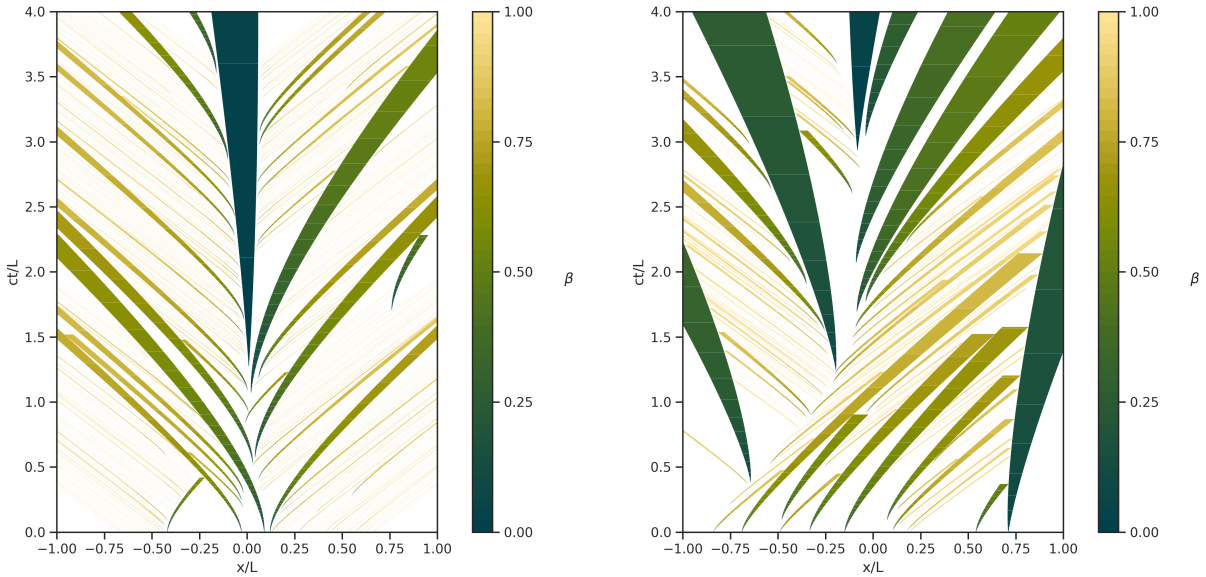


Figure 3.20.: Comparison of the trajectories of the plasmoids with a lifetime above $0.35L/c$ for a lower ($\sigma = 3$, left) and a higher ($\sigma = 50$, right) magnetisation, similar to fig. 3.17. The colour indicates the plasmoid's velocity in units of the speed of light.

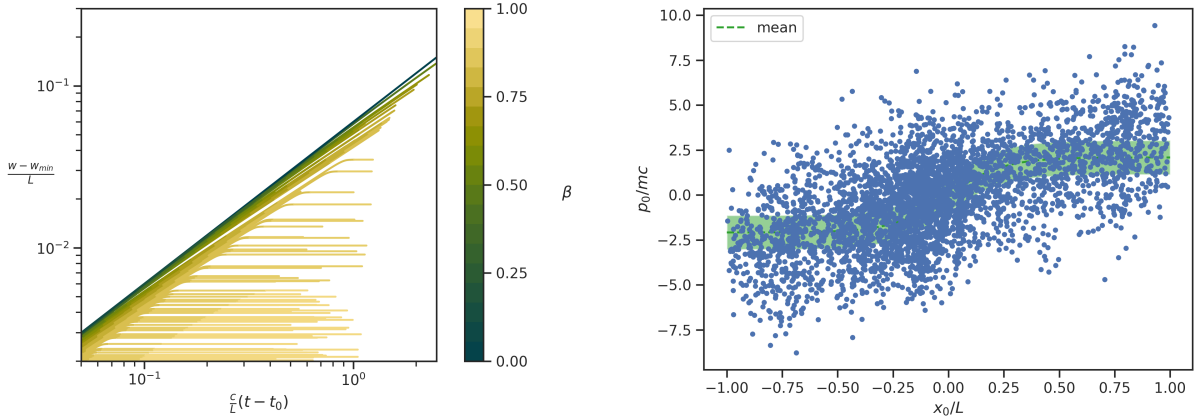


Figure 3.21.: Comparison of the growth of the plasmoids with a lifetime above $0.35L/c$ for a lower ($\sigma = 3$, left) and a higher ($\sigma = 50$, right) magnetisation, similar to fig. 3.17. The colour indicates the plasmoid's velocity in units of the speed of light.

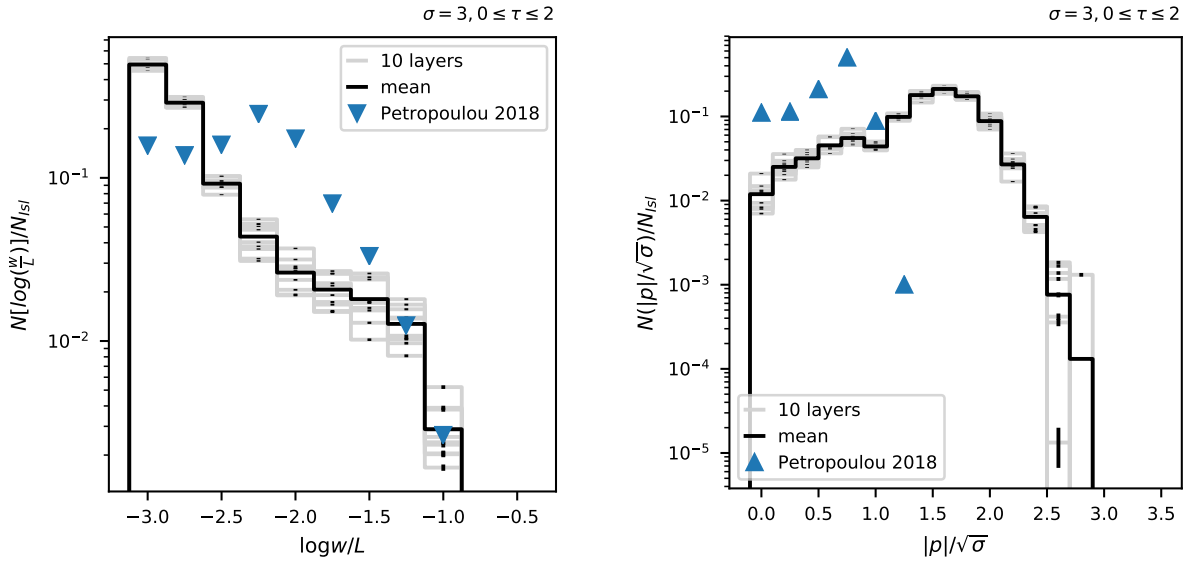


Figure 3.22.: Histograms of size (left) and momentum distribution (right) for a magnetisation $\sigma = 3$ integrated in time ($0 \leq \tau \leq 2.0$) and space ($-1 \leq r \leq 1$) and normalised to the total number of plasmoids and time steps. 10 realisations are denoted in grey with errors in black and their average is shown in black. The blue triangles are taken from [Petropoulou et al. \(2018\)](#) and the binning is chosen correspondingly.

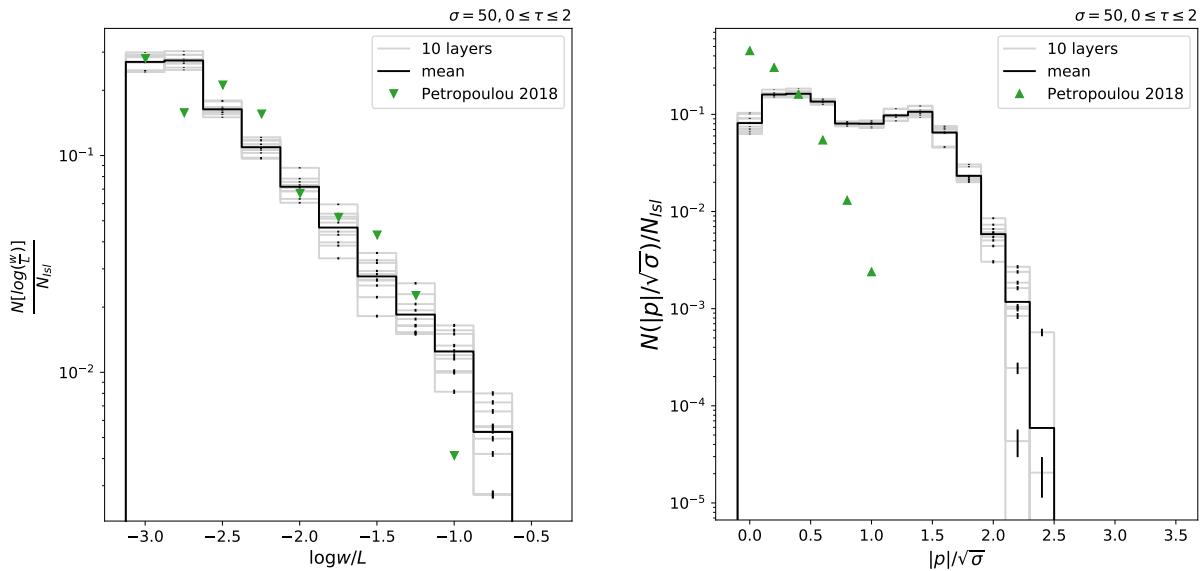


Figure 3.23.: Histograms of size (left) and momentum distribution (right) for a magnetisation $\sigma = 50$ integrated in time ($0 \leq \tau \leq 2.0$) and space ($-1 \leq r \leq 1$) and normalised to the total number of plasmoids and time steps. 10 realisations are denoted in grey with errors in black and their average is shown in black. The blue triangles are taken from [Petropoulou et al. \(2018\)](#) and the binning is chosen correspondingly.

3.6.3. Long-Term Evolution

The question of how the system evolves for longer times than the value of $2L/c$ that is used in [Petropoulou et al. \(2018\)](#) is of particular interest for the application to explain blazar variability on longer times scales like years. The assumption of a steady state implies by definition an infinitely long lasting stability. PIC simulations in [Sironi, Giannios, and Petropoulou \(2016\)](#) confirmed this up to $14L/c$ and showed a constant maximum plasmoid size of about 20 % of the layer's size. However, the developed code does not show such a pronounced stability, but rather a trend towards higher plasmoids with less momentum. This can be seen in fig. 3.24, where the size and momentum distributions analogue to the last section are plotted in bins of two light-crossing times up to twenty. These large plasmoids are called *monster* plasmoids and their size is in contrast to the findings in PIC simulations not limited about 20 % of the layer's size. To visualise this, the evolution of two layers for $\tau = 50$ is given in fig. 3.25. While the right layer consists of monster plasmoids which still have enough momentum to exit to the sides, the left one shows the even extremer case of a plasmoid which is moving much slower than it growths. After a bit more than 20 light-crossing times it completely fills up the layer, which is not expected to be a stable layer of magnetic reconnection. This shows that the MC approach is not very well suited to be applied to an evolution significantly longer than a few light-crossing times. However, this has to be studied again, if modifications are applied to the MC-procedure to change the distributions of size and momentum.

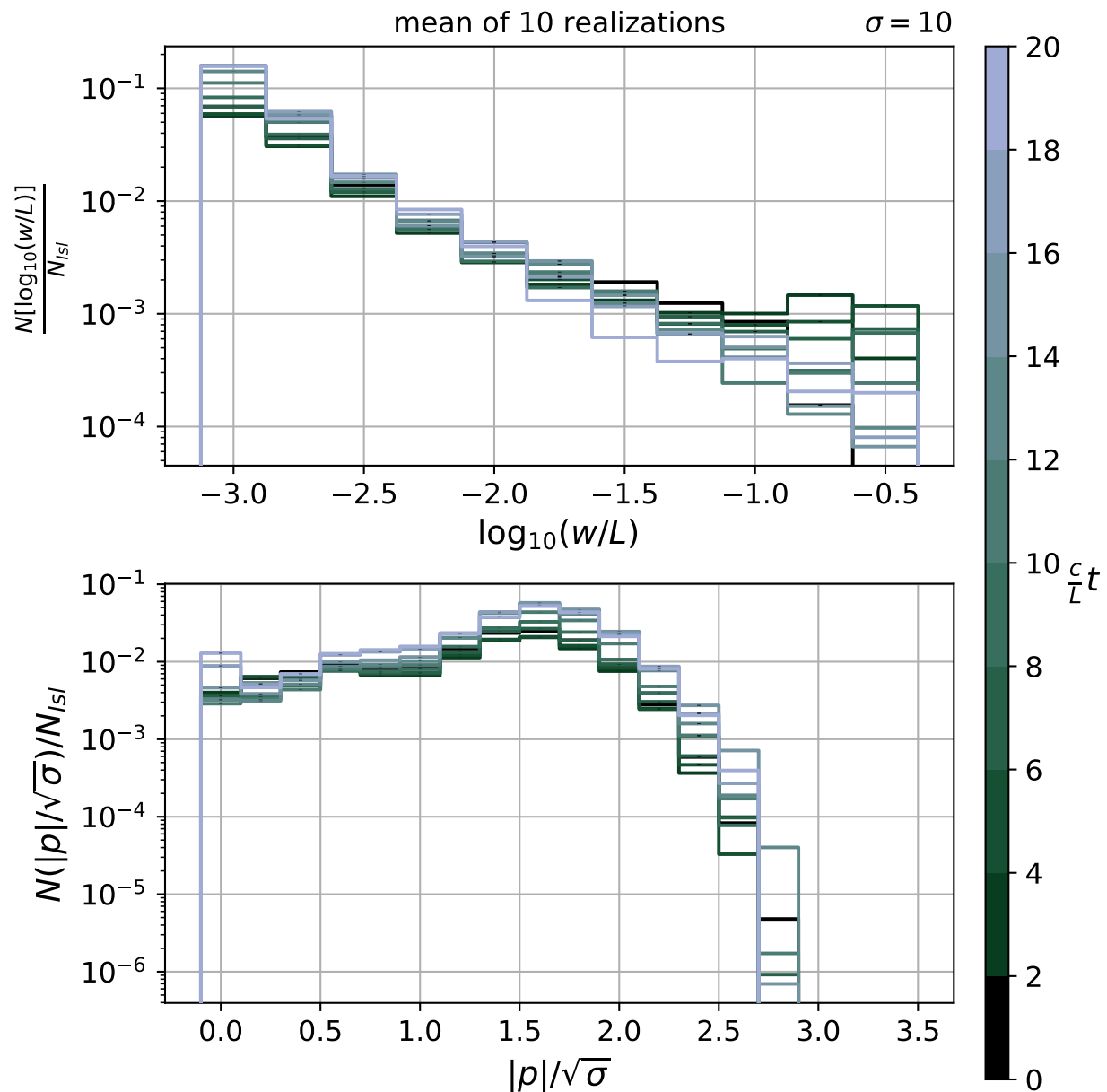


Figure 3.24.: Mean of 10 realisations of the histograms of size (top) and momentum (bottom) integrated in time slices of $\Delta\tau = 2$ and in space and normalised to the number of plasmoids and time steps within each slice of time.

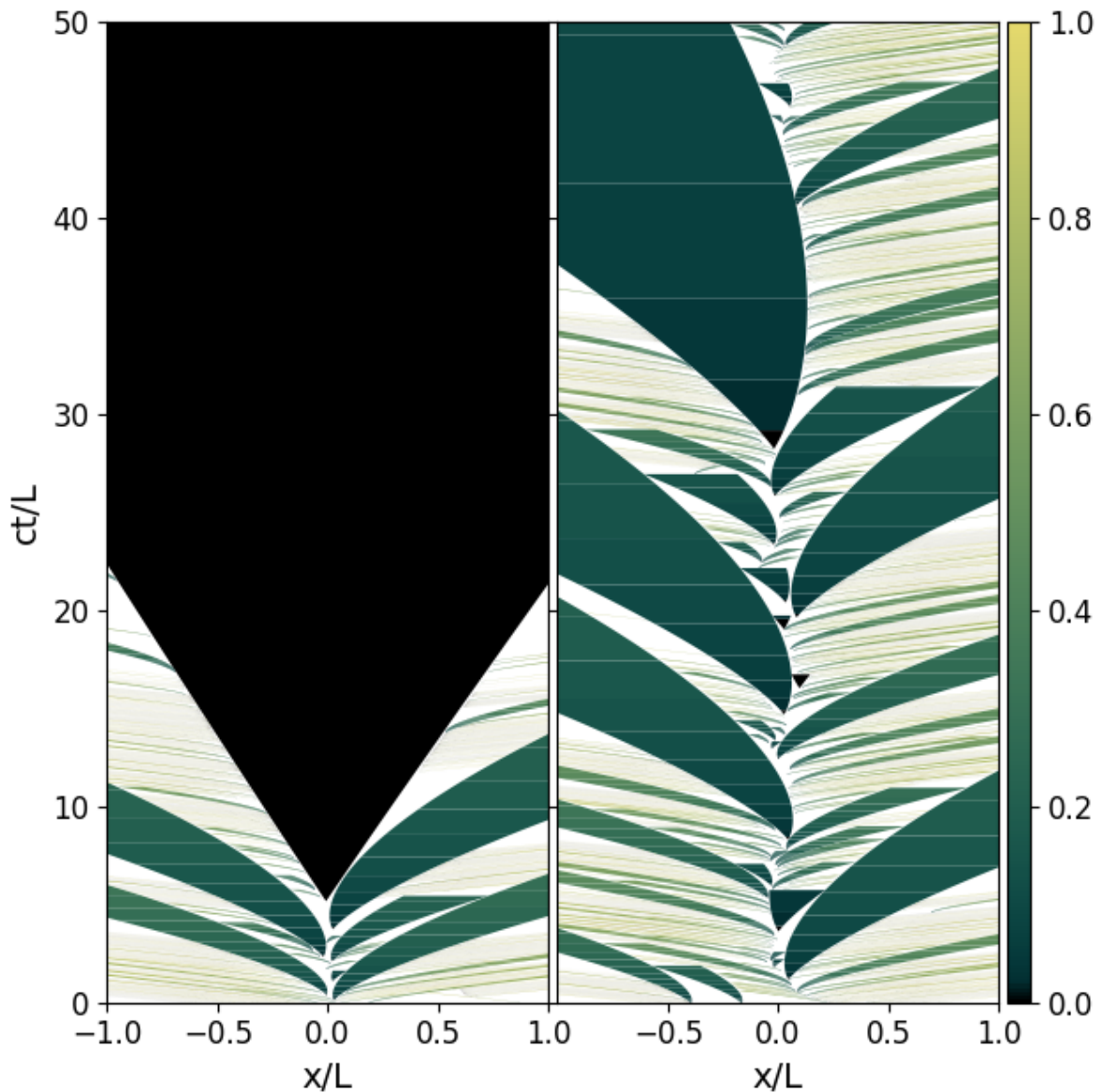


Figure 3.25.: Two exemplary Layers showing the long-term evolution of the MC code up to $\tau = 50$ for a magnetisation of $\sigma = 10$. The colorbar on the right indicates the speed of a plasmoid in units of the speed of light. The width of each line denotes the plasmoid's width and only plasmoids with a lifetime above $0.35L/c$ are shown.

4

Non-Thermal Radiation Modelling

The goal of this chapter is to model the radiative processes between the electron-positron pairs and the photons inside of a plasmoid. Therefore, first the radiative processes taken into account together with the crucial effects of special relativity are introduced. Then, the numerical implementation is described and several crosschecks in regimes with analytical solutions are done. To apply the code also to the radiation in a plasmoid, the dependencies on the plasmoids properties are introduced. The results for plasmoids with different final sizes as measured in the plasmoids rest frame and the observed emission in the observers frame are presented and discussed.

4.1. Normalisations

As often in physics it is useful to normalise the quantities of interest to reference values. This removes the dimensionality of quantities, keeps numerical values within reasonable ranges and allows better interpretation of the underlying processes in the system, independent of the actual absolute number. In agreement with chapter 3 and following the convention of [Mastichiadis and Kirk \(1995\)](#), lengths will be normalised to the length of the reconnection layer L and times to the respective light crossing time c/L . Furthermore, volumes are used with respect to the *Thomson volume* $\sigma_T L$ based on the Thomson cross section σ_T . Energies will be normalised to the rest mass energy of an electron $m_e c^2$, which yields for the electron energy simply its Lorentz-factor and for the photons with frequency ν a quantity called $x = h\nu/m_e c^2$. Furthermore, also temperatures T will be rescaled to the rest energy of an electron $\Theta = kT/m_e c^2$.

$$\tau = \frac{t}{L/c} \quad \tilde{V} = \frac{V}{\sigma_T L} \quad \gamma = \frac{E_E}{m_e c^2} \quad x = \frac{h\nu}{m_e c^2} \quad \Theta = \frac{kT}{m_e c^2} \quad (4.1)$$

4.2. Number Density and Compactness

To quantify the evolution of the system, one would generally look at the phase space density $f(\mathbf{r}, \mathbf{p}, t)$, which describes the number of particles in the system at position \mathbf{r} and with momentum \mathbf{p} at the time t . However, this approach is significantly simplified by three assumptions. The most important assumptions are spatial homogeneity and isotropy: $f = f(\mathbf{p}, t)$. Furthermore, isotropy in momentum space is assumed,

such that the phase space density depends only on the magnitude p of the momentum: $f = f(p, t)$. Next, p can be substituted by the energy of a particle. Integrating this over a Thomson volume and the sphere of isotropic momenta, one arrives at the number density in space and energy normalised to eq. (4.1) (due to spatial homogeneity the integration is equivalent to the norm of the volume). Henceforth this quantity is called the number density and will be denoted by the symbol n .

$$n = \frac{dN}{d\tilde{E}} = \int_{\sigma_T L} dV \int d\Omega_p f \quad (4.2)$$

where $\tilde{E} = E/m_e c^2$ is the normalised energy γ or x . To compare this quantity to formulas in non-normalised variables, the following conversion factor is useful:

$$n = \frac{dN}{d\tilde{E}} = \frac{m_e c^2}{\sigma_T L} \frac{dN}{dE} \quad (4.3)$$

When normalising the energy density of a system, another commonly used parameter emerges, the compactness l :

$$l = \frac{\sigma_T L}{m_e c^2} \frac{dE}{dV} \quad (4.4)$$

4.3. Effects of Special Relativity

Dilation, Contraction and Doppler Effect

From a Lorentz-transformation it follows that if a source of signals moves at relativistic speeds, time dilation has to be considered. Let S be the system at rest and S' be moving with $\beta = u/c$. Then, an infinitesimal time interval dt' in S' is related to one in S by (time on clock at rest in S' measured in S) (Einstein 1905):

$$dt = \Gamma dt' \quad \text{with} \quad \Gamma = \frac{1}{\sqrt{1 - \beta^2}} \quad (4.5)$$

When taking into account the effects of the motion itself (for example if the clock emits two light signals towards the observer), light travelling effects have to be accounted for and the Doppler effect comes in (Einstein 1905). From fig. 4.1 it can be seen that an additional factor of $1 - \beta \cos(\theta)$ emerges:

$$dt = \Gamma(1 - \beta \cos(\theta)) dt' \quad (4.6)$$

As a frequency behaves inversely to time and the Doppler factor is defined for frequencies, one defines:

$$\nu = \underbrace{\frac{1}{\Gamma(1 - \beta \cos(\theta))}}_{\delta} \nu' \quad (4.7)$$

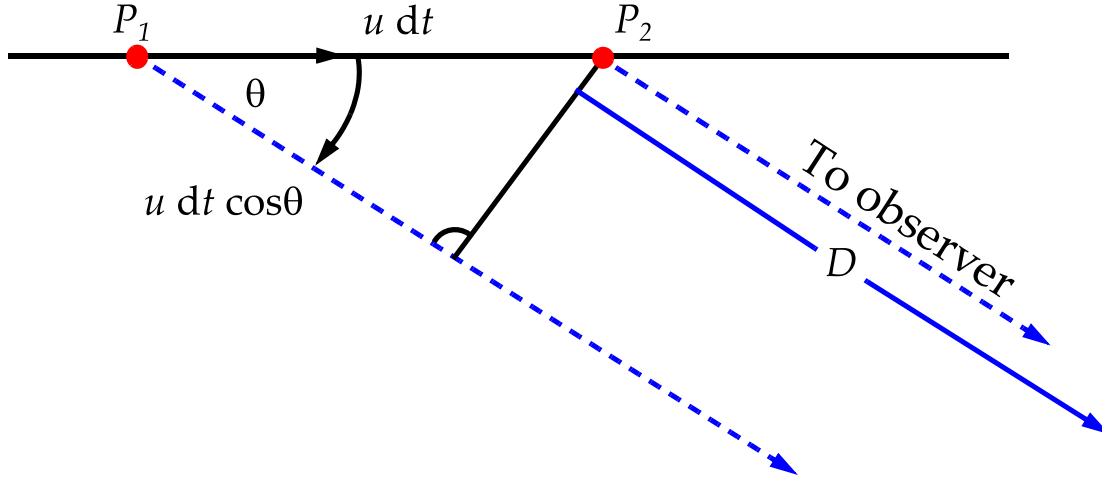


Figure 4.1.: Sketch for the derivation of the Doppler factor by taking the arrival time difference between the signal from points P_1 and P_2 .

Additionally, the same can be shown to hold also for the length contraction:

$$L = \delta L' \quad (4.8)$$

Relativistic Addition of Velocities

Following the ideas of Einsteins theory of special relativity, also the addition of velocities changes. This can be obtained by decomposing the velocities into a part parallel and perpendicular to the direction of motion and applying a Lorentz-transformation:

$$dy'_\parallel = \Gamma(dy_\parallel + u dt) = \Gamma(dy \cos(\theta) + u dt) \quad (4.9)$$

$$dy'_\perp = dy_\perp = dy \sin(\theta) \quad (4.10)$$

$$dt' = \Gamma\left(dt + \frac{u}{c} \frac{dy_\parallel}{c}\right) = \Gamma\left(dt + \frac{u}{c} \frac{dy \cos(\theta)}{c}\right) \quad (4.11)$$

Then the relativistic addition of velocities follows directly by considering dy'_\parallel / dt' and dy'_\perp / dt' and denoting $\beta_v = dy / dt / c$:

$$\beta'_\parallel = \frac{dy'_\parallel}{dt'} = \frac{\beta_v \cos \theta - \frac{u}{c}}{1 - \beta_v \frac{u}{c} \cos \theta} \quad \beta'_\perp = \frac{dy'_\perp}{dt'} = \frac{\beta_v \sin \theta}{\Gamma(1 - \beta_v \frac{u}{c} \cos \theta)} \quad (4.12)$$

The relation between the angles θ and θ' measured in S and S' respectively is given by relativistic aberration.

Relativistic Aberration

Einstein also showed in his paper how to transform angles in special relativity, what is known as relativistic aberration. Using eqs. (4.9) to (4.11), it can be shown that:

$$\tan(\theta) = \frac{dy_{\perp}}{dy_{\parallel}} = \frac{\beta \sin \theta'}{\Gamma(\frac{u}{c} + \beta \cos \theta')} \quad (4.13)$$

Furthermore, a solid angle transforms like $d\Omega' = \delta^2 d\Omega$, see ch. 22.3 of [Longair \(2011\)](#).

Intensities and Number Densities

The intensity I is defined as the energy $dE = mc^2 x dN$ of radiation which reaches a surface dA_{\perp} in a time dt from a solid angle $d\Omega$. Furthermore, the spectral intensity I_x is defined as the intensity within an energy bin dx . Knowing how all these quantities transform under boosts in special relativity, it can be shown that:

$$I_x = \delta^{-3} I'_x \quad (4.14)$$

For an isotropic source, the flux is emitted into all directions ($d\Omega = 4\pi$). In the boosted frame this changes due to the relativistic aberration to the smaller angle $d\Omega' = \delta^2 d\Omega = 4\pi\delta^2$. This leads to a compactification of an isotropic radiation field when seen from a relativistically moving observer. The spectral intensity is linked to the number density in the following way:

$$n = \frac{d\Omega}{hc} \frac{I_x}{x} \quad (4.15)$$

Then, the relativistic boost gives:

$$n' = \frac{\delta^2 d\Omega}{hc} \frac{\delta^3 I_x}{\delta x} = \delta^4 n \quad (4.16)$$

and finally:

$$n_{\text{obs}} = \delta_p^{-4} n_{\text{emitted}} \quad (4.17)$$

The four powers come from the transformation of the solid angle, the energy and the volume. For more details see also ch. 5 of [Dermer and Menon \(2009\)](#).

4.4. Black Body

A black body spectrum is completely characterised by one parameter: its temperature T . This determines the maximum of the distribution and its normalisation. It is useful to define it in units of the electron rest energy as well: $\Theta = kT/m_e c^2$. Using the intensity I_{ν} from Planck's law, the spectral number density of a black body can be written as:

$$\hat{n}_{\nu}(\nu) = \frac{\partial^2 N}{\partial V \partial \nu} = \frac{4\pi}{c} \frac{I_{\nu}(\nu)}{h\nu} = \frac{8\pi}{c^3} \frac{\nu^2}{e^{h\nu/kT} - 1} \quad (4.18)$$

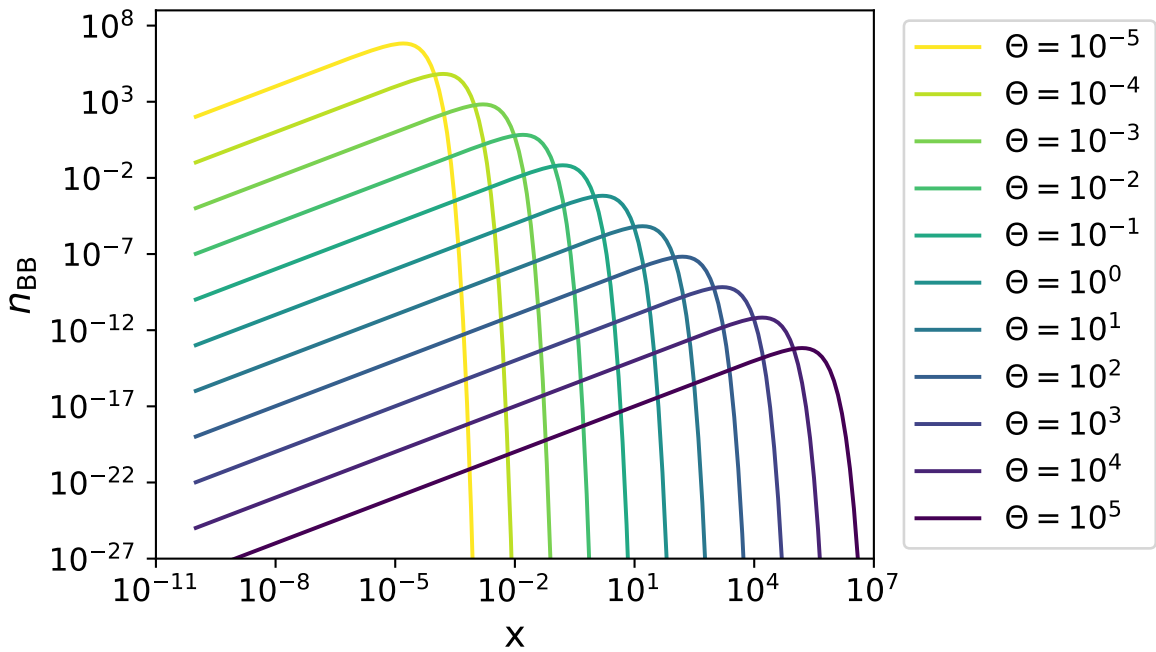


Figure 4.2.: Exemplary black body for a range of different temperatures.

In terms of the normalised spectral density this reads:

$$n_x(x) = \frac{m_e c^2}{h} n_\nu = \frac{m_e^3 c^3}{\pi^2 \hbar^3} \frac{x^2}{e^{x/\Theta} - 1} \quad (4.19)$$

In the limit of $x/\Theta \ll 1$ this can be approximated by the Rayleigh-Jeans law:

$$n_x(x) \approx \frac{m_e^3 c^3}{\pi^2 \hbar^3} \Theta x \quad (4.20)$$

Combining the formulae for both regimes, the black body can be calculated without numerical errors throughout the whole energy range, as shown in fig. 4.2. Furthermore, from the Stefan-Boltzmann law one can infer the energy density integrated over all energies (with the Stefan-Boltzmann constant $\sigma = \pi k^4 / 60 \hbar^3 c^2$):

$$u_{BB} = \frac{4\sigma}{c} T^4 \quad (4.21)$$

With this, the black body's spectral number density can be expressed also as a function of its energy density:

$$n_x(x) = \frac{U_{BB}}{\frac{4\sigma}{c} T^4} n_x = \frac{\sigma_T L}{mc^2} U_{BB} \frac{15}{\pi^4 \Theta^4} \frac{x^2}{e^{x/\Theta} - 1} = l_{BB} \frac{15}{\pi^4 \Theta^4} \frac{x^2}{e^{x/\Theta} - 1} \quad (4.22)$$

Here the l_{BB} is the compactness parameter of the black body. From the Stefan-Boltzmann law one finds: $l_{BB} = 4\sigma T^4 \sigma_T L / (mc^3)$. Equation (4.22) deviates from [Mastichiadis and Kirk \(1995\)](#) by a factor of 3 and it is unclear why. However, a value of $l_{BB} = 1/3$ is used for their calculations and an unambiguous definition of l_{BB} itself is not given in the paper, thus the definition of eq. (4.22) is used in the following.

Defining the norm of the black body spectrum via its energy density, the effect of the decrease depending on the distance to the observer can be included in a very convenient manner. For a spherical symmetric geometry, the energy density simply scales with the change of the volume. Since it is common to formulate this in terms of the luminosity of the black body, the energy density at a distance d can be expressed as:

$$u_{BB} = \frac{1}{c} \frac{L_{BB}}{4\pi d^2} \quad (4.23)$$

4.5. Radiative Processes

For a completely self-consistent picture, the PIC simulations also need to include radiative effects. These would lead to additional force terms when calculating the new position and momentum of the particles. However, for reasons of feasibility and simplicity it is assumed that the effects of energy losses due to photons in the systems do not effect the evolution significantly. Then, the evolution of the plasmoid instability can be treated separately from the modelling of the radiative processes and thus the evolution of emitted photons.

In this thesis, a system consisting of electron-positron pairs and photons is considered. It will be characterised by the photon number density n_γ and the electron-positron number density n_e . The included radiative effects are synchrotron radiation including the effect of synchrotron self-absorption at high optical thicknesses, inverse Compton-scattering in both, the Thomson and the Klein-Nishina regime and the production of new electron-positron pairs.

All processes connect the energy content of one species with the other one by transferring energy from one population to another in combination with the annihilation and creation of particles. The structure to characterise this is in its most general form a rate depending on the energy of the participating particles. All considered effects can be described by an interaction between two electrons (or their anti-particles, positrons) and two photons. In the language of Feynman diagrams becomes particularly clear, as there *simply* incoming and outgoing particles are switched¹. So the rate of interaction between the four particles generally depends on the energies of the four particles: $\hat{\eta}(E_1, E_2, E_3, E_4)$. Energy conservation imposes an additional constraint, which results in the dependency on only the energy of the two incoming particles and an outgoing one: $\eta_{3/4}(E_1, E_2, E_{out})$. The change in the spectral density of particles of type 3/4 can

¹Strictly speaking this picture is a bit oversimplified, since the photons of the magnetic field are virtual photons and the Feynman diagram is bit more complex.

then be obtained by a convolution with the spectral densities of the particles 1 and 2:

$$\frac{\partial n_{3/4}}{\partial t} \Big|_{\text{some process}} = \int dE_1 n_1(E_1) \int dE_2 n_2(E_2) \eta_{3/4}(E_1, E_2, E_{\text{out}}) \quad (4.24)$$

Using this approach the temporal evolution of the number density of multiple species can be modelled self consistently. However, this results in a set of integro-differential equations, which numerical solving can be rather challenging. This motivates the simplification of at least some terms, which can be approximated as *continuous* energy losses or gains. Then following the derivation in ch. 7.5.1 of [Longair \(2011\)](#), the process can be treated as an advection term in energy. If the energy loss rate of a given process typically called $b(E) = dE/dt = \eta \cdot \Delta E(E)$ with the energy loss or gain $\Delta E(E)$, the change of the number density can also be expressed as:

$$\frac{\partial n}{\partial t} = \frac{d}{dE} [b(E)n(E, t)] \quad (4.25)$$

The determination of all the terms for each process allows then a consistent simulation of the temporal evolution of the system. In the following sections, for each of the three effects the results taken from [Mastichiadis and Kirk \(1995\)](#) are summarised.

4.5.1. Synchrotron Radiation

When looking at the motion of a charged particle in a magnetic field, the solution of its equation of motion can be divided into a constant velocity along the magnetic field lines with an additional gyration around this path (see fig. 4.3). The radius of this spiral motion is usually much smaller than the length scale of variation the magnetic field lines. Furthermore, it is known that a charged particle moving in an electromagnetic field produces electromagnetic radiation. This can be understood by the nice explanation of J. J. Thompson, based on the fact that the speed of information of a change in the field of a charge can propagate at most at the speed of light. During an acceleration there must be therefore a perturbation of the fields at some distance, which can be interpreted as electromagnetic radiation, see fig. 4.4. Mathematically this was first expressed by Liénard and Wiechert in 1900 by deriving the potentials from Maxwell's equations. In this way the power radiated away by a moving charge can be calculated and gives Larmor's formula ([Jackson 1998](#)):

$$\frac{dE}{dt} = \frac{2q^2\gamma^4}{3c^3} [a_{\perp}^2 + \gamma^2 a_{\parallel}^2] \quad (4.26)$$

Plugging in the trajectory of the gyration and adding up both polarisations, the rate of the emission of photons per energy dx by an electron with pitch angle θ compared to the magnetic field lines can be inferred:

$$\eta(x, \gamma) = \sqrt{3}\alpha_f \frac{Lm_e c}{h} \frac{B \sin \theta}{B_c} \frac{F(x/x_c)}{x} \quad (4.27)$$

Here α_f is the fine structure constant and $F(x)$ is defined as in [Ginzburg and Syrovatskii](#)

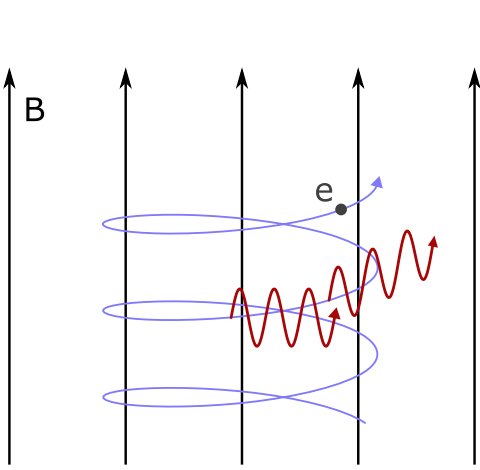


Figure 4.3.: On the length scale of one gyration the magnetic field is nearly constant and the electron gyrates around its directional vector. Due to the centripetal force keeping it on track, it is constantly accelerated and emits synchrotron radiation.

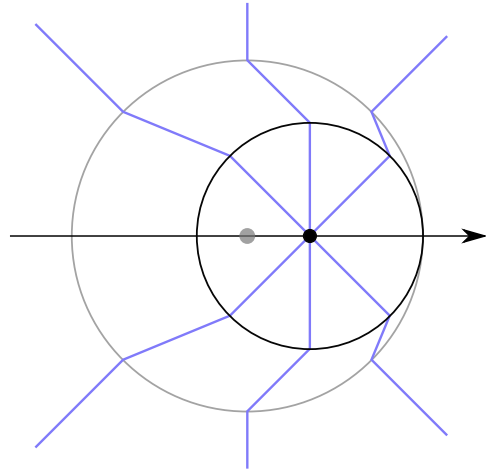


Figure 4.4.: According to J. J. Thomson, the charge moves instantaneously from the grey position to the black one. The circles show an exemplary distance, up to which the information of the acceleration has already propagated. This yields a perturbation in the field lines, which can be interpreted as electromagnetic radiation.

(1965). The critical magnetic field B_c is defined via the characteristic frequency x_c , which can be related to the maximum of F at approximately:

$$x_{\text{syn, max}} = 0.29x_c = 0.29 \cdot \frac{3}{2} \sin \theta \underbrace{\frac{B}{B_c}}_b \gamma^2 \quad \text{with} \quad B_c = \frac{m_e^2 c^3}{e \hbar} \approx 4.41 \cdot 10^{13} \text{ G} \quad (4.28)$$

To simplify this further, a δ -approximation going back to Hoyle (1960) is made. This assumes that all the emission of the synchrotron radiation is sent out monochromatically at the maximum frequency:

$$\eta_\delta(x, \gamma) \approx \frac{q_0}{x_0} \delta(x - x_0) \quad (4.29)$$

The norm q_0 can be determined by equating the emitted power to the one obtained by eq. (4.27):

$$b_{\text{syn}}(\gamma) = \frac{dx}{d\tau} = \int_0^\infty dx x \eta(x) = 2 \underbrace{\frac{\sigma_T L}{m_e c^2} U_B}_{l_B} \gamma^2 \sin^2 \theta \approx \frac{4}{3} l_B \gamma^2 \quad (4.30)$$

$$\Rightarrow q_0 = \int_0^\infty dx x \eta_\delta(x) = b_{\text{syn}}(\gamma) = \frac{4}{3} l_B \gamma^2 \quad (4.31)$$

where the average over θ has been taken in the last step ($\langle \sin^2 \theta \rangle = 2/3$). The frequency

x_0 from eq. (4.29) is chosen to be the critical frequency: $x_0 = \hat{b}\gamma^2$:

$$\Rightarrow \eta_\delta(x, \gamma) = \frac{4}{3} \frac{l_B}{\hat{b}} \delta(x - \hat{b}\gamma^2) = \frac{2}{3} \frac{l_B}{\sqrt{\hat{b}^3 x}} \delta\left(\gamma - \sqrt{\frac{x}{\hat{b}}}\right) \quad (4.32)$$

Since in astrophysical environments magnetic fields are $\mathcal{O}(G)$ and $B \ll B_c$ also the relative energy loss of one electron is small: $x_0 \ll \gamma$. Then the process can be approximated as continuous and the electron loss term is obtained by plugging eq. (4.30) into eq. (4.25):

$$L_{\text{syn}}^e(\gamma, \tau) = \frac{4}{3} l_B \frac{d}{d\gamma} \left[\gamma^2 n_e(\gamma, \tau) \right] \quad (4.33)$$

The photon energy gain is given by weighting eq. (4.29) with the electron energy distribution:

$$Q_{\text{syn}}^\gamma(x, \tau) = \int_1^\infty d\gamma n_e(\gamma, \tau) \eta_\delta(x, \gamma) = \frac{2}{3} \frac{l_B}{\sqrt{\hat{b}^3 x}} n_e\left(\sqrt{\frac{x}{\hat{b}}}, \tau\right) \quad (4.34)$$

From the monochromatic δ -approximation one can also infer the maximal energy of the photon spectrum:

$$x_{\max} = \hat{b}\gamma_{\max}^2 \quad (4.35)$$

Synchrotron Self-Absorption

When looking at an extended volume of electrons emitting synchrotron radiation there is of course also a respective absorption process: synchrotron-self-absorption (SSA). Depending on the energy of the photon this divides the region into optically thin and thick regimes, which can be understood as an extension of the *real* optical thickness to a photon transmittivity not restricted to the optical waveband. In the optically thin regimes photons can escape the system on average without being absorbed. In contrast to this, in the optically thick regime, the same population of electrons emitting the photons re-absorbs them several times before they could leave the system. This can be described by the absorption coefficient α giving the inverse distance at which the number of photons decreases by one e-fold. Following the derivation of [Rybicki and Lightman \(1986\)](#) the absorption coefficient can be written in the following form for small photon energies compared to the electron energy:

$$\alpha(x) = \frac{1}{8\pi} \frac{h^3}{m^3 c^3} \frac{1}{\sigma_T L^2} \frac{1}{x^2} \int_1^\infty d\gamma x \eta(x, \gamma) \gamma^2 \frac{d}{d\gamma} \left[\frac{n_e(\gamma, t)}{\gamma^2} \right] \quad (4.36)$$

$$= \frac{\pi}{3\alpha_f L} \frac{1}{\sqrt{\hat{b}x}} \frac{d}{d\gamma} \left[\frac{n_e(\gamma, t)}{\gamma^2} \right] \Big|_{\gamma=\sqrt{x/\hat{b}}} \quad (4.37)$$

The effect of SSA is then treated as a simple loss term scaling with the size of the system in units of the layer R/L :

$$L_{\text{ssa}}^\gamma(x, \tau) = \frac{R}{L} \alpha(x) n_\gamma(x, \tau) \quad (4.38)$$

Synchrotron Radiation from a Power Law Spectrum

One important crosscheck of the above formulae is checking the spectral index of the resulting emission of synchrotron radiation from a power-law electron distribution:

$$n_e(\gamma) = K\gamma^{-p} \quad (4.39)$$

Plugging this into eq. (4.34) yields the emission of photons following a power law distribution with a spectral index of $-(p + 1)/2$. This result is based on the δ -approximation, however a more rigorous derivation comes to the same spectral index (Longair 2011). The additional effect of SSA on the spectral shape for this example can be either approximated from physical arguments, see ch. 8.7.1 of Longair (2011) or by using the delta approximation and assuming a steady state with the dominating contribution by synchrotron sources from eq. (4.34) and SSA-losses from eq. (4.38):

$$\frac{\partial n}{\partial \tau} \approx -\frac{R}{L}\alpha(x, \tau)n_\gamma(x, \tau) + Q_{\text{syn}}^\gamma(x, \tau) = 0 \quad (4.40)$$

$$\Rightarrow n_\gamma(x, \tau) \propto \frac{Q_{\text{syn}}^\gamma(x, \tau)}{\alpha(x, \tau)} \propto x^{3/2} \quad (4.41)$$

It is worth to notice that this result holds independently of the initial spectral index p .

4.5.2. Inverse Compton Scattering

The second variant of electron-photon scattering aside of synchrotron radiation is the effect of Compton Scattering. This is discussed in great detail in Blumenthal and Gould (1970) and the most important results are summarised in the following.

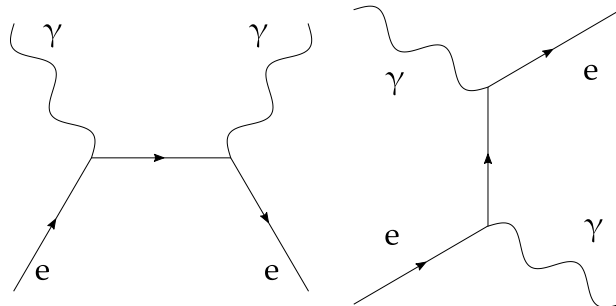


Figure 4.5.: Two exemplary Feynman diagrams of Compton scattering via the s-channel (left) and the t-channel (right) with time increasing from left to right.

Two example Feynman diagrams are shown in fig. 4.5. In contrast to synchrotron scattering now the photons are real photons from a radiation field. The treatment of this scattering can be categorised according to the energies of the electron γ and the photon x . In case of a non-relativistic electron ($\gamma \approx 1$) there are two regimes, first the commonly called Thomson scattering, where $\gamma x \ll 1$, the photon momentum is negligible and the

cross section can be treated without relativistic or quantum effects and yields simply the Thomson cross section σ_T . Increasing now the energy of the photon ($\gamma x \leq 1$), the photon momentum can no longer be neglected and a quantum treatment becomes necessary. This yields the typical Compton scattering, where usually the photon transfers energy to electron. This changes now, if the electron becomes relativistic ($\gamma \gg 1$). Then the electron transfers its energy to the photon, that is where the somewhat misleading name inverse Compton scattering comes from (no other process is happening). There exist also two cases in this limit, depending on the energy of the photon in the rest frame of the electron. For $\gamma x \ll 1$, the process can be treated in the same way as in the classical Thomson case in the electron's rest frame. However, through the relativistic aberration through the boost the focus and the photon energy in a lab frame can significantly change from the non-relativistic results. This is called the inverse Compton scattering in the Thomson regime. Increasing the photon energy even further, the cross section starts to deviate from the classical formula and quantum effects come into play. For $\gamma x \gg 1$ the cross section in the electron's rest frame is given by the Klein-Nishina formula. Therefore, this regime is called inverse Compton scattering in the Klein-Nishina regime.

Following the structure of [Mastichiadis and Kirk \(1995\)](#), the treatment of inverse Compton scattering will be done in these two relativistic regimes. Due to its close similarity to the synchrotron radiation, also the Thomson regime can be approximated as a continuous energy loss. In contrast to that, in the Klein-Nishina regime the electrons loose a significant fraction of their energy to the photon. Thus the derivation of the electron-loss as well as photon-gain terms starts from the general formula for the spectrum produced by a relativistic electron, which was first calculated by [Jones \(1968\)](#) and nicely summarised by [Blumenthal and Gould \(1970\)](#):

$$\eta_{\text{IC, full}}(\gamma, x_{\text{in}}, x) = \frac{3}{4} \frac{1}{\gamma^2 x_{\text{in}}} f_{\text{IC, full}}(q, \Gamma_e) \quad (4.42)$$

$$\text{with } \Gamma_e(\gamma, x_{\text{in}}) = 4\gamma x_{\text{in}} \quad \text{and} \quad q(\gamma, x_{\text{in}}, x) = \frac{x}{4\gamma^2 x_{\text{in}}(1 - x/\gamma)} \quad (4.43)$$

$$\text{and } f_{\text{IC, full}}(q, \Gamma_e) = 2q \ln q + (1 + 2q)(1 - q) + \frac{1}{2} \frac{(\Gamma_e q)^2}{1 + \Gamma_e q}(1 - q) \quad (4.44)$$

This function has then to be weighted with the incoming electron and photon distributions, which results in:

$$Q_{\text{IC, full}}^\gamma(x, \tau) = \frac{3}{4} \int_1^\infty \frac{d\gamma}{\gamma^2} n_e(x, \tau) \int_{\frac{1}{4\gamma^2} \leq q \leq 1} \frac{dx_{\text{in}}}{x_{\text{in}}} n_\gamma(x_{\text{in}}, \tau) f_{\text{IC, full}}(q, \Gamma_e) \quad (4.45)$$

$$(4.46)$$

It is then in principle possible to determine the energy losses of the electrons from the same integral by rewriting $\eta_{\text{IC, full}}$ in terms of the outgoing electron energy instead of x using energy conservation. However, this integration is rather complex and computationally expensive such that the discussion is split up into two approximations for each

of the regimes. This yields for the electron losses:

$$\frac{\partial n_e}{\partial t} \Big|_{IC}(\gamma, t) = \int_1^\infty d\gamma_{in} n_e(\gamma_{in}, t) \int_0^\infty dx_{in} n_\gamma(x_{in}, t) \eta_{IC}(\gamma_{in}, x_{in}, \gamma) \quad (4.47)$$

$$= \underbrace{\iint_{\gamma_{in}x_{in} < 1} d\gamma_{in} n_e(\gamma_{in}, t) dx_{in} n_\gamma(x_{in}, t) \eta_{IC}(\gamma_{in}, x_{in}, x)}_a + \quad (4.48)$$

$$\underbrace{\iint_{\gamma_{in}x_{in} \geq 1} d\gamma_{in} n_e(\gamma_{in}, t) dx_{in} n_\gamma(x_{in}, t) \eta_{IC}(\gamma_{in}, x_{in}, \gamma)}_b \quad (4.49)$$

For the photons it looks very similar:

$$\frac{\partial n_e}{\partial t} \Big|_{IC}(x, t) = \int_1^\infty d\gamma_{in} n_e(\gamma_{in}, t) \int_0^\infty dx_{in} n_\gamma(x_{in}, t) \eta_{IC}(\gamma_{in}, x_{in}, x) \quad (4.50)$$

$$= \underbrace{\iint_{\gamma_{in}x_{in} < 1} d\gamma_{in} n_e(\gamma_{in}, t) dx_{in} n_\gamma(x_{in}, t) \eta_{IC}(\gamma_{in}, x_{in}, x)}_c + \quad (4.51)$$

$$\underbrace{\iint_{\gamma_{in}x_{in} \geq 1} d\gamma_{in} n_e(\gamma_{in}, t) dx_{in} n_\gamma(x_{in}, t) \eta_{IC}(\gamma_{in}, x_{in}, x)}_d \quad (4.52)$$

Thomson Regime

In the Thomson regime the electrons loose only a small fraction of their energy. Calculating the energy loss rate in the ultra-relativistic limit $\beta \approx 1$, a result remarkably close to the synchrotron case is obtained:

$$b_{IC,T}(\gamma) = \int_0^\infty dx x \eta(x) = \frac{4}{3} \underbrace{\frac{\sigma_T L}{m_e c^2} U_T(\gamma)}_{l_{IC,T}} \gamma^2 \quad (4.53)$$

In contrast to a constant magnetic field, this time the compactness becomes a function of the electron energy, since only photons up to a limiting energy of the Thomson regime contribute to the relevant energy density U_T of the radiation field:

$$l_{IC,T}(\gamma) = \int_0^{x_T} dx x n_\gamma(x) \quad \text{with} \quad x_T = \frac{3}{4\gamma} \quad (4.54)$$

The upper limit of the integration is motivated by the fact that a photon with initial energy x_T will be on average scattered up to an energy of $x = 1$ in the rest frame of the electron.

In the same manner as for the synchrotron losses, also the relative electron energy losses

due to inverse Compton scattering can be assumed to be small. Thus, the first term (a) can be modelled in a continuous way:

$$\left. \frac{\partial n_e}{\partial \tau} \right|_{IC,T}(x, \tau) = \frac{d}{d\gamma} [b_{IC,T}(\gamma) n(\gamma, \tau)] = \frac{4}{3} \frac{d}{d\gamma} [l_{IC,T}(\gamma) \gamma^2] \quad (4.55)$$

The dependency of $l_{IC,T}$ on the electron energy γ is however neglected in [Mastichiadis and Kirk \(1995\)](#). In analogy to the synchrotron case, a similar δ -approximation is made in this case to reduce the 2D-integral from the full photon gain term:

$$\eta_{T,\delta}(x_{in}, x_{out}, \gamma) = q \delta(x_{out} - \langle x \rangle) \quad \text{with} \quad \langle x \rangle = \frac{4}{3} \gamma^2 x_{in} \quad (4.56)$$

Here the assumption is made that the photons scatter of always only at the mean energy $\langle x \rangle$. The normalisation q can then be determined by a comparison to the total energy loss rate:

$$\int_0^\infty dx_{out} x_{out} \int_0^{x_T} dx_{in} n_\gamma(x_{in}) \eta_{T,\delta}(x_{in}, x_{out}, \gamma) \stackrel{!}{=} b_{IC,T}(\gamma) \quad (4.57)$$

$$\Leftrightarrow q \int_0^{x_T} dx_{in} \frac{4}{3} \gamma^2 x_{in} n_\gamma(x_{in}) \stackrel{!}{=} \frac{4}{3} l_{IC,T} \gamma^2 \quad (4.58)$$

$$\Leftrightarrow q = 1 \quad (4.59)$$

This yields:

$$\eta_{\delta,T}(x_{in}, x_{out}, \gamma) = \delta\left(x_{out} - \frac{4}{3} \gamma^2 x_{in}\right) \quad (4.60)$$

and the source term for the photons (c) becomes then:

$$Q_{IC,T}^\gamma(x, \tau) = \int_1^\infty d\gamma n_e(\gamma, \tau) \int_0^{x_T} dx_{in} n_\gamma(x_{in}, \tau) \delta\left(x_{out} - \frac{4}{3} \gamma^2 x_{in}\right) \quad (4.61)$$

$$= \frac{\sqrt{3}}{4} \int_0^{\min(3/4x, 3x/4)} \frac{dx_{in}}{\sqrt{x x_{in}}} n_\gamma(x_{in}, \tau) n_e\left(\sqrt{\frac{3x}{4x_{in}}}, \tau\right) \quad (4.62)$$

The upper limit of this integral can be understood by looking at fig. 4.6. It shows the path along which the integral is calculated. The expression with the minimum comes in due to the fact that two conditions have to be fulfilled, $\gamma \geq 1$ and that the mean energy of the photon in the electron rest frame is still in the Thomson regime:

$$\gamma \geq 1 \quad \Rightarrow \quad \gamma^2 = \frac{3x}{4x_{in}} \geq 1 \quad \Rightarrow \quad x_{in} \leq \frac{3x}{4} \quad (4.63)$$

$$\frac{4}{3} x_{in} \gamma \leq 1 \quad \Rightarrow \quad x_{in} \leq \frac{3}{4x} \quad (4.64)$$

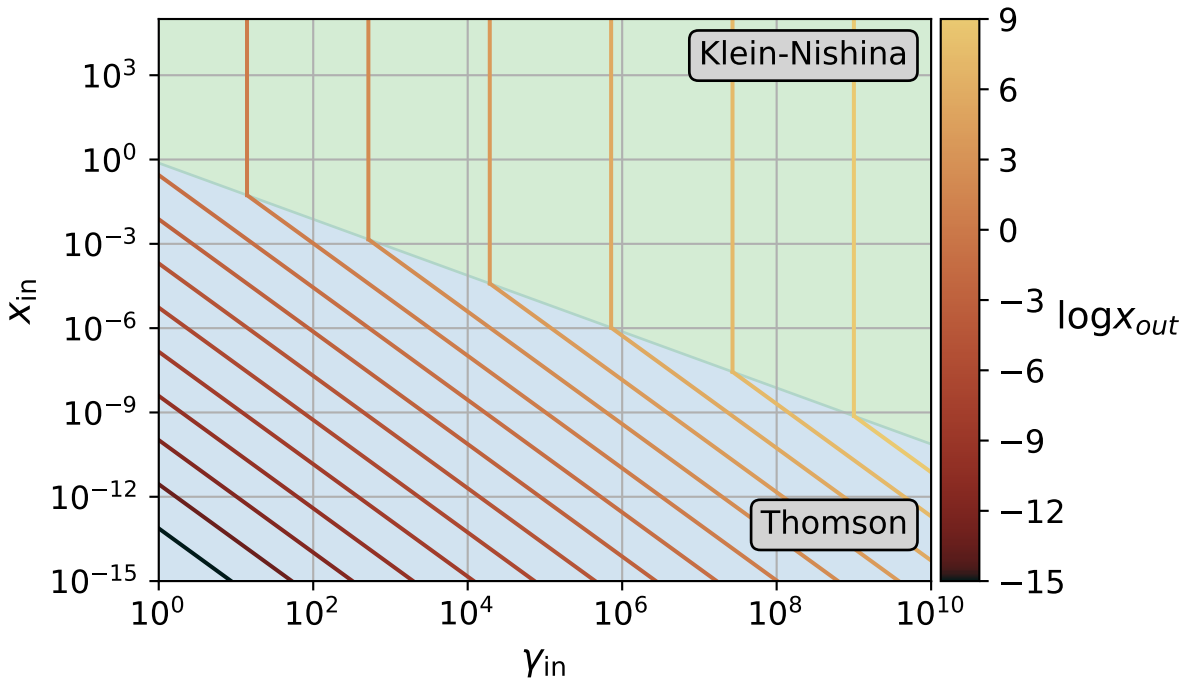


Figure 4.6.: Parameter space for the integral of the source term for the photons for inverse Compton scattering. The lower blue area corresponds to the parameter space, where scattering happens in the Thomson regime ($3\gamma x/4 < 1$), while the upper part belongs to the Klein-Nishina regime. Remember that the parameter space does not extend to the left ($\gamma \geq 1$ always) and that the approximation of relativistic electrons breaks down for $\gamma \rightarrow 1$. The solid lines correspond to the paths following from the two δ -approximations as introduced by [Mastichiadis and Kirk \(1995\)](#), where the colour denotes the outgoing photon energy: In the Thomson regime this corresponds to the assumption that the photon is always scattered to the mean energy: $x_{\text{out}} = \frac{4}{3}\gamma^2 x_{\text{in}}$. In case of the Klein-Nishina regime the out-coming photon energy is approximated by the incoming electron energy $x_{\text{out}} = \gamma$.

Klein-Nishina Regime

For the Klein-Nishina regime the cross section deviates from the constant σ_T in Thomson regime. This can be approximated by $\sigma = \sigma_T / \gamma x_{\text{in}}$ in the limit of $\gamma \gg 1$ ([Longair 2011](#)). Since in contrast to the Thomson limit the energies losses of an electron are significant, the continuous limit can not be taken here. Instead, another δ -approximation is made ([Mastichiadis and Kirk 1995](#)):

$$\eta_{\text{KN},\delta}(x_{\text{in}}, x_{\text{out}}, \gamma) = \frac{1}{\gamma x_{\text{in}}} \delta(x_{\text{out}} - \gamma) \quad (4.65)$$

This is obtained by assuming that all the electron energy is transferred to the photon and the additional factors of $1/\gamma x_{\text{in}}$ arise due to the different cross section. With this, the electron losses (b) and photon gains (d) can be calculated straightforward by convo-

lution with the incoming photon and electron fields:

$$Q_{\text{IC,KN}}^\gamma(x, \tau) = n_e(x, \tau) \int_{3/4x}^{\infty} \frac{dx_{\text{in}}}{xx_{\text{in}}} n_\gamma(x_{\text{in}}, \tau) \quad (4.66)$$

$$L_{\text{IC,KN}}^e(\gamma, \tau) = \frac{n_e(\gamma, \tau)}{\gamma} \int_{x_T}^{\infty} \frac{dx_{\text{in}}}{x_{\text{in}}} n_\gamma(x_{\text{in}}, \tau) \quad (4.67)$$

The paths of the integration depending on the out-going photon energy are also added to fig. 4.6. This time, $\gamma \geq 1$ is simply ensured by the fact that $\gamma \geq 1$ and $n_e(\gamma < 1, \tau) = 0$.

On the Origin of the Incoming Radiation Field

The radiation field, that is scattered up, can originate from either an external field (EC) or it can be the radiation field produced by the population of electrons itself via synchrotron radiation or previous inverse Compton scattering (SSC). Typical external radiation fields in astrophysical surroundings are for example the cosmic microwave background (Sunyaev–Zel'dovich effect) or thermal radiation emitted by its components, like the BLR in the case of an AGN.

Inverse Compton Scattering for a Power Law on a Black Body

One important application and crosscheck of the above formulae, which can be given by analytical approximations, is the inverse Compton scattering for a power-law electron distribution ($n_e(\gamma) = K\gamma^{-p}$) and a black-body photon distribution (see eq. (4.22)). The derivation of these expressions is given in [Blumenthal and Gould \(1970\)](#) and yields for the two regimes:

$$\left. \frac{\partial^2 n}{\partial \tau \partial x} \right|_{\text{Thomson}} = 3\pi \frac{m_e^3 c^3}{h^3} \sigma_T L K F(-\Gamma) \Theta^{(p+5)/2} x^{-(p+1)/2} \quad (4.68)$$

$$\left. \frac{\partial^2 n}{\partial \tau \partial x} \right|_{\text{Klein-Nishina}} = \frac{\pi^3}{2} \frac{m_e^3 c^3}{h^3} \sigma_T L K \Theta^2 x^{-(p+1)} (\ln x\Theta + 1 + C(-\Gamma) - C_E - C_l) \quad (4.69)$$

where $C_E = 0.5772$ is Euler's constant, $C_l = 0.57$ and the function $C(p)$ from [Blumenthal and Gould \(1970\)](#) can be approximated to -1 for $p = 2$. Of particular interest is the fact that the spectral index in both regimes can be determined by the one from the electron distribution: $-(p+1)/2$ in case of the Thomson regime and $-(p+1)$ in the Klein-Nishina regime if the logarithmic dependency is neglected.

4.5.3. Pair Production

The process of pair production denotes the annihilation of a pair of photons leading to a new electron-positron pair: $\gamma + \gamma \rightarrow e^+ + e^-$. To ensure momentum conservation, two photons are needed and energy conservation requires the centre-of-mass energy of the reaction which is equal to the energy of both photons together to be higher than twice the rest-mass energy of the electron. The derivation of the reaction rate is summarised in [Coppi and R. D. Blandford \(1990\)](#) and can be approximated as a function of the product

of both incoming photon energies:

$$R_{\gamma\gamma}(\omega) = 0.652 \frac{\omega^2 - 1}{\omega^3} \ln(\omega) \Theta(\omega - 1) \quad (4.70)$$

Following [Mastichiadis and Kirk \(1995\)](#) this yields the electron source and photon loss:

$$Q_{\gamma\gamma}^e(\gamma, \tau) = 4n_\gamma(2\gamma, \tau) \int_0^\infty dx' n_\gamma(x', \tau) R_{\gamma\gamma}(2\gamma x') \quad (4.71)$$

$$L_{\gamma\gamma}^\gamma(x, \tau) = n_\gamma(x, \tau) \int_0^\infty dx' n_\gamma(x', \tau) R_{\gamma\gamma}(xx') \quad (4.72)$$

4.6. Numerical Solving of the Equations

Summarising the preceding sections, for the radiation modelling the following two coupled partial differential equations need to be solved simultaneously:

$$\frac{\partial n_e}{\partial \tau} = Q_{\text{inj}}^e + Q_{\gamma\gamma}^e - L_{\text{syn}}^e - L_{\text{IC}}^e \quad (4.73)$$

$$\frac{\partial n_\gamma}{\partial \tau} = -\frac{n_\gamma}{\tau_{\text{esc}}} + Q_{\text{syn}}^\gamma + Q_{\text{IC}}^\gamma - L_{\gamma\gamma}^\gamma - L_{\text{ssa}}^\gamma \quad (4.74)$$

Here $n_x = \frac{dN_x}{dVdE} \cdot \sigma_T L m_e c^2$ are the spectral and spatial number densities of electron/-positron pairs or photons, which are normalised to the *Thomson volume* $\sigma_T L$ with the layer length L and thus the numbers in this volume. All the terms on the right hand side denote source (Q_x) and loss (L_x) terms. Time t is normalised to the light crossing time c/L referring to the layer's length.

Discretisation

The two number densities n_e and n_γ are both functions of the time and the energy of the particles. To solve these equations numerically, they have to be discretised. A linear grid is chosen for time, while for the energies a grid with equidistant steps in the logarithm of the energy is used. This enables the investigation of the physical processes happening on energy scales varying over several orders of magnitude. The two equations, that will be solved simultaneously, differ by two facts: First, the electron equation is basically an advection equation, while the photon equation is in general more complex. Second, the photon equation contains terms proportional to the integral over the photon number density, which makes it an integro-differential equation.

To solve the electron equation, an implicit scheme from [Chang and Cooper \(1970\)](#) is used. They presented a method to solve a diffusion equation, such that the total number of particles is conserved and the number density always remains positive. This is achieved by a dedicated discretisation of the advection and diffusion term. Since there is no diffusion term in this context, the limit of zero diffusion will be used.

Following the ideas of Chang and Cooper, for the time a simple forward differenced scheme and for the energy a center differenced scheme is used. Looking at a general advection-diffusion-equation, a generalised flux $F(t, E)$ can be defined:

$$\frac{\partial N(t, E)}{\partial t} = S(t, E) + A(t, E)N(t, E) + \underbrace{\frac{\partial}{\partial E} \left[B(t, E)N(t, E) + C(t, E)\frac{\partial}{\partial E}N(t, E) \right]}_{F(t, E)} \quad (4.75)$$

The discretised form of eq. (4.75) is then using the short notation $N_j^n = N(n \cdot \Delta t, j \cdot \Delta E)$:

$$\frac{N_j^{n+1} - N_j^n}{\Delta t} = S_j^n + A_j^n N_j^{n+1} + \frac{F_{j+1/2}^{n+1} - F_{j-1/2}^{n+1}}{\Delta E} \quad (4.76)$$

Chang and Cooper showed now for $S = 0$ and $A = 0$ that to make sure that the total number over all energies is conserved and to ensure $N \geq 0$, the definition of F at half-energy steps has to be done as follows:

$$F_{j\pm 1/2}^{n+1} = B_{j\pm 1/2}^n N_{j\pm 1/2}^{n+1} + C_{j\pm 1/2}^n \begin{cases} \frac{N_{j+1}^{n+1} - N_j^{n+1}}{\Delta E} \\ \frac{N_j^{n+1} - N_{j-1}^{n+1}}{\Delta E} \end{cases} \quad (4.77)$$

The important part is hereby the choice of $N_{j\pm 1/2} = (1 - \delta_j)N_{j+1} + \delta_j N_j$ at half-energy steps:

$$w_j = \Delta E \frac{B_j}{C_j} \quad (4.78)$$

$$\delta_j = \frac{1}{w_j} - \frac{1}{e^{w_j} - 1} \quad (4.79)$$

In the simple case that there is no diffusion term, one can take the limit of $C \searrow 0$:

$$\lim_{C \searrow 0} \delta_j = 0 \quad (4.80)$$

This implies $N_{j+1/2} = N_{j+1}$ and $N_{j-1/2} = N_j$. This yields a system of equations of the form:

$$v_{2,j} N_j^{n+1} + v_{3,j} N_{j+1}^{n+1} = Q_j^n \quad (4.81)$$

which corresponds to a banded matrix and can be solved, using the initial conditions $b_J = 0$, where J indexes the last energy bin:

$$MN^{n+1} = Q \quad (4.82)$$

with

$$M = \begin{pmatrix} v_{2,0} & v_{3,0} & 0 & \dots & 0 \\ 0 & v_{2,1} & v_{3,1} & \dots & 0 \\ \vdots & \vdots & \ddots & \ddots & 0 \\ 0 & 0 & 0 & v_{2,J-1} & v_{3,J-1} \\ 0 & 0 & 0 & 0 & v_{2,J} \end{pmatrix}, \quad Q = \begin{pmatrix} \Delta t S_0^n + N_0^n \\ \vdots \\ \Delta t S_J^n + N_J^n \end{pmatrix} \quad (4.83)$$

Using the results of section 4.5, the full electron equation is given by and the terms can be identified:

$$\frac{\partial n_e}{\partial t} = \underbrace{\frac{\partial}{\partial \gamma} \left[\frac{4}{3} (l_B + U_T(\gamma)) \gamma^2 n_e(\gamma) \right]}_{B(\gamma)} + \underbrace{n_e(\gamma) \int_{\frac{3}{4\gamma}}^{\infty} \frac{n_\gamma(x')}{x' \gamma} dx'}_{A(\gamma)} + \underbrace{4n_\gamma(2\gamma) \int_0^{\infty} dx' n_\gamma(x') R_{\gamma\gamma}(2\gamma x')}_{S(\gamma)} \quad (4.84)$$

Then the tridiagonal matrix equation 4.82 can be solved.

The discretisation of the photon equation is different from the electron equation due to two aspects: It contains no advection term, which simplifies the problem significantly. Furthermore, it is an integro-differential equation, since the source and loss terms contain integrals depending also on n_γ . However, the approximation is made that the integrals vary only negligibly in one time step and the value of the last time step is used to calculate the integral.

Then the structure of the photon equation becomes significantly simpler:

$$\frac{\partial N(t, E)}{\partial t} = S(t, E) + A(t, E)N(t, E). \quad (4.85)$$

Similar to eq. (4.76) this is discretised to:

$$\frac{N_j^{n+1} - N_j^n}{\Delta t} = S_j^n + A_j^n N_j^{n+1}, \quad (4.86)$$

which can be simply solved:

$$N_j^{n+1} = \frac{\Delta t S_j^n + N_j^n}{1 - \Delta t A_j^n}. \quad (4.87)$$

Then, the terms can be identified to:

$$\begin{aligned} S_j^n &= \frac{2}{3} \frac{l_B}{\sqrt{b^3 x_j}} n_e \left(\sqrt{\frac{x_j}{b}}, t^n \right) \\ &\quad + \frac{\sqrt{4}}{3} \int_0^{\min(\frac{3x_j}{4}, \frac{3}{4x_j})} \frac{dx'}{\sqrt{x_j x'}} n_e \left(\sqrt{\frac{3x_j}{4x'}}, t^n \right) \\ &\quad + \frac{n_e(x_j, t^n)}{x_j} \int_{\frac{3}{4x_j}}^{\infty} \frac{dx'}{x'} n_\gamma(x', t^n) \end{aligned} \quad (4.88)$$

and

$$\begin{aligned} A_j^n &= -\frac{1}{t_{\text{esc}}} \\ &\quad - n_\gamma(x_j, t^n) \int_0^\infty dx' n_\gamma(x', t^n) R_{\gamma\gamma}(x_j x') \\ &\quad + \frac{R}{L} \alpha(x_j) n_\gamma(x_j, t^n) \end{aligned} \quad (4.89)$$

Integrals, Derivatives and Interpolation

For the calculation of derivatives the numpy implementation is used². It uses second order accurate central differences in the interior points and first order accurate one-sided (forward or backwards) differences at the boundaries. For the numerical evaluation of the integrals of the terms the scipy implementation of Simpson's rule is used³. However, the accuracy could be improved significantly by solving the integrals after performing a substitution to logarithmic variables. The number of used grid points is chosen to be 500, which is a trade-off between computation time and accuracy. In order to evaluate the number densities at arbitrary energies, the values at the grid are interpolated linearly⁴. Values out of the grid are not extrapolated but simply set to 0.

Grid and Boundary Conditions

The boundaries of the problem can be estimated from the physical processes. Since no acceleration processes for electrons take place, $\gamma \in [1, \gamma_{\text{inj,max}}]$ with the maximum energy $\gamma_{\text{inj,max}}$ of injection. For the photons, the spectrum consists of basically two humps. The lower synchrotron hump defines the minimum energy from the δ -approximation $x_{\text{min}} = \hat{b}\gamma^2 = \hat{b}$ and the upper inverse Compton hump defines the maximum energy based on the highest electron energy, again using the δ -approximation: $x_{\text{max}} = \gamma_{\text{max}}$. To avoid numerical issues and boundary effects, the energy range is always chosen at least one order of magnitude lower⁵/higher.

²<https://docs.scipy.org/doc/numpy/reference/generated/numpy.gradient.html>

³<https://docs.scipy.org/doc/scipy/reference/integrate.html>

⁴<https://docs.scipy.org/doc/scipy/reference/interpolate.html>

⁵Except for the lower limit of $\gamma_{\text{min}} = 1$

Since the energies vary over orders of magnitude, a grid with a uniform binning in logarithmic energies is chosen. This can be parameterised by the minimum and maximum exponent $\eta_{\min/\max} = \log_{10} E_{\min/\max}$ and the total number of grid points N :

$$E_i = 10^{i \cdot (\eta_{\max} - \eta_{\min}) / (N-1) + \eta_{\min}} \quad (4.90)$$

Infinitesimal energies are then approximated by the difference between half steps:

$$dE_i = E_{i+1/2} - E_{i-1/2} = 2E \sinh \left(\frac{\ln 10}{2(N-1)} \log \left(\frac{E_{\max}}{E_{\min}} \right) \right) \quad (4.91)$$

The choice of the number of grid points is again a trade-off between speed and accuracy. Since the algorithm for the electron equation is of implicit nature, the Courant criterion can not be used to determine a proper value up to which the solver stays stable. For the time a linear binning is chosen. As a width of the time step a value of $d\tau = 10^{-3}$ has been found to yield results with negligible differences to finer grids. At the beginning of a simulation both number densities are chosen to be 0 at all energies. Out of the simulated range, the boundary conditions are also chosen to a vanishing number density.

4.7. Synchrotron Radiation for a Power Law

As a crosscheck of the code, at first some situations are investigated, where the solution is known analytically. Thereby the accuracy of the code can be checked. As an additional validation it is compared to the results of the code from the Bachelor's thesis of [Schwefer \(2019\)](#).

The first cross check performed is to look at a fixed electron spectrum and consider only the effects of synchrotron radiation, synchrotron self-absorption and losses at the boundaries of the system. The electron spectrum is chosen to be a power law with slope $-p$ and normalisation K . Mathematically this means:

$$\frac{\partial n_e}{\partial \tau} = 0 \quad n_e(\gamma) = K\gamma^{-p} \quad \text{for all times} \quad (4.92)$$

$$\frac{\partial n_\gamma}{\partial \tau} = Q_{\text{syn}}^\gamma - L_{\text{ssa}}^\gamma - L_{\text{esc}}^\gamma \quad n_\gamma(\tau = 0) = 0 \quad (4.93)$$

The escape term is given by $L_{\text{esc}}^\gamma = n_\gamma / L$ and also for the self-absorption term the length scale is chosen to be the size of the reconnection layer. An exemplary value of $B = 1 \text{ G}$ is used. The evolution of the electron and photon spectral number densities is given in fig. 4.7 on the left and right. The electron spectrum is enforced to be a power law with the injected spectral index of $-p = -2$ (flat in this plot). For the photon spectrum, it can be clearly seen that from early times (light blue) to late times (dark green) a steady state evolves. This consists effectively of two regions: An optical thick region dominated by self-absorption at low energies and an optical thin region dominated by the power law behaviour of the electron spectrum at low energies. As expected from section 4.5.1 also

the spectral indices show a value of 1.5 in the regime of significant SSA and a value of $-(p + 1)/2 = -1.5$ for higher energies. It can be furthermore seen that the minimal and maximal energies follow from the δ -approximation: $x_{\min/\max} = \hat{b}\gamma_{\min/\max}^2$. For $\gamma_{\min} = 10$ this yields $x_{\min} \approx 2 \cdot 10^{-12}$ and for $\gamma_{\min} = 1 \cdot 10^4$ one obtains $x_{\min} \approx 2 \cdot 10^{-6}$.

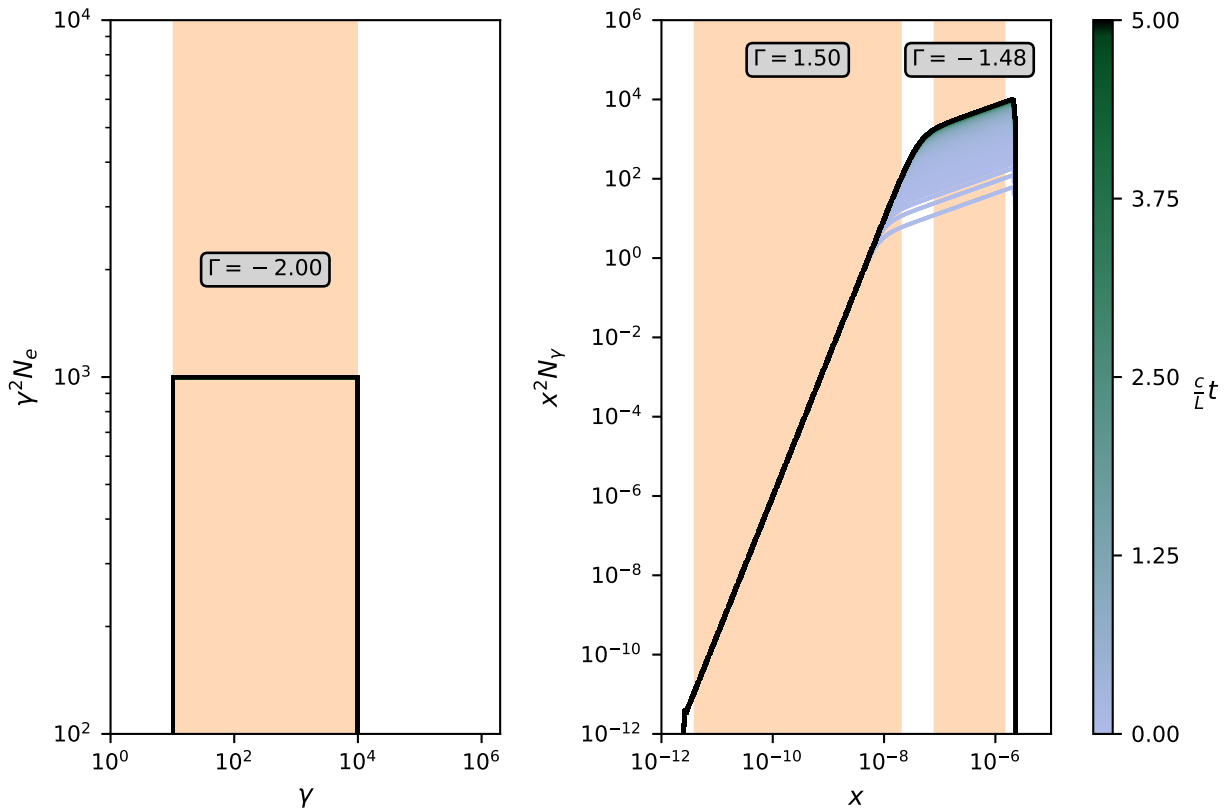


Figure 4.7.: Electron (left) and photon (right) spectrum for a fixed power law electron spectrum and only synchrotron radiation, synchrotron self-absorption and losses due to escape. For both terms the system size is chosen to a length of the reconnection layer $L = 5 \cdot 10^{16}$ cm and a magnetic field $B = 1$ G as representative values. Colour encodes the temporal evolution from light blue to dark green. In the orange marked energy ranges a power law fit has been performed and the spectral index of n_e is given in the box.

In fig. 4.8 the photon spectrum is compared to the code from Schwefer (2019) denoted by the index GS. The implementation of both codes is very similar, except for the fact that this code uses just simple linear difference quotient (Newton's method) for the calculation of the derivatives. This leads to a difference in the SSA-regime, as this code is based on a second-order accurate differencing scheme. In the optically thin regime both codes show consistent results during the steady state, although for early times slight differences can be observed. Furthermore, two humps in the optically thick regime can be seen at about $3 \cdot 10^{-11}$ and $8 \cdot 10^{-10}$, which indicate some systematic effect that probably also originates from the difference in the numerical schemes.

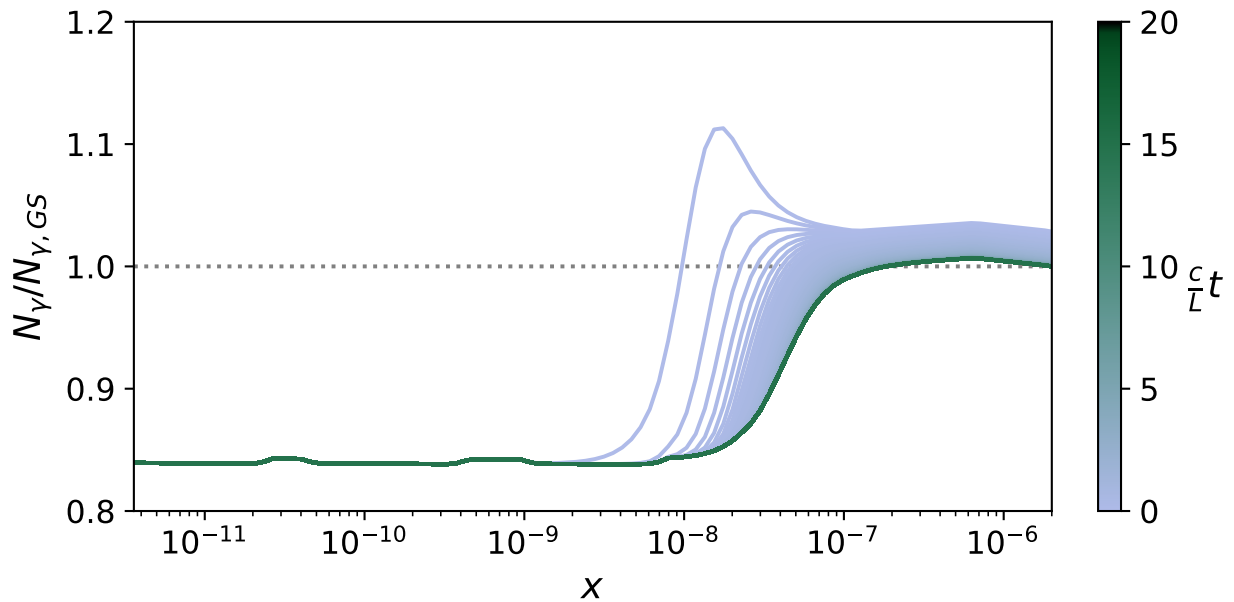


Figure 4.8.: Comparison of this code to the one obtained by [Schwefer \(2019\)](#) for the same parameters as in fig. 4.7.

4.8. Synchrotron in Steady State

As a next cross check the electron spectrum is no longer fixed as in the previous chapter, but a constant power-law is continuously injected. This is parameterised by the following system of coupled equations:

$$\frac{\partial n_e}{\partial \tau} = K\gamma^{-p} - L_{\text{syn}}^e \quad n_e(\gamma, \tau = 0) = 0 \quad (4.94)$$

$$\frac{\partial n_\gamma}{\partial \tau} = Q_{\text{syn}}^\gamma - L_{\text{ssa}}^\gamma - L_{\text{esc}}^\gamma \quad n_\gamma(x, \tau = 0) = 0 \quad (4.95)$$

The escape term is given again by $L_{\text{esc}}^\gamma = n_\gamma / L$ and also for the self-absorption term the length scale is chosen to be the size of the reconnection layer. An exemplary value of $B = 1 \text{ G}$ is used. The evolution of the electron and photon spectral number densities is given in fig. 4.9 on the left and right. The electron injection spectrum is enforced to be a power law with the injected spectral index of $-p = -2$ (flat in this plot).

When looking at the solution of the electron spectrum, two spectral ranges with a breaking point decreasing in time can be identified. This fits to the numerical expectation from [Kardashev \(1962\)](#), which predicts the break position at (compare also [Mastichiadis and Kirk \(1995\)](#)):

$$\gamma_{\text{br}} = \frac{\gamma_{\text{max}}}{1 + \frac{4}{3}l_B\gamma_{\text{max}}\tau} \quad (4.96)$$

For the earliest (lowest) line this yields $\gamma_{\text{br}} \approx 1.5 \cdot 10^5$ and for the latest curve during steady state $\gamma_{\text{br}} \approx 156$, which is in good agreement with the obtained results. Furthermore, the spectral indices for both regimes are predicted by [Kardashev \(1962\)](#) to be

approximately $-p$ before and $-p - 1$ after the breaking point. The fitted spectral indices show exactly this behaviour.

Looking at the photon spectrum also two regimes are visible, again an optically thick one with a spectral index of 1.5 for lower energies and an optically thin one for the upper range of the spectrum, where the spectral index is as expected $-(a + 1)/2 = -2$, since the electron spectrum changes to the softer index $a = (p + 1) = 3$ in this range. Furthermore, it can be seen that for early times another spectral component is visible, whose breaking point is drifting towards lower energies with time. This is exactly the break of the electron spectrum and the spectrum before resembles exactly the synchrotron radiation of the electron spectrum before the break with a spectral index of $-(p + 1)/2 = -1.5$.

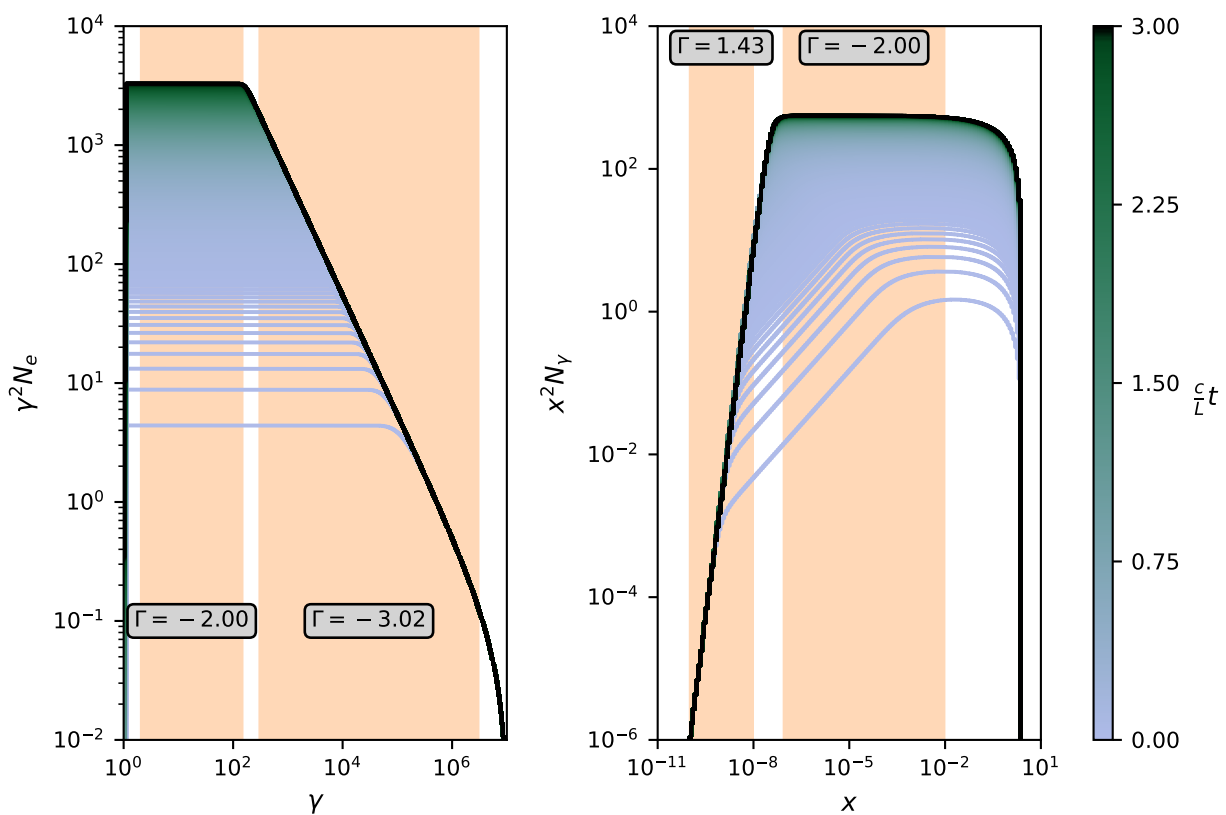


Figure 4.9.: Electron (left) and photon (right) spectrum for a fixed power law electron spectrum and only synchrotron radiation, synchrotron self-absorption and losses at the boundaries. For both terms the system size is chosen to the length of the reconnection layer $L = 5 \cdot 10^{16}$ cm and a magnetic field $B = 1$ G. Colour encodes the temporal evolution from blue to dark green. In the orange marked energy ranges a power law fit has been performed and the spectral index of n_e is given in the box.

Figure 4.10 shows analogue to fig. 4.8 a comparison of this code to the one from [Schwefer \(2019\)](#). At first one can see that again the optically thick regime is about 20 % below, while the effect is opposite this time for the optical thin regime. This is thought to originate from

the improved calculation of integrals and gradients as well as the finer resolution of the energy grid. It is also thought that this is the reason for the small oscillatory behaviour, which is only visible in the code from [Schwefer \(2019\)](#). The origin of the additional feature around $1 \cdot 10^{-8}$ and the difference is unclear and has to be further investigated.

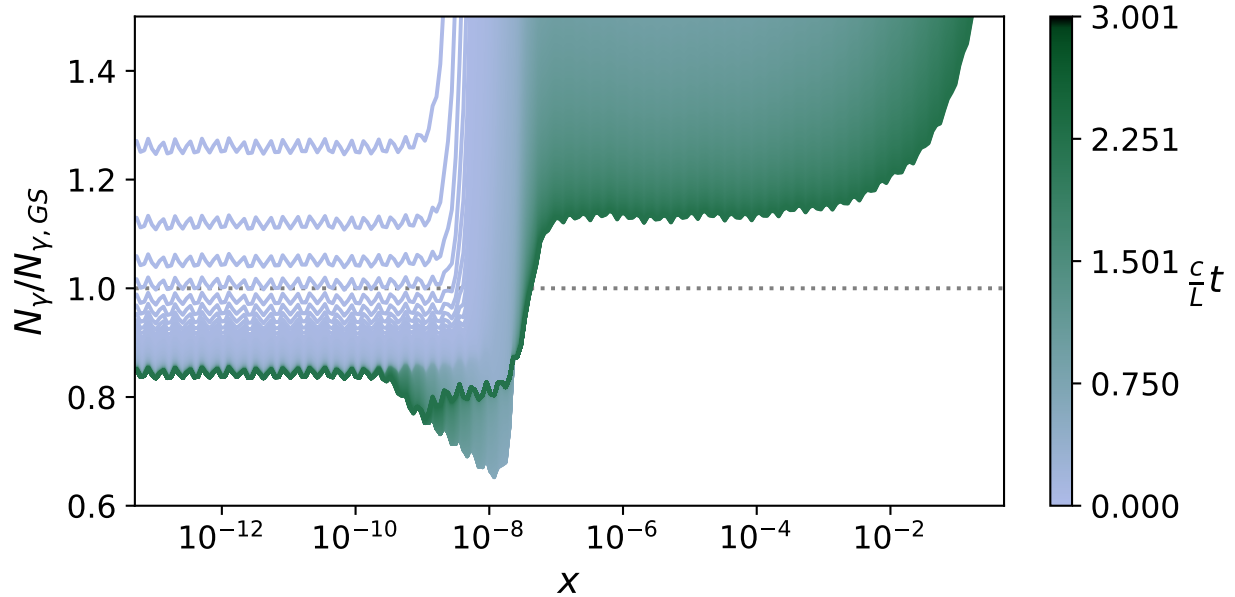


Figure 4.10.: Comparison of this code to the one obtained by [Schwefer \(2019\)](#) for the same parameters as in fig. 4.9.

4.9. Inverse Compton Scattering on a Black Body for a Power Law

To check the implementation of the inverse Compton scattering, two cross checks are performed. In this section a fixed power-law electron spectrum and a black body are investigated, while in the next section a source term for the electron population and a photon-escape term are included. The first check corresponds basically to just comparing the two source terms from the δ -approximation of [Mastichiadis and Kirk \(1995\)](#) to the full integral from eq. (4.42) and its approximations eq. (4.68) and eq. (4.69). A representative value of $\Theta = 1 \cdot 10^{-5}$ is chosen and the electrons are injected with energies between $\gamma_{\min} = 10$ and $\gamma_{\max} = 1 \cdot 10^{10}$ to allow for a significant Klein-Nishina regime. The results can be seen in fig. 4.11. The two dotted lines show the photon source term in the Thomson (blue) and Klein-Nishina (green) regime, which sum up to the red curve. Comparing the sum of both terms now to the full 2D-integral from [Blumenthal and Gould \(1970\)](#) and its approximation in the Thomson regime, a good agreement can be found in the range of $10^{-4} \leq \gamma \leq 10^4$. In contrast to that, it can be seen that a kink compared to the full integral occurs in the transition of the two regimes. This is important to keep in mind for the interpretation of later results, since this kink is expected to be

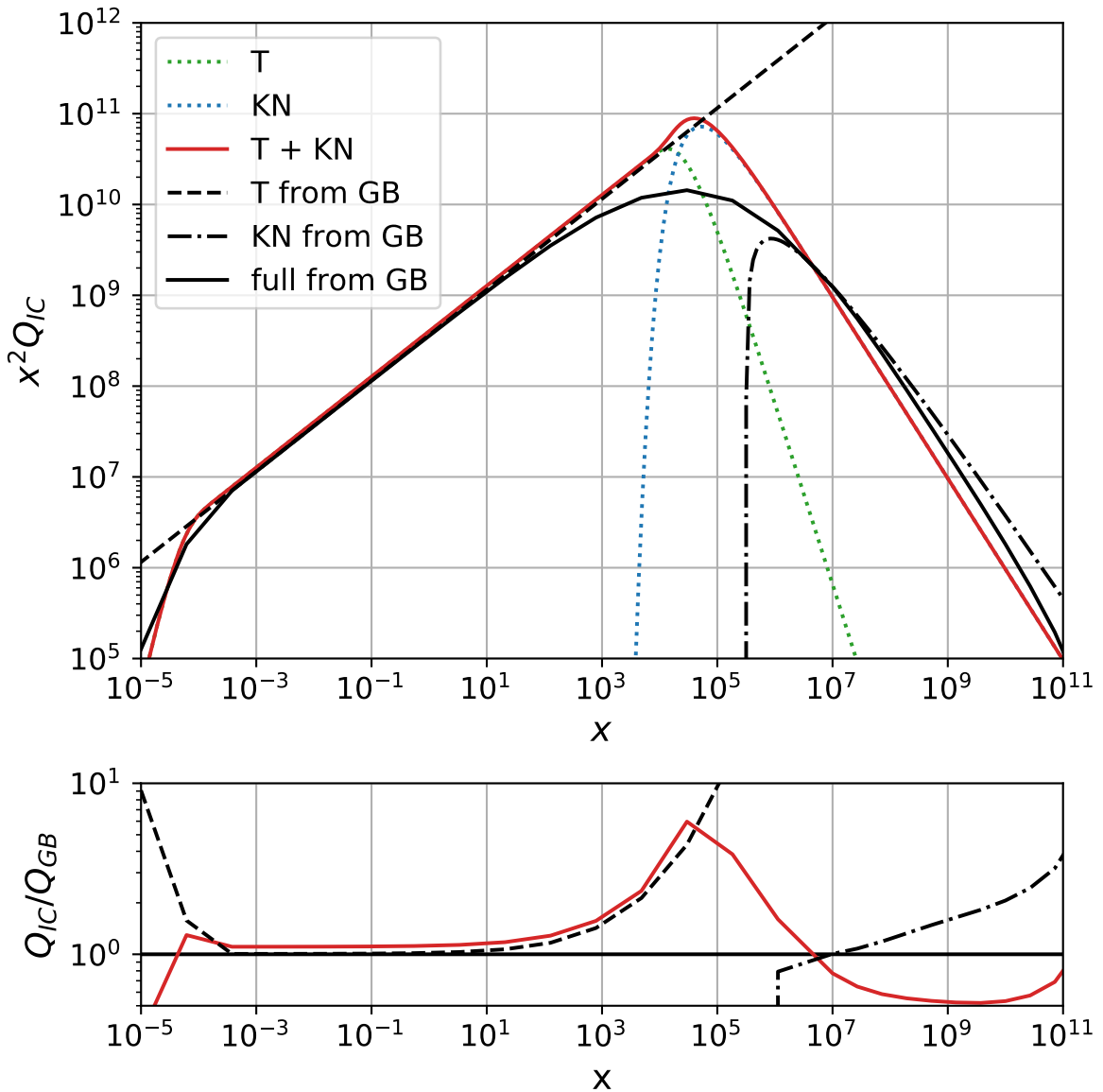


Figure 4.11.: Comparison of the different source terms of inverse Compton scattering: The dotted lines show the Thomson (green, T) and Klein-Nishina (blue, KN) regime in the δ -approximation from [Mastichiadis and Kirk \(1995\)](#) and the solid red line their sum ($T+KN$). The solid black line (*full from GB*) shows the full integral of [Blumenthal and Gould \(1970\)](#) and their analytical approximations are the dashed black line (*T from GB*) for the Thomson regime and the dash-dotted black line (*KN from GB*) for the Klein-Nishina regime. The lower plot shows the fraction of each component to the full integral. The electron spectrum is assumed to be a power law for $10 \leq \gamma \leq 10^{10}$ with spectral index $-p = -2$ and a black-body temperature of $\Theta = 10^{-5}$ is used.

also visible in the results from plasmoids. The Klein-Nishina regime shows also a difference up to factor two when comparing the full integral and the approximation from [Mastichiadis and Kirk \(1995\)](#). In this regime the numerical solving of the full integral is rather complicated and this result was obtained by a substitution to a photon energy normalised to the energy scale corresponding to the black body temperature. The fact that the dashed dotted line deviates also significantly from the full integral indicates that the solution of the full integral might have a limited accuracy.

It can be furthermore seen that the spectral indices of the all solutions show the expected behaviour. For the Thomson regime it is $-(p + 1)/2 = -1.5$ and in the Klein-Nishina regime a spectral index of about $-(p + 1) = -3$ can be observed.

4.10. Inverse Compton Scattering on a Black Body in Steady State

The second cross-check for the inverse Compton scattering consists of a steady state of an electron power-law distribution scattering only on an extra black body. The terms that are included are though:

$$\frac{\partial n_e}{\partial \tau} = K\gamma^{-p} - L_{IC,T}^e - L_{IC,KN}^e \quad n_e(\gamma, \tau = 0) = 0 \quad (4.97)$$

$$\frac{\partial n_\gamma}{\partial \tau} = Q_{IC,T}^\gamma + Q_{IC,KN}^\gamma - L_{esc}^\gamma \quad n_\gamma(\tau = 0) = 0 \quad (4.98)$$

The escape term is given similar to the synchrotron case by $L_{esc}^\gamma = 2n_\gamma/L$ and also for the self-absorption term the length scale is chosen to be the size of the reconnection layer. The same exemplary value of $\Theta = 1 \cdot 10^{-5}$ is used. In this case a spectral index of $-p = -3$ in combination with a injection between $10 \leq \gamma \leq 10^7$ show the different regimes clearly. The results for the electrons (top) and photons (bottom) are given in fig. 4.12. After 5 light-crossing times the electron spectrum shows a steady state consisting of three regimes: One regime below the injection with a spectral index of $-a_1 = -2$ and in accordance with [Mastichiadis and Kirk \(1995\)](#) the Thomson regime with $-a_2 = -p - 1 = -4$ and the Klein-Nishina regime $-a_3 = -p + 1 = -2$. This is confirmed by the fitted spectral indices given in the boxes on the red bands. The photon spectrum resembles the different regimes from the electron spectrum. At first, for very low energies a Rayleigh-Jeans tail with spectral index 1 can be found. Then the two features in the Thomson regime translate their spectrum to the spectral indices $-(a_1 + 1)/2 = -1.5$ and $-(a_2 + 1)/2 = -2.5$ for $a_1 = -2$ and $a_2 = -4$. Then the artefact from the transition from the Thomson to the Klein-Nishina regime can be seen as hardening resulting in a small hump. At higher energies the Klein-Nishina regime sets in with a spectral index of $-a_3 - 1 = -p = -3$.

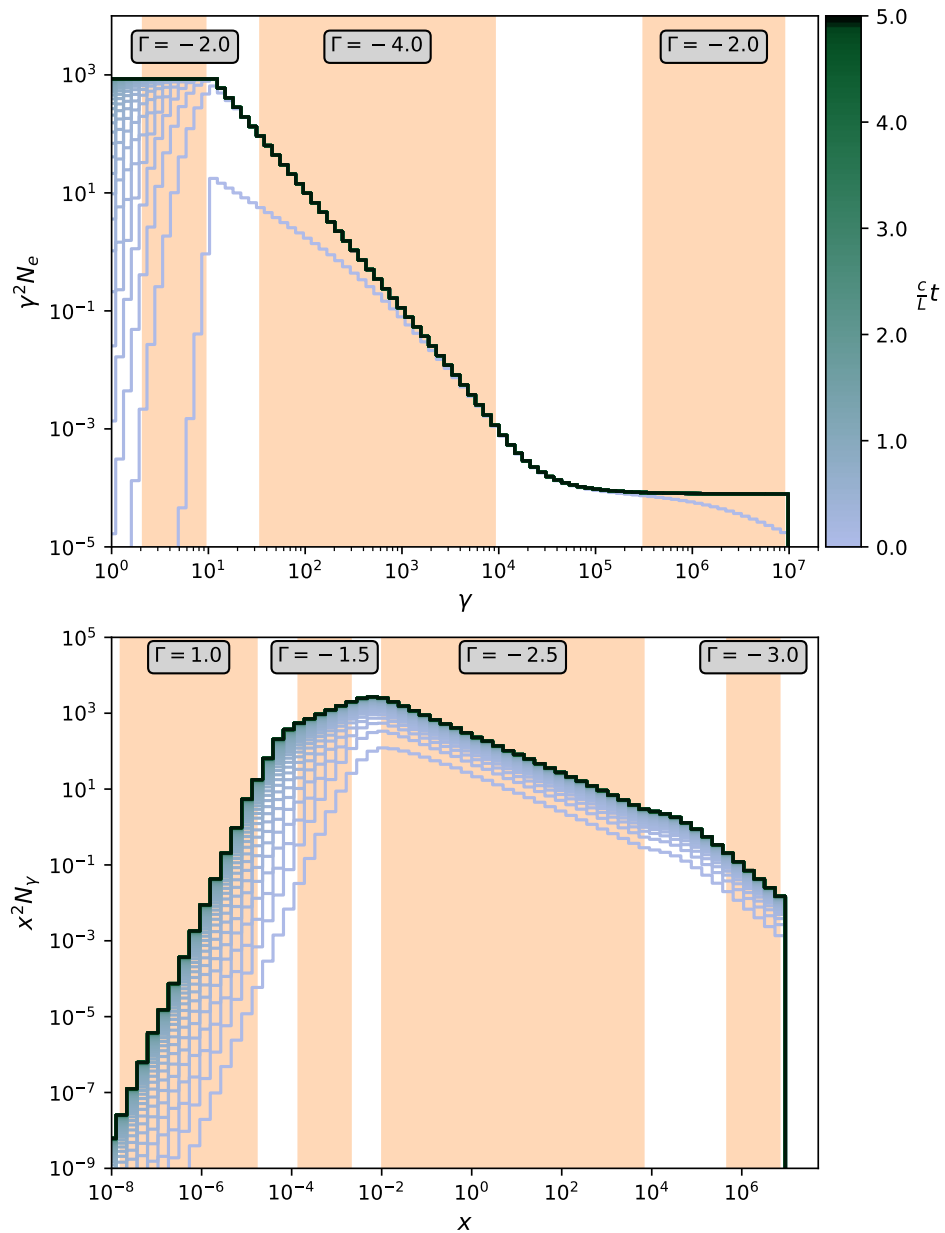


Figure 4.12.: Electron (top) and photon (bottom) spectrum for a fixed power law electron spectrum and only inverse Compton scattering and losses at the boundaries. For the escape term the system size is chosen to a representative value of the length of the reconnection layer $L = 5 \cdot 10^{16}$ cm and an exemplary black-body temperature of $\Theta = 10^{-5}$. Colour encodes the temporal evolution from blue to dark green. In the orange marked energy ranges a power law fit has been performed and the spectral index of n_e is given in the box.

4.11. Modelling the Radiation in a Plasmoid

As the overall idea is, to generate fluxes as measured in the observer's frame, which does not move with respect to the galaxy (except for redshifts and other propagation effects), the high speeds of the plasmoids in the jet introduce relativistic effects. The setup considered is the same as in [Christie et al. \(2019a\)](#) and consists of three different frames: First, the rest frame of the plasmoid, where the radiation modelling is done. Second, the rest frame of the reconnection layer, where the Monte Carlo simulations are performed. Finally, there is the observer's frame, which is assumed to be the same as the galaxy's rest frame. Additionally, the rest frame of the broad line region is assumed to be the same as the galaxy's rest frame. In this thesis, the following notations are used:

- plasmoid frame K : unprimed
- layer frame K' : primed
- observer frame = galaxy frame = black body rest frame K'' : twice primed

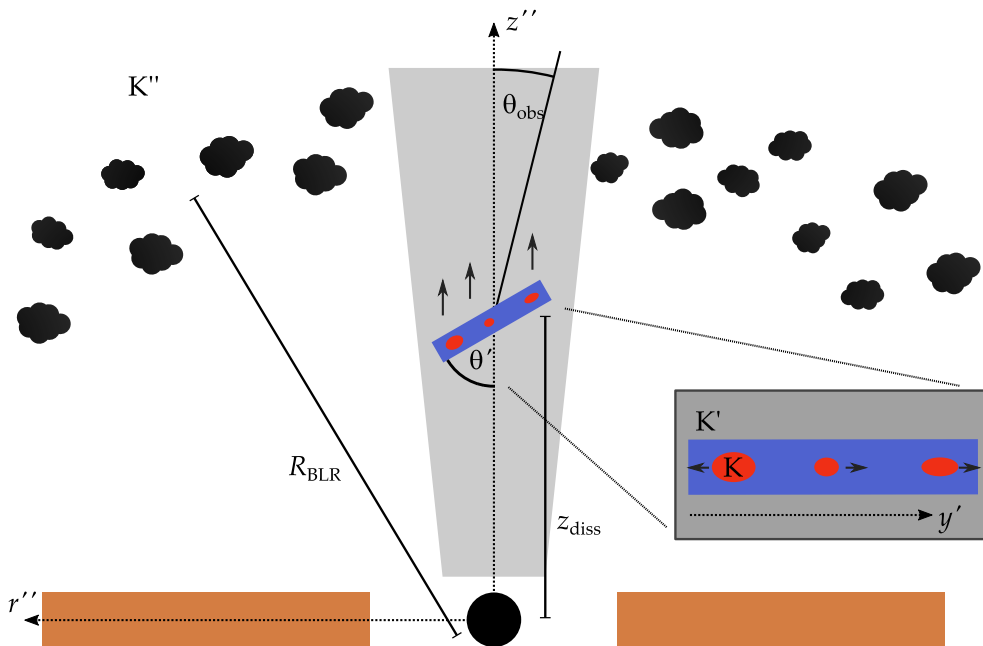


Figure 4.13.: General setup: The black hole and the accretion disk (brown) produce a jet (light grey). At a distance z_{diss} a significant amount of energy from the jet's magnetic field is dissipated away via a reconnection layer (blue) with plasmoids (red). The plasmoids with rest frame K move in one dimension in the layer, that is tilted by the angle θ' with respect to the jet's axis and moving in the jet. The observer sees the layer under an angle θ_{obs} . The black clouds denote the BLR at a distance R_{BLR} .

The general strategy is thus to compute the Doppler factor of the BLR with respect to each plasmoid at the correct time, see section 4.11.1 and section 4.11.2. Then the black-body temperature and the size of each plasmoid can be used to determine the electron

injection and photon escape terms, see section 4.11.3. After this, the escape term can be sliced either into time bins to yield a light curve or into energy bins to yield a spectrum, see section 4.11.5.

In order to model the radiation in a moving plasmoid it is furthermore assumed that the plasmoid is an ellipsoid with a constant magnetic field and a constant number density inside. This is motivated by the PIC results and the ideas of [Christie et al. \(2019a\)](#). For the sake of clearness the normalised times are denoted by the symbol t throughout this chapter. Remember that also lengths are normalised to the layer's length L .

4.11.1. Doppler Factor of Plasmoid and Broad Line Region

In analogy to eqs. (4.9) to (4.11), the Doppler factor that is boosting the emission of a plasmoid to the observer's frame can be calculated from the relativistic addition of velocities, aberration of the angles and the definition of the Doppler factor in eq. (4.7), compare also to [Christie et al. \(2019a\)](#). Looking at fig. 4.13, two types of motion need to be combined, the motion of the plasmoid in the layer's rest frame and the bulk velocity of the jet. The first is characterised by the MC simulations of the layer, which gives β'_p , while the second is assumed to be at a constant speed β''_{jet} corresponding to Γ''_{jet} .

Now let K' be the layer frame, where the plasmoid moves along the y' -axis and let K'' be the observer frame, which is tilted by the angle θ'' and moving with the speed of the layer in the jet β''_{jet} . Call the axes z'' and r'' as in the sketch, then the direction of motion can be divided into a parallel dy'_{\parallel} and a perpendicular component dy'_{\perp} . Then, a change of the plasmoids position in K'' is given by a Lorentz-transformation:

$$dz'' = dy''_{\parallel} = \Gamma''_{jet} (dy'_{\parallel} + \beta''_{jet} dt') = \Gamma''_{jet} (dy' \cos \theta' + \beta''_{jet} dt') \quad (4.99)$$

$$dr'' = dy''_{\perp} = dy'_{\perp} = dy' \sin \theta' \quad (4.100)$$

$$dt'' = \Gamma''_{jet} (dt' + \beta''_{jet} dy'_{\parallel}) = \Gamma''_{jet} (dt' + \beta''_{jet} dy' \cos \theta') \quad (4.101)$$

Defining $\frac{dy'}{dt'} := \beta'_p(t')$, this yields the velocity of the plasmoid in K'' (relativistic addition of velocities):

$$\beta''_p(t') = \frac{dz''}{cdt''} = \frac{\beta''_{jet} + \beta'_p(t') \cos \theta'}{1 + \beta''_{jet} \beta'_p(t') \cos \theta'} \quad (4.102)$$

From this the Lorentz factor according to β''_p can be calculated:

$$\Gamma''_p(t') = \Gamma''_{jet} \Gamma'_p(t') \left[1 + \beta''_{jet} \beta'_p(t') \cos \theta' \right] \quad (4.103)$$

Then the Doppler factor is given by:

$$\delta_p = \frac{1}{\Gamma''_p(t') \left[1 - \beta''_p(t') \cos(\theta'' - \theta''_{Obs}) \right]} \quad (4.104)$$

Here the angle θ''_{Obs} appears, which is the angle between the axis of the jet and the direction towards the observer.

Since the BLR is assumed to be a black body in the rest frame of the galaxy, it has to be boosted into the plasmoids frame as well. The considerations are completely analogue to the ones for the plasmoid-observer case, except for the detail, that the sign of the relative velocity depends on the model. Assuming that the BLR is aligned at an angle θ''_{BLR} with respect to plasmoid motion as measured in the galaxies rest frame, the Doppler factor reads:

$$\delta_{\text{BB}} = \frac{1}{\Gamma_p''(t') \left[1 \mp \beta_p''(t') \cos \theta''_{\text{BLR}} \right]} \quad (4.105)$$

The \pm arises due to the different arrangements of plasmoid and BLR for different blazar types, either the reconnection is outside of the BLR (-) or vice versa (+).

4.11.2. Boosting the Results of the Radiation Modelling

Based on PIC simulations the Monte Carlo code yields the size s' , velocity β' and position r' of each plasmoid in a chain as a function of the layer time t' . This is then used as an input to calculate the evolution of the number densities in the plasmoid. The size of the plasmoid is basically needed for the loss term and the synchrotron self-absorption. Since the size is measured perpendicular to the plasmoid's motion, it is not affected by relativistic effects: $s = s'$. For the inverse Compton terms the velocity of the plasma with respect to the black body (= broad line clouds) is needed. This yields the Doppler factor δ derived in section 4.11.1. Both, s and δ are still only given at time steps t' in the layer's frame. This grid of t' can be converted with an instantaneous Lorentz-transformation to the plasmoid's frame:

$$t(t') = \int_{t'_0}^{t'} \frac{d\tau'}{\Gamma(\tau')} + t(t'_0) = \int_0^{t'-t'_0} \frac{d\tau'}{\Gamma(\tau' + t'_0)} + t(t'_0) \quad (4.106)$$

To simplify calculations $t(t'_0) = 0$ is chosen. By this, $s(t)$ and $\beta'(t)$ are known at the grid points $t(t')$ and can be interpolated, since $\Gamma(\tau') > 1$ which ensures $t < t'$. Then the radiation modelling can be done in the plasmoid's frame and yields the spectral number density $n_\gamma(x, t)$. The escape term of the photon equation is then converted into a spectral number of escaped particles.

Next, the results need to be boosted to the observer's frame. First the relation between the frequencies x in the plasmoid's rest frame and x'' in the observer's frame is simply a Doppler factor (eq. (4.7)). Second, the spectral number density transforms using four Doppler factors. Third, the time grid t needs to be converted to the one of the observer t'' by another instantaneous LT using the Doppler factor $\delta(t)$:

$$t''(t) = \int_{t_0=0}^t \frac{d\tau}{\delta(\tau)} + \frac{t'_{ini}}{\Gamma_{jet}} \quad (4.107)$$

4.11.3. Injection and Escape

PIC simulations suggest that the comoving number density of a plasmoid is constant in time:

$$\frac{dn_{\text{co}}}{dt} = 0 \quad \Rightarrow \quad \frac{dN}{dt} = n_{\text{co}} \frac{d\hat{V}}{dt} \quad (4.108)$$

The continuous growth requires thus a permanent injection of electrons. Denote their spectral shape as $F(\gamma)$, which is normalised to one:

$$\int_1^\infty F(\gamma) d\gamma = 1 \quad (4.109)$$

Then the spectral rate of injection for a plasmoid can be written as:

$$\frac{\partial^2 N}{\partial t \partial \gamma} = R(t) \cdot F(\gamma) \quad (4.110)$$

Here $R(t)$ is the total rate of injected particles into a plasmoid:

$$R(t) = \int_1^\infty R(t) F(\gamma) d\gamma = \int_1^\infty \frac{\partial^2 N}{\partial t \partial \gamma} d\gamma = \frac{dN}{dt} = n_{\text{co}} \frac{d\hat{V}}{dt} \quad (4.111)$$

To convert this to a number density, it has to be divided by the volume of the plasmoid:

$$\frac{\partial^2 n}{\partial t \partial \gamma} = \frac{n_{\text{co}}}{\hat{V}} \frac{d\hat{V}}{dt} F(\gamma) \quad (4.112)$$

Now three other assumptions are motivated by PIC simulations. First, the spectral shape of injection can be written as a power law with a magnetisation-dependent spectral index:

$$F(\gamma) = \frac{1-p}{\gamma_{\max}^{1-p} - \gamma_{\min}^{1-p}} \gamma^{-p} \quad (4.113)$$

For values $\gamma_{\min} \leq \gamma \leq \gamma_{\max}$ F is set to 0. Second, the plasmoids can be approximated as ellipsoids:

$$\hat{V} \propto s^3 \quad \Rightarrow \quad \frac{1}{\hat{V}} \frac{d\hat{V}}{dt} = \frac{3}{s} \frac{ds}{dt} = \frac{3}{s} \frac{\beta_g}{f_{\text{sup}}(\beta_p)} \quad (4.114)$$

where the parameterisation of eq. (3.21) has been used. The third assumption is necessary to determine the comoving number density n_{co} . PIC simulations show a rough equipartition between magnetic fields and relativistic particles (Christie et al. 2019a):

$$U_{\text{rel}} = \frac{m_e c^2}{\sigma_T L} l_{\text{rel}} = \frac{m_e c^2}{\sigma_T L} \int_1^\infty d\gamma n_{\text{co}} \gamma F(\gamma) \quad (4.115)$$

$$U_B = \frac{B^2}{8\pi} \quad (4.116)$$

Leaving the ratio of both as a free parameter this yields:

$$n_{\text{co}} = \frac{\sigma_T L}{m_e c^2} \frac{8\pi}{B^2} \frac{2-p}{1-p} \frac{\gamma_{\max}^{1-p} - \gamma_{\min}^{1-p}}{\gamma_{\max}^{2-p} - \gamma_{\min}^{2-p}} \frac{U_{\text{rel}}}{U_B} \quad (4.117)$$

Putting all together:

$$Q_{\text{inj}}^e(\gamma, t) = \begin{cases} \frac{3n_{\text{co}}}{s(t)} \frac{\beta_g}{f_{\text{sup}}(\beta_p)} \frac{1-p}{\gamma_{\max}^{1-p} - \gamma_{\min}^{1-p}} \gamma^{-p} & \gamma_{\min} \leq \gamma \leq \gamma_{\max} \\ 0 & \text{otherwise} \end{cases} \quad (4.118)$$

For the photons no additional source term is included. However the black-body radiation from the external BLR acts indirectly as an energy injection to the system. Following [Christie et al. \(2019a\)](#), the escape of electrons from the system can be neglected. This can be motivated by comparing the cooling time to the size of the plasmoids, which is proportional to their escape time. This is different for the photons, where the escape term corresponds to those photons emitted from the blazar. The proper transformation of this is topic of the next subsection.

4.11.4. After Leaving the Layer

As soon as a plasmoid leaves the layer, it is per se no clear how to proceed with the processing of a plasmoid, since the PIC simulations make no statement about the regions outside of the layer. Furthermore, the physical conditions in the jet are expected to be turbulent and extremely complicated. Following [Christie et al. \(2019a\)](#) it is therefore assumed that the plasmoid continues its motion for a constant time without further growth ($s = \text{const}$), acceleration ($\beta = \text{const}$) or injection of electrons. For this time values between $\tau_{\text{add}} = 0.5$ and $\tau_{\text{add}} = 1$ are chosen.

4.11.5. Transformation of the Photon Escape

At each time step of the evolution of the photons, there is a loss scaling with the radius of the plasmoid. This is only an approximation as neither the plasmoid is spherical but ellipsoidal nor is even the assumption of an ellipsoid completely true and only a simplification of the PIC results. Nevertheless, the total emission of a plasmoid is computed from the loss of the number density integrated over the whole normalised volume:

$$\hat{V}_p = \frac{\pi s^3 L^3}{4\sigma_T L} \quad (4.119)$$

$$\frac{\partial^2 N}{\partial t \partial x}(x, t) = \frac{\hat{V}}{\tau_{\text{esc}}} n_\gamma(x, t) = \frac{\pi}{2} \frac{s^2 L^2}{\sigma_T} n_\gamma(x, t) \quad (4.120)$$

where a factor 2 comes in from $\tau_{\text{esc}} = s/2$. This can now be processed in two ways, a binning in time yields basically a light curve L and a binning in energy a spectrum νL_ν :

$$L = \int dE E \frac{dN}{dEdt} \quad \nu L_\nu = E^2 \frac{dN}{dEdt} \quad (4.121)$$

To convert time from the layer's light crossing time $\tau = tc/L$ to real time t and $x = E/m_e c^2$ to energy, in both cases the same conversion factor arises: $m_e c^3/L$. As defined in eq. (4.17), both, spectrum and light curve, get multiplied by a factor δ_p^4 to be transformed to the observer's frame.

4.12. Results for Single Plasmoids

Choice of Parameters

To validate the developed code parameters similar to [Christie et al. \(2019a\)](#) are used to compare the results for single plasmoids. They are summarised in table 4.1. Two parameter sets were chosen in a way that represents the characteristics of the two blazar sub-classes, FSRQs and BL Lacs (see section 1.2). Both are based on the same MC parameters and an exemplary plasmoid of medium final size is chosen. Its speed is positive (towards the right edge) and the observer and the BLR are assumed to have perfect alignment ($\theta' = \theta_{\text{obs}} = 0$). In case of the FSRQs the region of energy dissipation is placed inside of the BLR, in contrast to the other case. Also the total luminosity of the BLR L_{BLR} is chosen much higher. Both facts lead to an increase in the emission due to inverse Compton scattering at higher energies. Furthermore, for the BL Lacs the energy injection happens at a higher energy range.

	FSRQ	BL Lac
σ	10	10
L [cm]	$1 \cdot 10^{16}$	$1 \cdot 10^{16}$
B [G]	7	2
γ_{\min}	94	560
γ_{\max}	$5 \cdot 10^3$	$5 \cdot 10^4$
$-p$	-2.1	-2.1
U_{rel}/U_B	1.1	1.4
$\Theta = kT/m_e c^2$	$1 \cdot 10^{-5}$	$1 \cdot 10^{-5}$
L_{BLR} [erg s $^{-1}$]	$1.2 \cdot 10^{46}$	$5 \cdot 10^{41}$
Γ_{jet}	12	12
z_{diss} [cm]	$1 \cdot 10^{17}$	$1 \cdot 10^{18}$
R_{BLR} [cm]	$5 \cdot 10^{17}$	$5 \cdot 10^{17}$

Table 4.1.: Parameters for the calculation of the radiation modelling in a plasmoid and the boosting to the observers frame in this section. ([Christie et al. 2019a](#))

Results in the Rest Frame

Figure 4.14 shows the temporal evolution of the spectral number density of the electrons, which is obtained with the FSRQ parameters. The injection spectrum at the early dark times evolves towards a steady state like behaviour (green). As soon as the plasmoid leaves the layer and the injection stops, the electrons at high energies cool down quickly. This behaviour drives the evolution of the spectral photon number density in fig. 4.15. Initially no photons are assumed to be present and the first time step already shows a rather stable distribution. As soon, as the injection of high energetic electrons stops, also the high energy photon population disappears and finally the complete population escapes from the plasmoid.

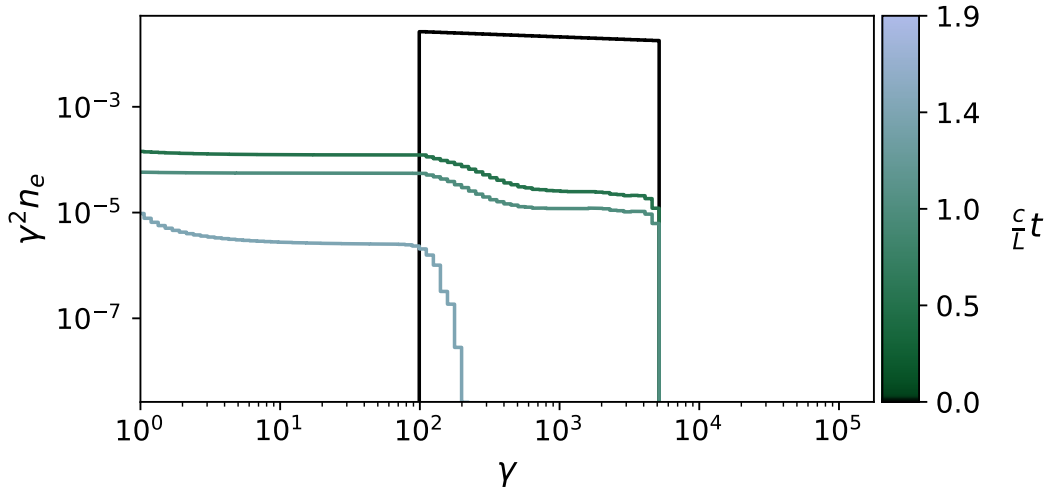


Figure 4.14.: Temporal evolution of the spectral electron number density for an exemplary plasmoid with the FSRQ parameters in the plasmoid's rest frame. The darkest line shows the initial distribution, which evolves towards a steady state until the injection stops and the electrons at high energies cool down fast.

To understand the features visible in the photon spectrum fig. 4.16 focuses on the two distributions at a time step of about one third of the total time. As one would expect a double hump structure is visible: The first peak at low energies originates from the effect of synchrotron radiation, while the second one is produced by the inverse Compton scattering. In the case of the FSRQ parameters the inverse Compton peak is much higher than the synchrotron peak, which reflects the choice of a luminous BLR moving towards the plasmoid. This suggests the interpretation that the evolution of the number densities is dominated by inverse Compton scattering. Thus, below the range of injection a power law with spectral index -2 independent of the injection is expected. Knowing the spectral index of injection to be $-p = -2.1$, also a value of $-p - 1 \approx -3$ in the purple marked area can be interpreted as the Thomson regime. However, a spectral index of about -2 at the highest energies (red band) does not fit to the Klein-Nishina regime. The corresponding photon spectrum in the plot below can now be divided into

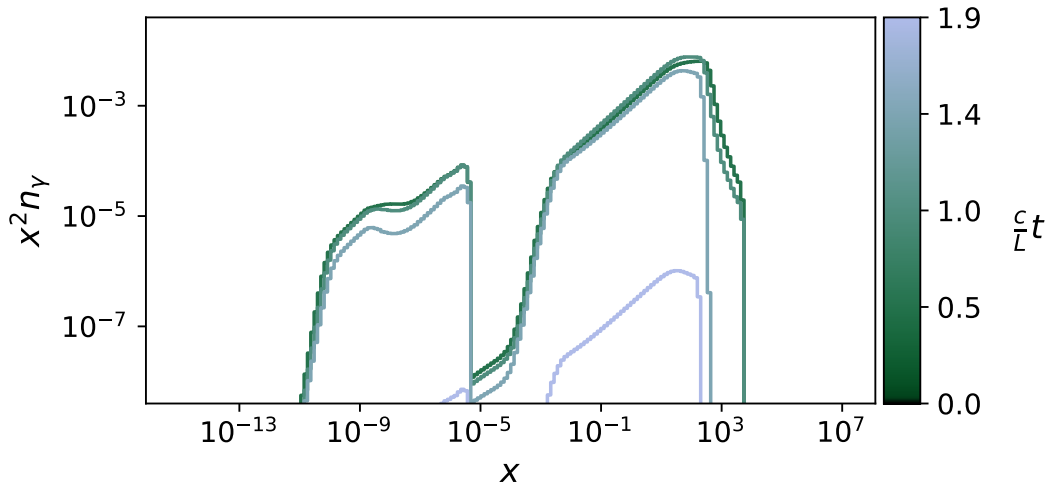


Figure 4.15.: Temporal evolution of the spectral photon number density for an exemplary plasmoid with the FSRQ parameters in the plasmoid's rest frame. The darkest line shows the initial distribution, which evolves towards a steady state until the injection stops and the electrons at high energies cool down fast.

the synchrotron and the inverse Compton peak. The structure of the synchrotron peak resembles exactly the one from the electron spectrum (according to $-(p + 1)/2$) in the optical thin region marked by the blue band, while the range below shows a spectral index of 1.5 as expected in the optical thick regime. The inverse Compton peak shows a rich phenomenology, where the last three regions can be assigned to each of the three regions in the electron spectrum. In the energy range between the blue and the orange band spectral indices of -1.5 and 0.5 are observed, which might originate from the edge of the Thomson approximation, where the electrons become non-relativistic or from the effect of synchrotron self-Compton scattering. Furthermore, the maximum energies of both peaks correspond to the values expected from the maximum electron energy: $x_{\text{syn, max}} = \hat{b}\gamma_{\text{max}}^2 \approx 4 \cdot 10^{-6}$ and $x_{\text{IC, max}} = \gamma_{\text{max}} = 5 \cdot 10^3$.

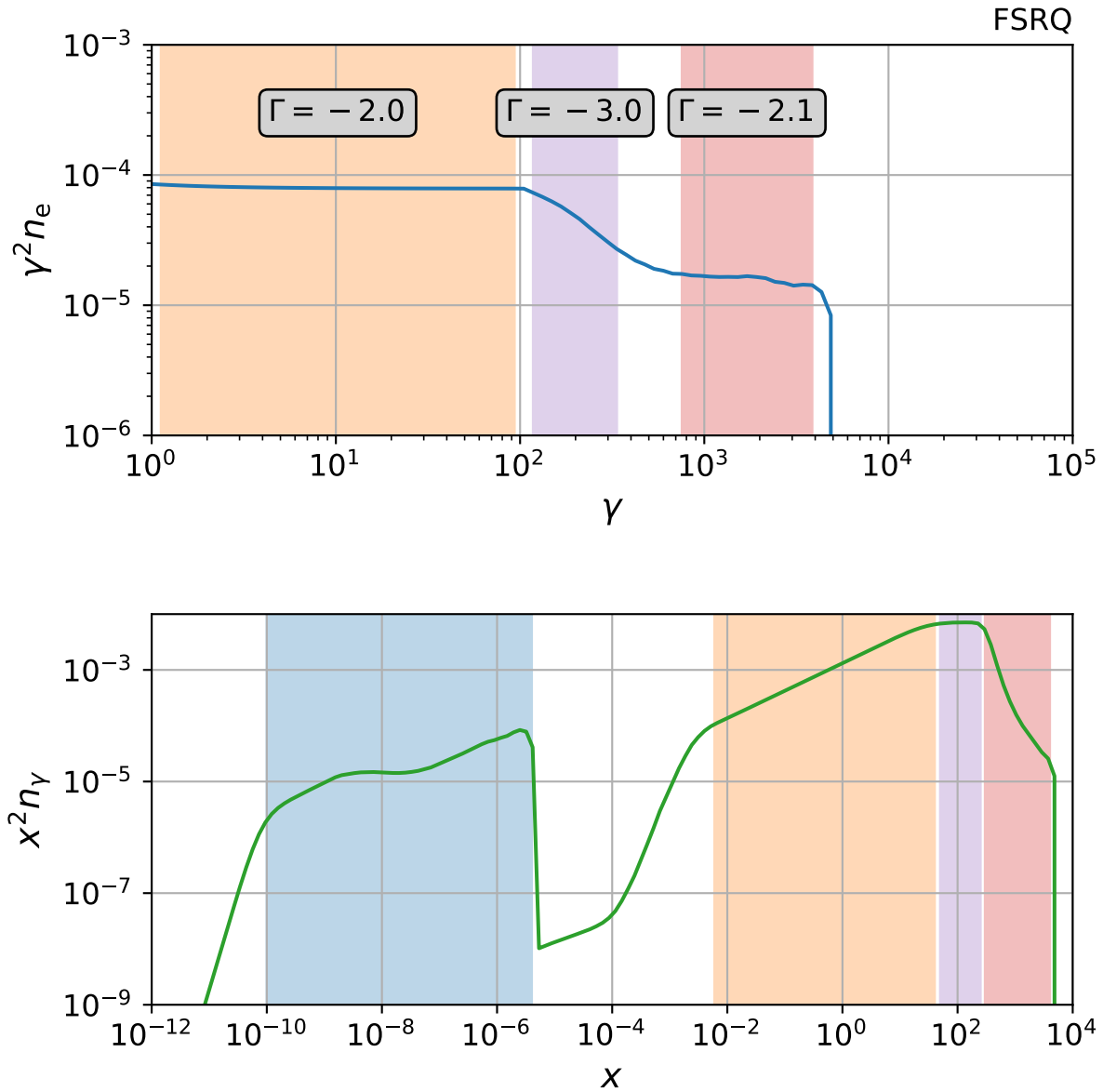


Figure 4.16.: Electron (top) and photon spectrum (bottom) at about two thirds of the simulated time. Within the coloured bands in the electron plot the given spectral indices (Γ) are fitted. In the lower plot the blue band marks the range, where the synchrotron emission resembles the electron distribution in the optical thin regime (spectral indices of -1.5, -2 and -1.5). The orange ($\Gamma = -1.5$), purple ($\Gamma = -2$) and red bands correspond to the ranges in the electron plot.

In fig. 4.17 the evolution of the spectral electron number density for the BL Lac parameters is shown. A similar behaviour as in the case of the FSRQs is observed. Again, the initial injection spectrum can be seen in black, although this time shifted to higher energies. From this, a rather stationary state evolves and the same behaviour can be seen when the injection stops. Additionally, this time the low energy population below Lorentz factors of few hundreds, the population drops extremely steep by about six orders of magnitude and then reaches a plateau, which remains rather constant in time. The analogon for the photons is plotted in fig. 4.18. Also here a two-hump structure is visible, which remains present until the injection stops and a new feature comes in, as the electron population changes significantly.

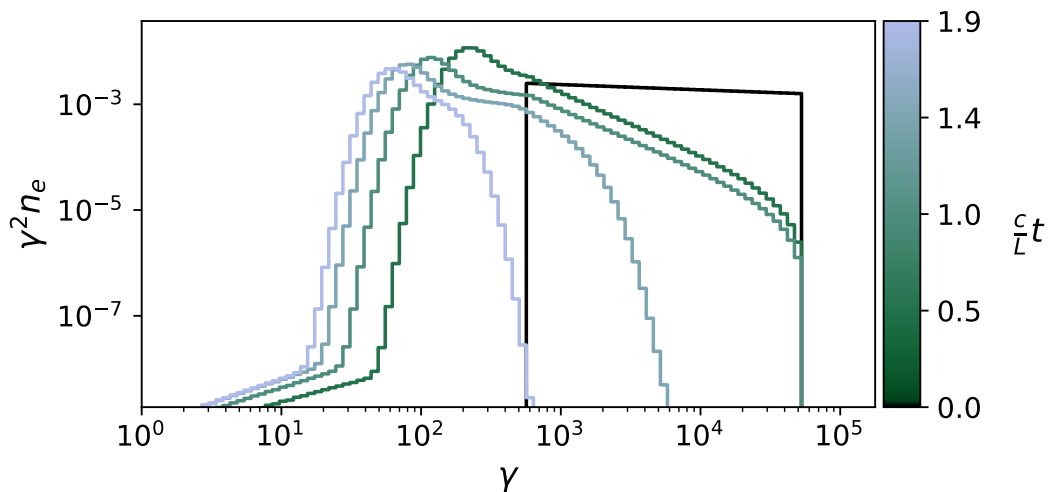


Figure 4.17.: Temporal evolution of the spectral electron number density for an exemplary plasmoid with the BL Lac parameters in the plasmoid's rest frame. The darkest line shows the initial distribution, which evolves towards a steady state until the injection stops and the electrons at high energies cool down fast.

To discuss the features in the photon spectrum, again both spectra at about one third of the total time are shown separately in fig. 4.19. The dominance of the synchrotron peak suggests this time, that also the electron spectrum is dominated by synchrotron radiation. This fits to the power law with spectral index $-\alpha = -p - 1 \approx -3.1$ which can be found roughly between 10^2 and $10^{4.5}$. However, the electron spectrum shows a complicated feature below the lower bound of the injection, which is marked by the red line. This feature and the power law above can then be found exactly in the synchrotron peak of the photon spectrum. The position of the red line fits exactly to the lower bound of the electron injection ($x_{\min, \text{inj}} = \gamma_{\min}^2 \hat{b}$). Also the spectral index yields as expected $-(\alpha + 1)/2 = -2.1$. For the inverse Compton peak the spectral index decreases from values slightly above -2 to values below and then steepens further until it goes down to zero. This is in agreement with the trend of the electron spectrum, which also becomes softer at higher energies. The spectral index of about $-(\alpha + 1)/2 \approx -2$ fits to

the expectation from the Thomson regime. The red line in the inverse Compton peak marks again a feature, which origin might either be the hump in the electron spectrum or the little artefact in the transition from the Thomson to the Klein-Nishina regime, compare section 4.9. Also here the maximum energies of both peaks correspond to the values expected from the maximum electron energy: $x_{\text{syn, max}} = \hat{b}\gamma_{\text{max}}^2 \approx 1.1 \cdot 10^{-4}$ and $x_{\text{IC, max}} = \gamma_{\text{max}} = 5 \cdot 10^4$.

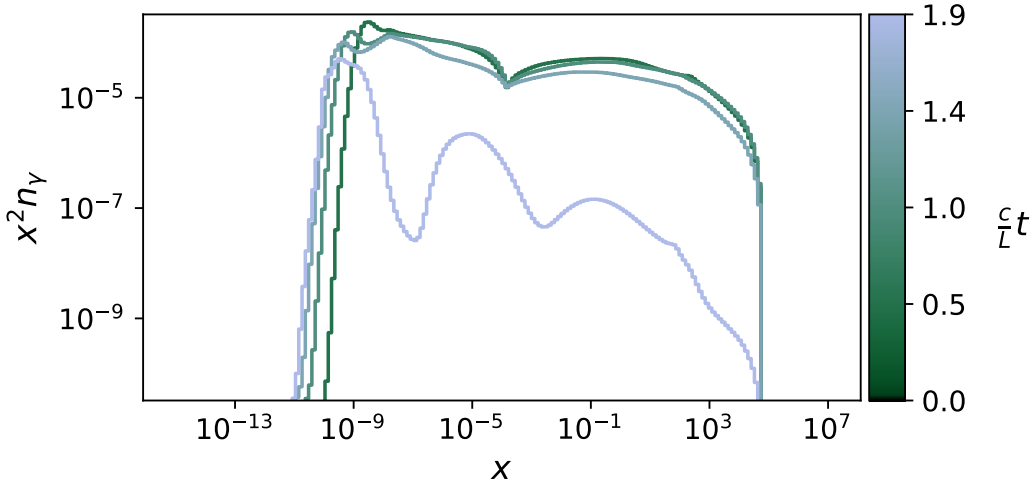


Figure 4.18.: Temporal evolution of the spectral photon number density for an exemplary plasmoid with the BL Lac parameters in the plasmoid's rest frame. The darkest line shows the initial distribution, which evolves towards a steady state until the injection stops and the electrons at high energies cool down fast.

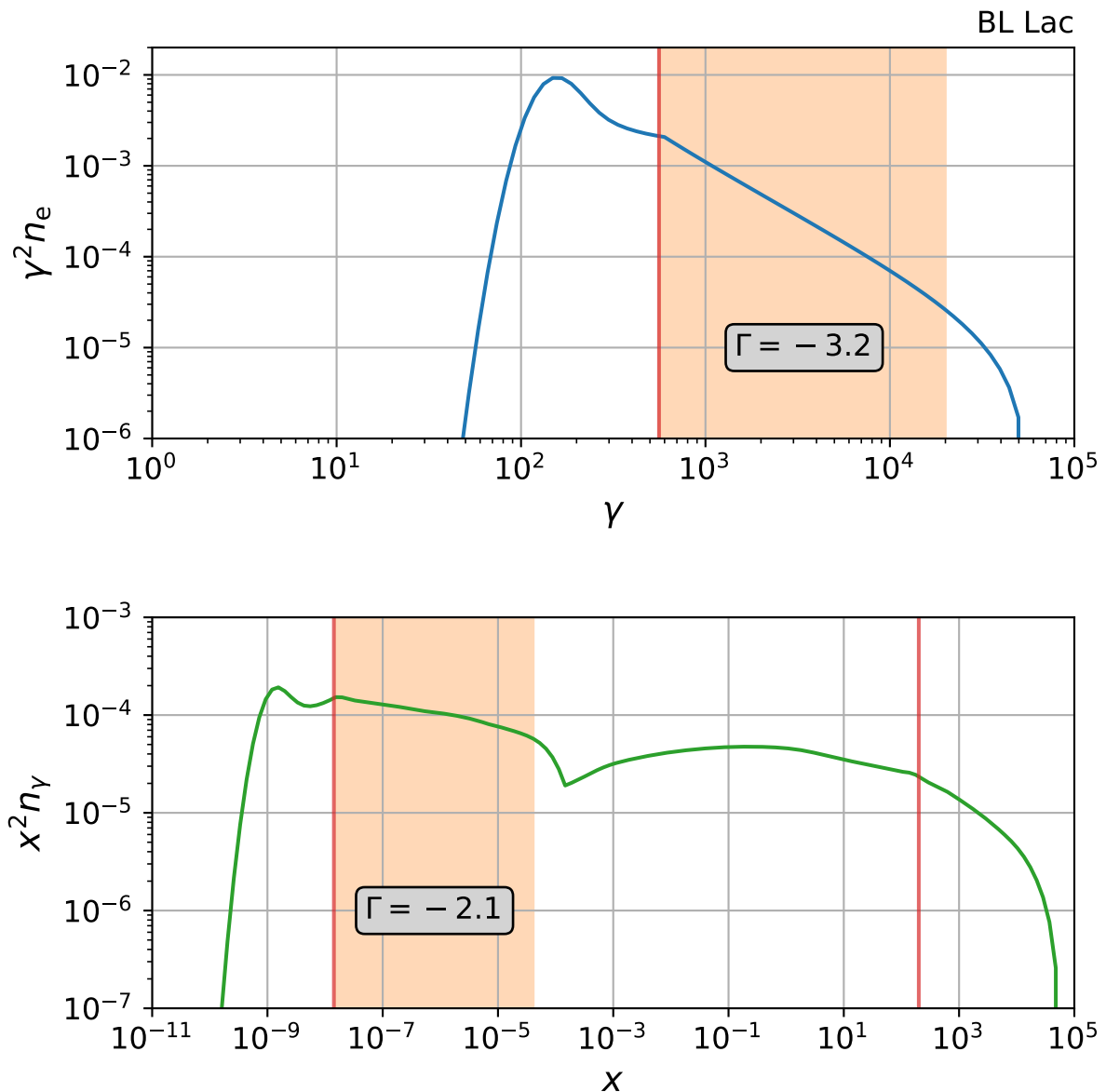


Figure 4.19.: Electron (top) and photon spectrum (bottom) at about two thirds of the simulated time. Within the coloured bands in the electron plot the given spectral indices (Γ) are fitted. The red line in the upper plot corresponds to the minimum injected energy. This transfers to a photon energy of $x_{\text{syn, min}} = \hat{b}\gamma_{\text{max}}^2 \approx 1.4 \cdot 10^{-8}$. The second red line marks another feature visible in the inverse Compton hump ($x \approx 200$).

Observed Spectrum

Assuming perfect alignment, the resulting spectra for both cases are shown in fig. 4.20. No shape-changing differences compared to the results from the plasmoid's rest frame occur for this alignment. Comparing the frequency and flux range to the values from the blazar sequence these first results seem very promising. This choice of parameters allows for the production of the typical double-hump structure incorporating additionally the measured ratio between synchrotron and inverse Compton peak. This is in good agreement with previous results of [Christie et al. \(2019a\)](#) and [Schwefer \(2019\)](#) show good agreement. Now, further exploration of the parameter space is needed to draw conclusions from the features of observations and incorporate them also in the results of the model.

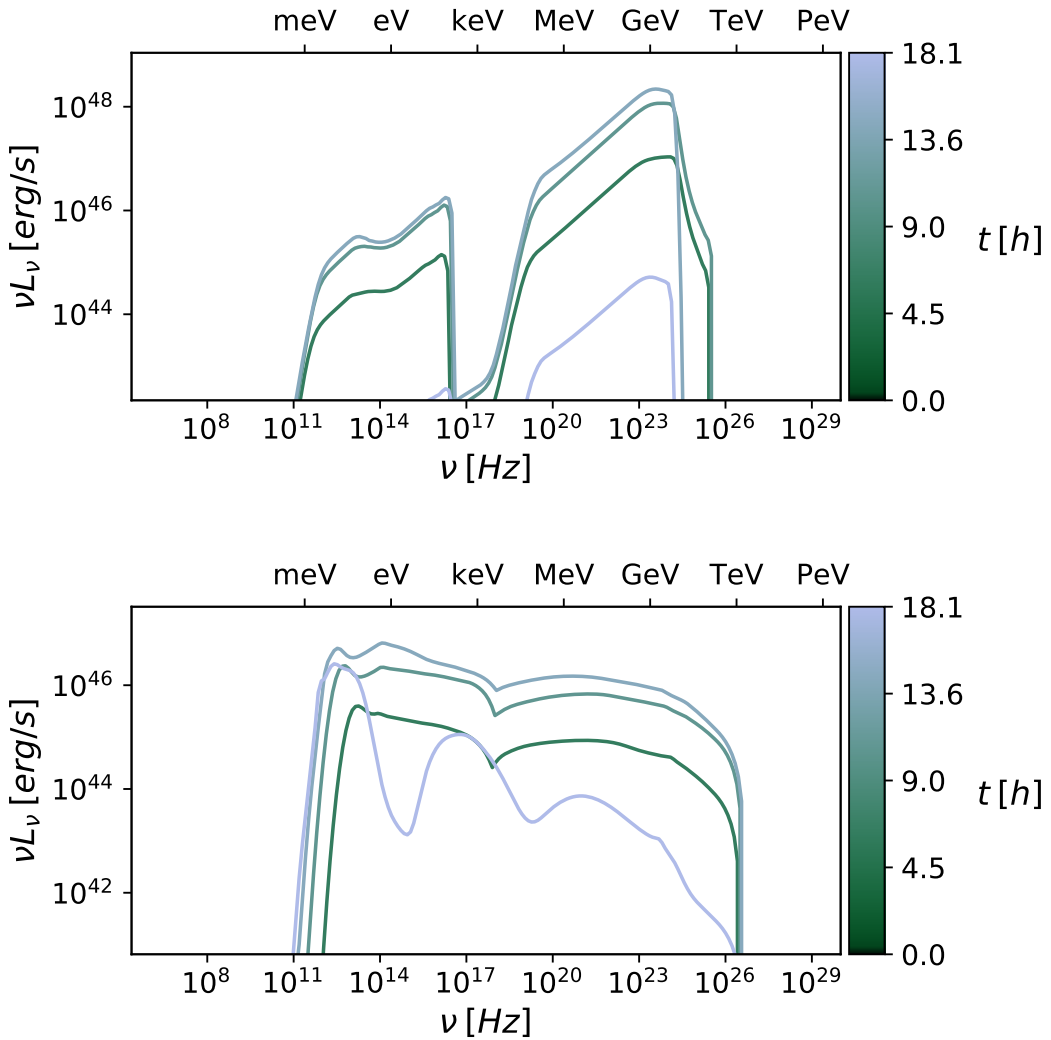


Figure 4.20.: Temporal evolution of the photon spectrum for an exemplary plasmoid with the FSRQ (top) and BL Lac (bottom) parameters in the observer's frame.

Observed Light Curves

Figure 4.21 compares the light curve for the same exemplary plasmoid for the two parameter sets FSRQ and BL Lac. Both are integrated between 100 GeV and 100 TeV, which corresponds to the VHE gamma-ray range as measured for example with FACT. For this particular example a flux doubling time compared to the maximum value of about 3 h to 4 h can be observed. This depends of course of course strongly on the final size and speed of the plasmoid. As expected, both curves reach their maximal value at the same time, since the time at which the plasmoid leaves the layer is of course not affected by the choice of the radiation parameters. The red BL Lac curve has as slightly lower value at its maximum than the blue one. This is however non-trivial, since the Doppler effect increases the luminosity, while the radiation parameters affect the maximum energy and the intensity of the inverse Compton peak. Furthermore, the BL Lac light curve decays exponentially within about one hour, while the FSRQ light curve ends abruptly. Assuming that the FSRQ plasmoid is dominated by inverse Compton scattering, the high-energy electrons cool down much more efficient than in the synchrotron dominated BL Lac case. This results in a sudden drop in the production of high-energy photons, which yields a sudden drop in the VHE light curve. In the BL Lac case the electrons cool down continuously by synchrotron radiation, which takes longer and an exponential decay emerges. These results show good agreement to [Christie et al. \(2019a\)](#) and [Schwefer \(2019\)](#).

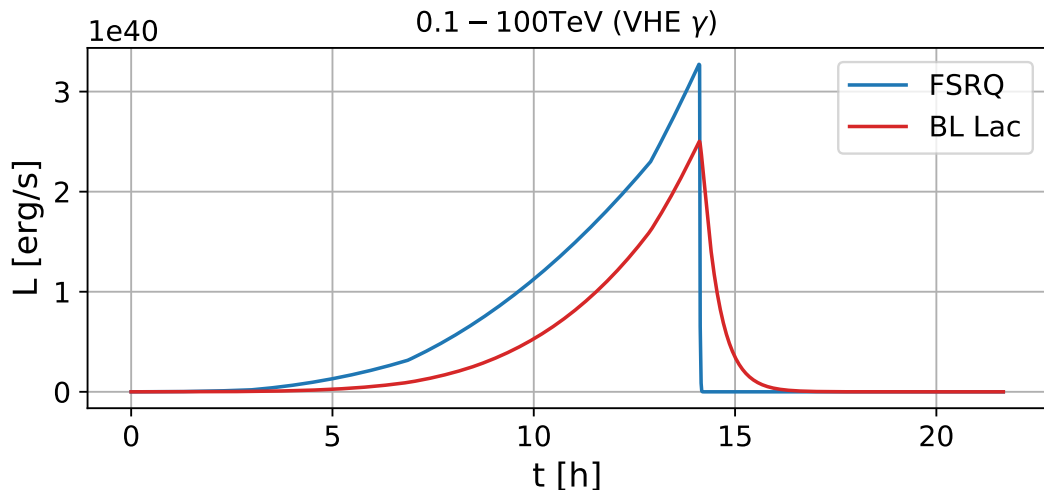


Figure 4.21.: VHE gamma-ray light curve (0.1 TeV-100 TeV) obtained from the two parameter sets from table 4.1. The same exemplary plasmoid with a medium final size is used.

4.13. Light Curves of a Complete Reconnection Layer

In fig. 4.22 the light curves of all plasmoids in one reconnection layer are added up according to their transformed time of appearance. Again, the VHE gamma-ray range

(0.1 TeV-100 TeV) as measured by FACT is chosen. In the figure, four light curves are plotted: The two red curves belong to the FSRQ parameters and the blue ones to the BL Lac parameters. Furthermore, the brighter lines show the light curves of all plasmoids of the reconnection chain, which lasts for about 6.5 days. A rich structure can be seen, where many short intense peaks from small and fast plasmoids are visible on top a few long lasting flares originating from large and slow plasmoids. This is a result of the interplay of the two effects that fast plasmoids are boosted to high intensities, but also large plasmoids emit a lot simply due to their size. To illustrate this, the dark lines show the light curves of the seven plasmoids with the largest final sizes. Here the decaying behaviour as in fig. 4.21 can be observed. For some plasmoids even no emission in the BL Lac light curve can be observed, but not in the FSRQ. In addition, some medium flares (for example at the beginning or end of the red BL Lac curve) are visible, which probably originate from medium sized plasmoids. These are then large enough to produce significant emission and fast enough that this emission is also significantly boosted. This also explains the wide range of flux doubling times, which can go down far below one hour. A similar behaviour is also observed in [Christie et al. \(2019a\)](#) and [Schwefer \(2019\)](#).

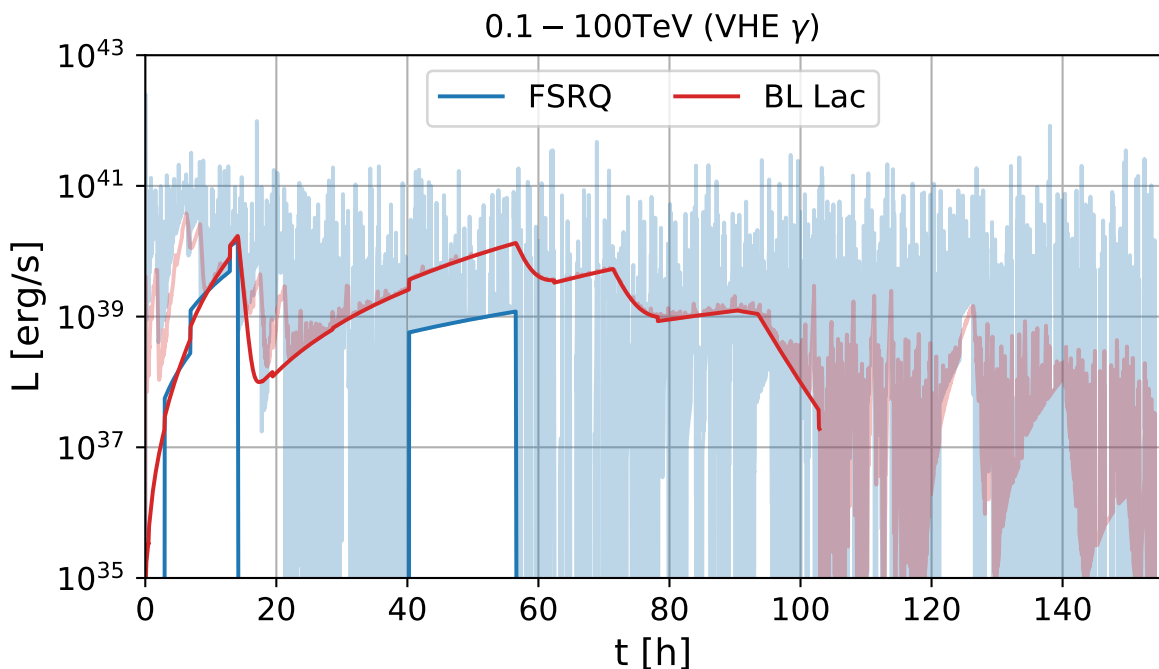


Figure 4.22.: VHE gamma-ray light curve (0.1 TeV-100 TeV) obtained from the two parameter sets from table 4.1. The emission of all plasmoids in the layer is summed up in the lighter lines, while the darker ones show only the light curve of the seven plasmoids with the largest final sizes.

5

Summary

In this thesis I worked towards a study of blazar variability combining a theoretical model based on magnetic reconnection with observations from the First G-APD Cherenkov Telescope (FACT).

I started by introducing blazars as a special case of active galactic nuclei and explained the particular difficulty to model their short time scale variability. Then, I explained imaging air Cherenkov telescopes (IACTs) as a technique to detect very-high-energy gamma-ray signatures of blazars and focused on FACT, which offers an unprecedented, unbiased long-term monitoring. I put special emphasis on its data acquisition and analysis chain. Additionally, I reviewed the FACT Monte Carlo sample and used it to study the efficiency of detector and data processing. By including the existing Monte Carlos into an SQL database and correcting for systematic effects I paved the way towards a fast calculation of spectra. Studying the efficiency of data acquisition and analysis chain I suggested improvements for future Monte Carlo productions.

Focusing on the theoretical model, I introduced the relevant effects of magnetohydrodynamics to describe magnetic reconnection, in particular in the context of the plasmoid instability. I explained how particle-in-cell (PIC) simulations in [Sironi, Giannios, and Petropoulou \(2016\)](#) support this concept and allow for a prediction of the temporal evolution of the characteristic properties of a plasmoid. [Petropoulou et al. \(2018\)](#) introduced a MC approach to resemble these PIC findings, which I tried to reproduce. My implementation yields the same behaviour for growth and motion of plasmoids. However, the integrated size and momentum distributions show differences in scaling and shape. In the following, I set into context the radiative processes and effects of special relativity which are essential to model the radiation inside of a plasmoid. I developed an implementation based on the results of [Mastichiadis and Kirk \(1995\)](#), which is capable of modelling synchrotron radiation in the optically thin and thick regime, inverse Compton scattering in the Thomson and Klein-Nishina regime and the production of electron-positron pairs from two photons. It allows for the inclusion of synchrotron-self Compton scattering and inverse Compton scattering on an additional, external radiation field. Validations of limiting cases are consistent with results from previous literature, especially [Blumenthal and Gould \(1970\)](#) and [Mastichiadis and Kirk \(1995\)](#). With dedicated source and escape terms I extended the scope of my implementation to the self-consistent modelling of the radiative processes inside of a plasmoid. Finally, I presented results of a representative plasmoid and a complete chain of plasmoids, which

show good agreement to previous results of [Christie et al. \(2019a\)](#) and ([Schwefer 2019](#)). All in all, this work set the foundation to compare the blazar variability predicted by this model of magnetic reconnection to the gamma-ray fluxes as measured by the FACT telescope during its unbiased long-term monitoring of the brightest blazars.

5.1. Outlook

The results from this work are intended to create a basis for further investigations in blazar variability. To ensure that the FACT MCs cover the complete significant parameter space the efficiencies of the telescope including the analysis have to be taken into account. For the current improvements of the analysis by [Beck \(2019\)](#) no higher leakage values are required. In the case of a future production of new MCs, a real uniform distribution in the zenith distance should be preferred to avoid systematic effects originating from the production. Furthermore, the efficiency of such a new generation could be systematically improved by using an adaptive algorithm as suggested in section 2.4. This could then be used as a lookup table for the calculation of the effective area, which is essential for the calculation of spectra. The calculation of spectra can then be performed as described in [Beck \(2019\)](#). In addition to this, a comparison to the data-driven correction factors for light curves derived in [Theissen \(2020\)](#) offers potential to gain supplementary insights to the underlying physical processes and to check the agreement of MCs and data.

A personal communication is expected to lead to further insights to resolve the discrepancy between the Monte Carlo approach of this thesis and the results by [Petropoulou et al. \(2018\)](#). With these changes, it has to be checked again, how the long-term evolution of the layer will be affected. Together with the study of the stability of the layer from physical arguments it has to be investigated, if such a model could be even stable on longer time scales of multiple years. A larger layer could in principle be expected to lead to longer flares for big plasmoids. This might offer an explanation for the occurrence of long-term active and inactive states like the ones observed for Mrk 501. Apart from the idea that one layer remains for a long time inside of the jet, it is of course not clear, how probable it is that multiple reconnection layers are present in the jet. This idea quickly increases the number of free parameters and might therefore become hard to confirm by measurements.

In addition to this, it is now possible to study in greater detail the effects of pair-production and synchrotron self-Compton, which can be simply turned on and off in the developed implementation. Together with these additional insights, the parameter space of the radiation modelling and the alignment of the layer in the jet can be explored systematically. Then, it can be checked which combinations of parameters are capable to explain the observed behaviour. Also expansions of the model should be taken into account: For example, relativistic magnetic reconnection also works for much smaller pair multiplicities. Because a significant baryonic loading is of particular interest in the context of the production of cosmic rays and high-energy neutrinos, including hadronic interactions might yield completely new features. Moreover, [Christie et al. \(2019b\)](#) found a significant effect of the radiation emitted by neighbouring plasmoids, which then acts

as another incoming radiation field for inverse Compton scattering. This effect is in particular important for the radiation modelling in small plasmoids next to big ones and can be included rather simple into the current implementation. Also the effect of mergers which cause a small dip in the evolution of the size of a plasmoid might create features in the observable emission. In general, the feedback of the radiative losses on the dynamics and the plasmoid's structure are approximated to be negligible and it needs to be further investigated under which circumstances this remains valid.

In order to compare the results of the theoretical model to observational data, different checks need to be performed. Of course the measured spectrum of a complete layer needs to be calculated and compared to measurements at all wavelengths like those used for the blazar sequence. Light curves as illustratively shown in this thesis need to be calculated for other energy ranges as well and compared to observational data from respective instruments. This can be done in two approaches: On the one hand, the typical shape of flares could be studied and compared to observations. On the other hand, the power spectral density (PSD) of a time series offers a sophisticated mean for a comparison at a statistical level. Since FACT is specialised on unbiased long-term modelling, such an analysis is in particular interesting for light curves obtained by this instrument. This is discussed in great detail in [Theissen \(2020\)](#), where also a search for periodic behaviour is performed. In the context of these results a periodicity analysis of the simulated light curves is of special interest. Moreover, light curves of different energy ranges are found to be correlated, which yields another opportunity to compare the theoretical model to observations. Overall, there is thus a large potential to use the investigated model of magnetic reconnection as the driving process of energy dissipation in the jet to gain understanding in the complex phenomenology of blazar variability as measured for example with FACT.

A

List of Abbreviations

ADC analog-to-digital converter

AGN active galactic nucleus

BB black body

BZ mechanism Blandford-Znajek mechanism

BL Lac BL Lacertae

BLR broad line region

CERES Camera Electronics and REflector Simulation

CMB cosmic microwave background

COG center of gravity

CORSIKA COsmic Ray SImulations for KAscade

CTA Cherenkov Telescope Array

DSA diffusive shock acceleration

EAS extensive air shower

EC external Compton

FACT First G-APD Cherenkov Telescope

FSRQ flat-spectrum radio quasar

G-APD Geiger-mode avalanche photodiode

HE high-energy

H.E.S.S High Energy Stereoscopic System

IACT imaging air Cherenkov telescope

ILT instantaneous Lorentz-transformation

MAGIC Major Atmospheric Gamma-Ray Imaging Cherenkov Telescopes

MARS Modular Analysis and Reconstruction Software

MARS-CheObs Modular Analysis and Reconstruction Software - Cherenkov Observatory edition

MC Monte Carlo

MHD magnetohydrodynamics

Mrk 421 Markarian 421

Mrk 501 Markarian 501

NLR narrow line region

PDF probability density function

PIC particle-in-cell

PMT photo multiplier tubes

PSF point-spread-function

QLA quick-look analysis

SED spectral energy distribution

SMBH supermassive black hole

SSA synchrotron-self-absorption

SSC synchrotron self-Compton

UHE ultra-high-energy

VERITAS Very Energetic Radiation Imaging Telescope Array System

VHE very-high-energy

References

- Ackermann, M. et al. (June 2016). "Minute-timescale >100 MeV γ -Ray Variability during the Giant Outburst of Quasar 3C 279 Observed by Fermi-LAT in 2015 June". In: *The Astrophysical Journal, Letters* 824.2, L20, p. L20. DOI: [10.3847/2041-8205/824/2/L20](https://doi.org/10.3847/2041-8205/824/2/L20). arXiv: [1605.05324 \[astro-ph.HE\]](https://arxiv.org/abs/1605.05324).
- Aharonian, F. et al. (Aug. 2007). "An Exceptional Very High Energy Gamma-Ray Flare of PKS 2155-304". In: *The Astrophysical Journal, Letters* 664.2, pp. L71–L74. DOI: [10.1086/520635](https://doi.org/10.1086/520635). arXiv: [0706.0797 \[astro-ph\]](https://arxiv.org/abs/0706.0797).
- Ahnen, M. L. et al. (Sept. 2016). "Long-term multi-wavelength variability and correlation study of Markarian 421 from 2007 to 2009". In: *Astronomy and Astrophysics* 593, A91, A91. DOI: [10.1051/0004-6361/201628447](https://doi.org/10.1051/0004-6361/201628447). arXiv: [1605.09017 \[astro-ph.GA\]](https://arxiv.org/abs/1605.09017).
- Albert, J. et al. (Nov. 2007). "Variable Very High Energy γ -Ray Emission from Markarian 501". In: *The Astrophysical Journal* 669.2, pp. 862–883. DOI: [10.1086/521382](https://doi.org/10.1086/521382). arXiv: [astro-ph/0702008 \[astro-ph\]](https://arxiv.org/abs/astro-ph/0702008).
- Anderhub, H. et al. (June 2013). "Design and operation of FACT - the first G-APD Cherenkov telescope". In: *Journal of Instrumentation* 8.6, P06008, P06008. DOI: [10.1088/1748-0221/8/06/P06008](https://doi.org/10.1088/1748-0221/8/06/P06008). arXiv: [1304.1710](https://arxiv.org/abs/1304.1710).
- Arlen, T. et al. (Jan. 2013). "Rapid TeV Gamma-Ray Flaring of BL Lacertae". In: *The Astrophysical Journal* 762.2, 92, p. 92. DOI: [10.1088/0004-637X/762/2/92](https://doi.org/10.1088/0004-637X/762/2/92). arXiv: [1211.3073 \[astro-ph.HE\]](https://arxiv.org/abs/1211.3073).
- Ayala Solares, H. A. et al. (Jan. 2020). "The Astrophysical Multimessenger Observatory Network (AMON): Performance and science program". In: *Astroparticle Physics* 114, pp. 68–76. DOI: [10.1016/j.astropartphys.2019.06.007](https://doi.org/10.1016/j.astropartphys.2019.06.007). arXiv: [1903.08714 \[astro-ph.IM\]](https://arxiv.org/abs/1903.08714).
- Beck, M. (2019). "Spectral analysis with the First G-APD Cherenkov Telescope under changing observational conditions". Masterthesis. Physikalisches Institut 3A, RWTH Aachen.
- Blandford, R. D. and D. G. Payne (June 1982). "Hydromagnetic flows from accretion disks and the production of radio jets." In: *Monthly Notices of the Royal Astronomical Society* 199, pp. 883–903. DOI: [10.1093/mnras/199.4.883](https://doi.org/10.1093/mnras/199.4.883).

- Blandford, R. D. and R. L. Znajek (May 1977). "Electromagnetic extraction of energy from Kerr black holes." In: *Monthly Notices of the Royal Astronomical Society* 179, pp. 433–456. DOI: [10.1093/mnras/179.3.433](https://doi.org/10.1093/mnras/179.3.433).
- Blandford, R., D. Meier, and A. Readhead (Aug. 2019). "Relativistic Jets from Active Galactic Nuclei". In: *Annual Review of Astronomy and Astrophysics* 57, pp. 467–509. DOI: [10.1146/annurev-astro-081817-051948](https://doi.org/10.1146/annurev-astro-081817-051948). arXiv: [1812.06025 \[astro-ph.HE\]](https://arxiv.org/abs/1812.06025).
- Blumenthal, G. R. and R. J. Gould (Jan. 1970). "Bremsstrahlung, Synchrotron Radiation, and Compton Scattering of High-Energy Electrons Traversing Dilute Gases". In: *Reviews of Modern Physics* 42.2, pp. 237–271. DOI: [10.1103/RevModPhys.42.237](https://doi.org/10.1103/RevModPhys.42.237).
- Böttcher, M. (Jan. 2019). "Progress in Multi-wavelength and Multi-Messenger Observations of Blazars and Theoretical Challenges". In: *Galaxies* 7.1, p. 20. DOI: [10.3390/galaxies7010020](https://doi.org/10.3390/galaxies7010020). arXiv: [1901.04178 \[astro-ph.HE\]](https://arxiv.org/abs/1901.04178).
- Bretz, T. and D. Dorner (Apr. 2010). "MARS - CheObs ed. – A flexible Software Framework for future Cherenkov Telescopes". In: *Astroparticle, Particle and Space Physics, Detectors and Medical Physics Applications*. Ed. by C. Leroy et al., pp. 681–687. DOI: [10.1142/9789814307529_0111](https://doi.org/10.1142/9789814307529_0111).
- Britto, R. J. et al. (Oct. 2016). "Fermi-LAT Observations of the 2014 May-July Outburst from 3C 454.3". In: *The Astrophysical Journal* 830.2, 162, p. 162. DOI: [10.3847/0004-637X/830/2/162](https://doi.org/10.3847/0004-637X/830/2/162). arXiv: [1511.02280 \[astro-ph.HE\]](https://arxiv.org/abs/1511.02280).
- Bühler, R. and R. Blandford (June 2014). "The surprising Crab pulsar and its nebula: a review". In: *Reports on Progress in Physics* 77.6, 066901, p. 066901. DOI: [10.1088/0034-4885/77/6/066901](https://doi.org/10.1088/0034-4885/77/6/066901). arXiv: [1309.7046 \[astro-ph.HE\]](https://arxiv.org/abs/1309.7046).
- Chang, J. S. and G. Cooper (Aug. 1970). "A Practical Difference Scheme for Fokker-Planck Equations". In: *Journal of Computational Physics* 6.1, pp. 1–16. DOI: [10.1016/0021-9991\(70\)90001-X](https://doi.org/10.1016/0021-9991(70)90001-X).
- Christie, I. M. et al. (Jan. 2019a). "Radiative signatures of plasmoid-dominated reconnection in blazar jets". In: *Monthly Notices of the Royal Astronomical Society* 482.1, pp. 65–82. DOI: [10.1093/mnras/sty2636](https://doi.org/10.1093/mnras/sty2636). arXiv: [1807.08041 \[astro-ph.HE\]](https://arxiv.org/abs/1807.08041).
- Christie, I. M. et al. (Aug. 2019b). "Inter-Plasmoid Compton Scattering and the Compton Dominance of BL Lacs". In: *arXiv e-prints*, arXiv:1908.02764, arXiv:1908.02764. arXiv: [1908.02764 \[astro-ph.HE\]](https://arxiv.org/abs/1908.02764).
- Comisso, L. and F. A. Asenjo (July 2014). "Thermal-Inertial Effects on Magnetic Reconnection in Relativistic Pair Plasmas". In: *Physical Review Letters* 113.4, 045001, p. 045001. DOI: [10.1103/PhysRevLett.113.045001](https://doi.org/10.1103/PhysRevLett.113.045001). arXiv: [1402.1115 \[physics.plasm-ph\]](https://arxiv.org/abs/1402.1115).

- Coppi, P. S. and R. D. Blandford (Aug. 1990). "Reaction rates and energy distributions for elementary processes in relativistic pair plasmas". In: *Monthly Notices of the Royal Astronomical Society* 245, pp. 453–507.
- De Angelis, A. and M. J. M. Pimenta (2015). *Introduction to Particle and Astroparticle Physics*. 1st ed. Springer. DOI: [10.1007/978-88-470-2688-9](https://doi.org/10.1007/978-88-470-2688-9).
- Dermer, C. D. and G. Menon (2009). *High Energy Radiation from Black Holes: Gamma Rays, Cosmic Rays, and Neutrinos*. Princeton University Press. ISBN: 978-0-691-13795-7.
- Einstein, A. (Jan. 1905). "Zur Elektrodynamik bewegter Körper". In: *Annalen der Physik* 322.10, pp. 891–921. DOI: [10.1002/andp.19053221004](https://doi.org/10.1002/andp.19053221004).
- FACT Collaboration et al. (June 2018). "Towards Robotic Operation with the First G-APD Cherenkov Telescope". In: *arXiv e-prints*, arXiv:1806.01542, arXiv:1806.01542. arXiv: [1806.01542 \[astro-ph.IM\]](https://arxiv.org/abs/1806.01542).
- Fitzpatrick, R. (2014). *Plasma Physics: An Introduction*. 1st ed. CRC Press.
- Foschini, L. (Nov. 2011). "Accretion and jet power in active galactic nuclei". In: *Research in Astronomy and Astrophysics* 11.11, pp. 1266–1278. DOI: [10.1088/1674-4527/11/11/003](https://doi.org/10.1088/1674-4527/11/11/003). arXiv: [1106.5532 \[astro-ph.HE\]](https://arxiv.org/abs/1106.5532).
- Fossati, G. et al. (Sept. 1998). "A unifying view of the spectral energy distributions of blazars". In: *Monthly Notices of the Royal Astronomical Society* 299.2, pp. 433–448. DOI: [10.1046/j.1365-8711.1998.01828.x](https://doi.org/10.1046/j.1365-8711.1998.01828.x). arXiv: [astro-ph/9804103 \[astro-ph\]](https://arxiv.org/abs/astro-ph/9804103).
- Ghisellini, G. et al. (July 2017). "The Fermi blazar sequence". In: *Monthly Notices of the Royal Astronomical Society* 469.1, pp. 255–266. DOI: [10.1093/mnras/stx806](https://doi.org/10.1093/mnras/stx806). arXiv: [1702.02571 \[astro-ph.HE\]](https://arxiv.org/abs/1702.02571).
- Ghisellini, G. (Sept. 2016). "The Blazar Sequence 2.0". In: *Galaxies* 4.4, p. 36. DOI: [10.3390/galaxies4040036](https://doi.org/10.3390/galaxies4040036). arXiv: [1609.08606 \[astro-ph.HE\]](https://arxiv.org/abs/1609.08606).
- Giannios, D. (May 2013). "Reconnection-driven plasmoids in blazars: fast flares on a slow envelope". In: *Monthly Notices of the Royal Astronomical Society* 431.1, pp. 355–363. DOI: [10.1093/mnras/stt167](https://doi.org/10.1093/mnras/stt167). arXiv: [1211.0296 \[astro-ph.HE\]](https://arxiv.org/abs/1211.0296).
- Ginzburg, V. L. and S. I. Syrovatskii (Jan. 1965). "Cosmic Magnetobremssstrahlung (synchrotron Radiation)". In: *Annual Review of Astronomy and Astrophysics* 3, p. 297. DOI: [10.1146/annurev.aa.03.090165.001501](https://doi.org/10.1146/annurev.aa.03.090165.001501).
- González, M. et al. (Apr. 2019). "Unbiased Long-Term Monitoring at TeV Energies". In: *Galaxies* 7.2, p. 51. DOI: [10.3390/galaxies7020051](https://doi.org/10.3390/galaxies7020051).

- Hildebrand, D. et al. (Jan. 2017). "Using Charged Cosmic Ray Particles to Monitor the Data Quality of FACT". In: *35th International Cosmic Ray Conference (ICRC2017)*. Vol. 301. International Cosmic Ray Conference, p. 779.
- Hillas, A. M. (Aug. 1985). "Cerenkov Light Images of EAS Produced by Primary Gamma Rays and by Nuclei". In: *19th International Cosmic Ray Conference (ICRC19), Volume 3*. Vol. 3. International Cosmic Ray Conference, p. 445.
- Hoyle, F. (Jan. 1960). "Radio-source problems". In: *Monthly Notices of the Royal Astronomical Society* 120, p. 338. DOI: [10.1093/mnras/120.4.338](https://doi.org/10.1093/mnras/120.4.338).
- Jackson, J. D. (1998). *Classical Electrodynamics*. 3rd ed. John Wiley & Sons.
- Jones, F. C. (Mar. 1968). "Calculated Spectrum of Inverse-Compton-Scattered Photons". In: *Phys. Rev.* 167 (5), pp. 1159–1169. DOI: [10.1103/PhysRev.167.1159](https://doi.org/10.1103/PhysRev.167.1159). URL: <https://link.aps.org/doi/10.1103/PhysRev.167.1159>.
- Kagan, D. et al. (Oct. 2015). "Relativistic Magnetic Reconnection in Pair Plasmas and Its Astrophysical Applications". In: *Space Science Reviews* 191.1-4, pp. 545–573. DOI: [10.1007/s11214-014-0132-9](https://doi.org/10.1007/s11214-014-0132-9). arXiv: [1412.2451 \[astro-ph.HE\]](https://arxiv.org/abs/1412.2451).
- Kardashev, N. S. (Jan. 1962). "Nonstationarity of Spectra of Young Sources of Nonthermal Radio Emission". In: *Astronomicheskii Zhurnal* 39, p. 393.
- Kormendy, J. and L. C. Ho (Aug. 2013). "Coevolution (Or Not) of Supermassive Black Holes and Host Galaxies". In: *Annual Review of Astronomy and Astrophysics* 51.1, pp. 511–653. DOI: [10.1146/annurev-astro-082708-101811](https://doi.org/10.1146/annurev-astro-082708-101811). arXiv: [1304.7762 \[astro-ph.CO\]](https://arxiv.org/abs/1304.7762).
- Kulsrud, R. M. (2005). *Plasma Physics for Astrophysics*. Princeton University Press.
- Lessard, R. W. et al. (Mar. 2001). "A new analysis method for reconstructing the arrival direction of TeV gamma rays using a single imaging atmospheric Cherenkov telescope". In: *Astroparticle Physics* 15.1, pp. 1–18. DOI: [10.1016/S0927-6505\(00\)00133-X](https://doi.org/10.1016/S0927-6505(00)00133-X). arXiv: [astro-ph/0005468 \[astro-ph\]](https://arxiv.org/abs/astro-ph/0005468).
- Longair, M. S. (2011). *High Energy Astrophysics*. 3rd ed. Cambridge University Press. ISBN: 978-0-521-75618-1. DOI: [10.1017/CBO9780511778346](https://doi.org/10.1017/CBO9780511778346).
- Loureiro, N. F., A. A. Schekochihin, and S. C. Cowley (Oct. 2007). "Instability of current sheets and formation of plasmoid chains". In: *Physics of Plasmas* 14.10, pp. 100703–100703. DOI: [10.1063/1.2783986](https://doi.org/10.1063/1.2783986). arXiv: [astro-ph/0703631 \[astro-ph\]](https://arxiv.org/abs/astro-ph/0703631).
- Lyubarsky, Y. E. (Mar. 2005). "On the relativistic magnetic reconnection". In: *Monthly Notices of the Royal Astronomical Society* 358.1, pp. 113–119. DOI: [10.1111/j.1365-2966.2005.08767.x](https://doi.org/10.1111/j.1365-2966.2005.08767.x). arXiv: [astro-ph/0501392 \[astro-ph\]](https://arxiv.org/abs/astro-ph/0501392).

- Mastichiadis, A. and J. G. Kirk (Mar. 1995). "Self-consistent particle acceleration in active galactic nuclei." In: *Astronomy and Astrophysics* 295, p. 613.
- Nigro, C. et al. (May 2019). "Towards open and reproducible multi-instrument analysis in gamma-ray astronomy". In: *Astronomy and Astrophysics* 625, A10, A10. DOI: [10.1051/0004-6361/201834938](https://doi.org/10.1051/0004-6361/201834938). arXiv: [1903.06621 \[astro-ph.HE\]](https://arxiv.org/abs/1903.06621).
- Padovani, P. (Nov. 2017). "Active Galactic Nuclei at all wavelengths and from all angles". In: *Frontiers in Astronomy and Space Sciences* 4, 35, p. 35. DOI: [10.3389/fspas.2017.00035](https://doi.org/10.3389/fspas.2017.00035).
- Parker, E. N. (Dec. 1957). "Sweet's Mechanism for Merging Magnetic Fields in Conducting Fluids". In: *Journal of Geophysical Research* 62.4, pp. 509–520. DOI: [10.1029/JZ062i004p00509](https://doi.org/10.1029/JZ062i004p00509).
- Paterno, M. (Dec. 2004). "Calculating efficiencies and their uncertainties". In: DOI: [10.2172/15017262](https://doi.org/10.2172/15017262).
- Petropoulou, M. et al. (Apr. 2018). "Plasmoid statistics in relativistic magnetic reconnection". In: *Monthly Notices of the Royal Astronomical Society* 475.3, pp. 3797–3812. DOI: [10.1093/mnras/sty033](https://doi.org/10.1093/mnras/sty033). arXiv: [1710.00724 \[astro-ph.HE\]](https://arxiv.org/abs/1710.00724).
- Petschek, H. E. (1964). "Magnetic Field Annihilation". In: *The Physics of Solar Flares, Proceedings of the AAS-NASA Symposium held 28-30 October, 1963 at the Goddard Space Flight Center, Greenbelt, MD. Edited by Wilmot N. Hess. Washington, DC: National Aeronautics and Space Administration, Science and Technical Information Division, 1964., p.425.* Vol. 50, p. 425.
- Punch, M. et al. (Aug. 1992). "Detection of TeV photons from the active galaxy Markarian 421". In: *Nature* 358.6386, pp. 477–478. DOI: [10.1038/358477a0](https://doi.org/10.1038/358477a0).
- Rybicki, G. B. and A. P. Lightman (1986). *Radiative Processes in Astrophysics*. John Wiley & Sons, Ltd. ISBN: 9783527618170. DOI: [10.1002/9783527618170](https://doi.org/10.1002/9783527618170).
- Schmidt, F. and J. Knapp (2005). *CORSIKA Shower Images*. URL: <https://www-zeuthen.desy.de/~jknapp/fs/showerimages.html> (visited on 11/15/2019).
- Schwefer, G. (2019). "Blazar Flares from Plasmoids". Bachelorthesis. Institute for Theoretical Particle Physics and Cosmology, RWTH Aachen.
- Sironi, L., D. Giannios, and M. Petropoulou (Oct. 2016). "Plasmoids in relativistic reconnection, from birth to adulthood: first they grow, then they go". In: *Monthly Notices of the Royal Astronomical Society* 462.1, pp. 48–74. DOI: [10.1093/mnras/stw1620](https://doi.org/10.1093/mnras/stw1620). arXiv: [1605.02071 \[astro-ph.HE\]](https://arxiv.org/abs/1605.02071).

- Sironi, L. and A. Spitkovsky (Oct. 2014). "Relativistic Reconnection: An Efficient Source of Non-thermal Particles". In: *The Astrophysical Journal* 783.1, L21, p. L21. DOI: [10 . 1088/2041-8205/783/1/L21](https://doi.org/10.1088/2041-8205/783/1/L21). arXiv: [1401 . 5471 \[astro-ph.HE\]](https://arxiv.org/abs/1401.5471).
- Sliusar, V. et al. (Sept. 2019). "5.5 years multi-wavelength variability of Mrk 421: evidences of leptonic emission from the radio to TeV". In: *arXiv e-prints*, arXiv:1909.13106, arXiv:1909.13106. arXiv: [1909 . 13106 \[astro-ph.HE\]](https://arxiv.org/abs/1909.13106).
- Smith, A. J. (Jan. 2005). "The MILAGRO Gamma Ray Observatory". In: *29th International Cosmic Ray Conference (ICRC29), Volume 10*. Vol. 10. International Cosmic Ray Conference, p. 227.
- Sparke, L. S. and I. Gallagher John S. (2007). *Galaxies in the Universe: An Introduction*. 2nd ed. Cambridge University Press. ISBN: 978-0-511-29472-3.
- Spurio, M. (2015). *Particles and Astrophysics - A Multi-Messenger Approach*. 1st ed. Springer. ISBN: 978-3-319-08051-2. DOI: [10 . 1007 / 978-3-319-08051-2](https://doi.org/10.1007/978-3-319-08051-2).
- Sweet, P. A. (Jan. 1958). "The Neutral Point Theory of Solar Flares". In: *Electromagnetic Phenomena in Cosmical Physics*. Ed. by B. Lehnert. Vol. 6. IAU Symposium, p. 123.
- Temme, F. et al. (Feb. 2017). "Long-Term Monitoring of Bright Blazars in the Multi-GeV to TeV Range with FACT". In: *Galaxies* 5.1, p. 18. DOI: [10 . 3390 / galaxies5010018](https://doi.org/10.3390/galaxies5010018).
- Theissen, F. (2020). "Data-Driven Efficiency Corrections Enabling Unbiased Periodicity Analyses with the FACT Telescope". Masterthesis. Physikalisches Institut 3A, RWTH Aachen.
- Urry, C. M. and P. Padovani (Sept. 1995). "Unified Schemes for Radio-Loud Active Galactic Nuclei". In: *Publications of the ASP* 107, p. 803. DOI: [10 . 1086 / 133630](https://doi.org/10.1086/133630). arXiv: [astro-ph/9506063 \[astro-ph\]](https://arxiv.org/abs/astro-ph/9506063).
- Uzdensky, D. A., N. F. Loureiro, and A. A. Schekochihin (Dec. 2010). "Fast Magnetic Reconnection in the Plasmoid-Dominated Regime". In: *Physical Review Letters* 105.23, 235002, p. 235002. DOI: [10 . 1103 / PhysRevLett . 105 . 235002](https://doi.org/10.1103/PhysRevLett.105.235002). arXiv: [1008 . 3330 \[astro-ph.SR\]](https://arxiv.org/abs/1008.3330).
- Völk, H. J. and K. Bernlöhr (Aug. 2009). "Imaging very high energy gamma-ray telescopes". In: *Experimental Astronomy* 25.1-3, pp. 173–191. DOI: [10 . 1007 / s10686-009-9151-z](https://doi.org/10.1007/s10686-009-9151-z). arXiv: [0812 . 4198 \[astro-ph\]](https://arxiv.org/abs/0812.4198).
- Weekes, T. C. et al. (July 1989). "Observation of TeV Gamma Rays from the Crab Nebula Using the Atmospheric Cerenkov Imaging Technique". In: *The Astrophysical Journal* 342, p. 379. DOI: [10 . 1086 / 167599](https://doi.org/10.1086/167599).

Werner, G. et al. (Oct. 2017). "Nonthermal particle acceleration in 3D relativistic pair reconnection". In: *APS Division of Plasma Physics Meeting Abstracts*. Vol. 2017, BO6.010.